

**TOUGHENING OF CARBON FIBER BASED
COMPOSITES WITH ELECTROSPUN FABRIC
LAYERS**

**A Thesis Submitted to
the Graduate School of Engineering and Science of
Izmir Institute of Technology
in Partial Fulfillment of the Requirements for the Degree of**

DOCTOR OF PHILOSOPHY

in Mechanical Engineering

**by
Bertan BEYLERGİL**

**November 2017
İZMİR**

We approve the thesis of **Bertan BEYLERGİL**

Examining Committee Members:

Prof. Dr. Metin TANOĞLU

Department of Mechanical Engineering, İzmir Institute of Technology

Prof. Dr. Sacide Alsoy ALTINKAYA

Department of Chemical Engineering, İzmir Institute of Technology

Assoc. Prof. Dr. H. Seçil ARTEM

Department of Mechanical Engineering, İzmir Institute of Technology

Assist. Prof. Dr. Levent AYDIN

Department of Mechanical Engineering, İzmir Katip Çelebi University

Assist. Prof. Dr. Aylin ZİYLAN

Department of Metallurgical and Materials Engineering, Dokuz Eylül University

14 November 2017

Prof. Dr. Metin TANOĞLU

Advisor, Department of Mechanical Engineering, İzmir Institute of Technology

Assoc. Prof. Dr. Engin AKTAŞ

Co-advisor, Department of Civil Engineering, İzmir Institute of Technology

Prof. Dr. Metin TANOĞLU

Head of the Department of Mechanical Engineering

Prof. Dr. Aysun SOFUOĞLU

Dean of the Graduate School of Engineering and Sciences

Dedicated to my father and grandmother in heaven;

ACKNOWLEDGMENTS

I would like to give my sincere thanks to my advisor Professor Dr. Metin TANOĞLU and my co-advisor Assoc. Professor Engin AKTAŞ for their useful comments, guidance, support, encouragement and motivation. Besides my advisors, I would like to thank the rest of my PhD thesis committee members Professor Sacide ALSOY ALTINKAYA and Assoc. Professor Hatice Seçil ARTEM for their encouragement, constructive comments and challenging questions.

I would like to thank to my labmates and friends Mehmet Deniz GÜNEŞ, Oylum Çolpankan GÜNEŞ, Osman KARTAV, Mehmet Ziya OKUR, Serkan KANGAL and Zeynep AY for their help and unconditional support.

I would like to thank Albert ORTEGA (Director of Technology, Cerex Advanced Fabrics Inc. USA) for supplying PA 66 nonwoven materials. I would like to thank KORDSA Global Inc. of Turkey for providing unidirectional carbon fabrics and PA66 pellets.

Lastly, I offer my sincere thanks to my mother Gülümser BEYLERGİL, my brother Dr. Volkan BEYLERGİL and my wife Sevil BEYLERGİL for their love, motivation and support during my study.

ABSTRACT

TOUGHENING OF CARBON FIBER BASED COMPOSITES WITH ELECTROSPUN FABRIC LAYERS

The objective of this PhD thesis is to investigate interlaminar Mode-I fracture toughness of carbon fiber/epoxy composites interleaved by micro and/or nano scaled PA66 nonwoven veils. Also, the effects of electrospun PVA nanofibers on the mechanical performance of these composites were investigated. Additionally, this thesis also deals with the effects of aramid nonwoven veils on the mechanical properties of CF/EP composites. The produced nanofibers produced by electrospinning were directly deposited on carbon fiber fabrics. Then, reference and nano-modified laminates were manufactured by vacuum infusion method. A series of mechanical tests such as tensile, compression, three point bending, Charpy-impact, interlaminar shear strength and open hole tensile tests (OHT) were carried out on the prepared specimens. Double cantilever beam (DCB) tests were conducted on reference and interleaf-modified laminates. The effect of PA 66 nanofiber areal weight density was also evaluated with varying electrospinning time. Scanning electron microscopy (SEM) was used to investigate the fiber morphology and to understand the toughening mechanisms. Dynamic mechanic analysis (DMA) was used to investigate the thermo-mechanical behavior of reference and interleaf-modified composite specimens. Differential scanning calorimetry (DSC) was used to determine the thermal properties of micro and electrospun PA66 nonwoven veils. Comparing the mechanical test results, the most effective nonwoven interleaving system was determined in terms of higher delamination resistance and in-plane mechanical properties. Finite element method (FEM) was used to evaluate the effects of electrospun PA66 nonwoven veils on the CF/EP composites. Numerical simulations of Mode-I fracture toughness tests were carried out using ANSYS Workbench. The results showed that the most effective material was electrospun PA66 nonwovens considering the higher delamination resistance. Additionally, the electrospun PA 66 nonwovens also improved Charpy-impact and interlaminar shear strength of the reference CF/EP composites. Numerical results showed good agreement with the experimental ones.

ÖZET

ELEKTROEĞRİLMİŞ KUMAŞ TABAKALARI İLE KARBON ELYAF ESASLI KOMPOZİTLERİN TOKLAŞTIRILMASI

Bu doktora tezinin amacı, arayüzeyde mikro ve/veya nano boyutta poliamid 66 (PA 66) dokusuz kumaş tabakaları kullanılarak üretilmiş karbon fiber/epoksi (KF/EP) kompozitlerin Mod-I kırılma tokluğunun incelenmesidir. Ayrıca, elektroğrılmış polivinil alkol (PVA) nanofiberlerin bu kompozitlerin mekanik performansı üzerine etkileri incelenmiştir. Buna ek olarak, bu tezde aramid dokusuz kumaşlar kullanılarak üretilmiş KF/EP kompozitlerin mekanik özellikleri incelenmiştir. Üretilen nanofiberler direkt olarak karbon kumaş üzerine kaplanmıştır. Daha sonra referans ve nanofiber takviyeli kompozitler vakum infüzyon yöntemiyle üretilmiştir. Üretilen numunelere çekme, basma, üç-nokta eğme, Charpy-darbe, arayüzey kayma mukavemeti ve delikli çekme testleri yapılmıştır. Referans ve arayüzeyi modifiye edilmiş numunelere Çift Ankastre Kiriş Testleri (DCB) yapılmıştır. PA 66 nanofiber alansal yoğunluğunun etkisi elektroğirme süresi değiştirilerek ortaya konmuştur. Taramalı elektron mikroskobu kullanılarak fiber morfolojisi ve arayüzey kırılma mekanizmaları incelenmiştir. Dinamik mekaniz analiz (DMA) ile referans ve arayüzeyi modifiye edilmiş kompozit numunelerin termomekanik özellikleri incelenmiştir. Diferansiyel taramalı kalorimetre (DSC) yöntemiyle mikro ve elektroğrılmış PA66 dokusuz kumaşların termal özellikleri belirlenmiştir. Mekanik test sonuçları karşılaştırılarak, delaminasyon direnci ve düzlem-içi mukavemet açısından en verimli dokusuz kumaş sistemi belirlenmiştir. Buna ek olarak sonlu elemanlar yöntemi ile elektroğrılmış PA 66 nanokumaş tabakaların KF/EP kompozitler üzerine etkisi incelenmiştir. Mod- I kırılma tokluğu testlerinin nümerik simülasyonları ANSYS Workbench kullanılarak gerçekleştirilmiştir. Sonuçlar en verimli sistemin elektroğrılmış PA66 dokusuz kumaşlar olduğunu göstermiştir. Buna ek olarak, bu kumaşların referans KF/EP kompozitlerin darbe direncini ve arayüzey mukavemetini iyileştirdiği gözlemlenmiştir. Nümerik sonuçların deneysel sonuçlarla uyum gösterdiği belirlenmiştir.

TABLE OF CONTENTS

CHAPTER 1. INTRODUCTION	19
1.1. Background	19
1.2. Objectives	21
1.3. Thesis outline	22
1.4. Unique contributions	24
CHAPTER 2. FUNDAMENTAL CONCEPTS AND RELEVANT LITERATURE	26
2.1. Introduction to Composite Materials.....	26
2.1.1. Definition of a composite material	28
2.1.2. Components of composite materials.....	29
2.1.3. Classification of composite materials.....	30
2.1.4. Manufacturing techniques for FRP composites.....	36
2.2. Failure and damage mechanisms in unidirectional composites	39
2.3. Delamination	40
2.3.1. Suppression of delamination and toughening mechanism in composite materials.....	41
2.3.1.1. Mechanical approach	43
2.3.1.2. Material approach	47
2.3.1.3. Interleaving technique.....	48
2.4. Toughening of polymeric composite materials with nanofibrous mats	50
2.4.1. Electrospinning.....	51
2.4.2. Literature review on electrospun nanofiber toughened composites	53

CHAPTER 3. EXPERIMENTAL.....	67
3.1. Materials.....	67
3.2. Electrospinning and deposition of electrospun nanofibers onto carbon fabrics.....	70
3.3. Manufacturing of composite laminates.....	74
3.4. Mechanical characterization of composite specimens.....	76
3.5. Fractured surface observations and dynamic mechanical analysis (DMA)	81
3.6. Calculation of carbon fiber volume fraction (V_f).....	82
CHAPTER 4. RESULTS AND DISCUSSION.....	83
4.1. Effects of interleaf materials on carbon fiber volume fraction (V_f) of CF/EP composites.....	83
4.2. Effects of interleaf materials on the tensile properties of CF/EP composites.	84
4.3. Effects of interleaf materials on the flexural and interlaminar shear properties of CF/EP composites.....	92
4.4. Effects of interleaf materials on the compressive properties of CF/EP composites.....	100
4.5. Effects of interleaf materials on the impact strength of CF/EP composites..	103
4.6. Effects of interleaf materials on the Mode-I fracture toughness of CF/EP composites.....	107
4.7. Effects of interleaf materials on thermomechanical behavior of CF/EP composites.....	123
4.8. Comparison of interleaf materials on the mechanical performance of CF/EP composites.....	126

CHAPTER 5. FINITE ELEMENT MODELING OF CF/EP COMPOSITES INTERLEAVED BY ELECTROSPUN PA 66 NANOFIBERS.....	132
5.1. Delamination analysis using ANSYS	132
5.2. Cohesive zone modeling	132
5.3. FEM model.....	135
5.4. Comparison of experimental and numerical results	137
CHAPTER 6. CONCLUDING REMARKS and FUTURE WORK.....	141
6.1. Conclusions	141
6.2. Future work	144
6.3. List of publications.....	146
REFERENCES	148

LIST OF FIGURES

Figure 2.1.1. The process of ancient Egyptian brick making	27
Figure 2.1.2 Some of structural applications of CFRPs	28
Figure 2.1.3. SEM image of a hybrid composite structure made of boron fiber/epoxy and aluminum layer	29
Figure 2.1.4. Material structure of a 3D woven composite	29
Figure 2.1.5. Classification of composite materials.....	30
Figure 2.1.6. Continuous and discontinuous reinforcements.....	31
Figure 2.1.7.Examples of composite laminates oriented at different orientations	32
Figure 2.1.8. (a) SEM image of SiC whiskers and (b) whisker pull-out and (c) whisker bridging phenomena observed in ceramic matrix composites	33
Figure 2.1.9. Comparison of thermoset and thermoplastic matrices	34
Figure 2.1.10. CFRP composites market forecasts to 2020.....	35
Figure 2.1.11. Classification of composite manufacturing techniques.....	36
Figure 2.1.12. Recent applications of VaRTM method for aerospace component production	37
Figure 2.1.13.(a) Schematic representation of VaRTM set-up and (b) experimental VaRTM set-up.....	38
Figure 2.2.1. Damage mechanisms observed in composite materials	39
Figure 2.3.1. Damage mechanisms observed in composite materials	41
Figure 2.3.2. Three modes of delamination fracture.....	41

Figure 2.3.3. A stitched composite specimen under Mode-I loading	43
Figure 2.3.4. Microstructural defects caused by stitching process	44
Figure 2.3.5. (a) Manufacturing steps of z-anchoring	45
Figure 2.3.6.(a) Effect of z-pin volume content on the Mode-I fracture toughness	45
Figure 2.3.7. Microstructural defects caused by z-anchoring operation.....	46
Figure 2.3.8. Manufacturing steps of a nanoparticle reinforced composite.	47
Figure 2.3.9. Fiber bridging under Mode-I loading	49
Figure 2.4.1. Laminated composite with nanofiber-reinforced interfacial layer.	51
Figure 2.4.2. Schematic representation of an electrospinning device.	52
Figure 2.4.3. Fabrication steps of PSF nanofibers toughened CF/EP composite	53
Figure 2.4.4. (a) PSF nanofibers and (b) PSF films toughened composite specimens	54
Figure 2.4.5. Mode I delamination fracture toughness and flexure properties as a function of (a) nanofiber diameter and (b) interlayer thickness.....	55
Figure 2.4.6. SEM images of fractured DCB test specimens (a) control specimen, (b) nanofiber diameter: 450 nm, (c-d) nanofiber diameter: 750 nm, (e-f) nanofiber diameter: 950 nm.....	56
Figure 2.4.7. SEM images of electrospun nanofibers; PCL nanofibers; (a) 12 wt.%, (b)15 wt.% and (c) 20 wt.% solutions (d) PVDF nanofibers and (e) PAN nanofibers.....	56
Figure 2.4.8. Mode I fracture toughness (a) PCL and (b) PVDF, PAN interlayers	57

Figure 2.4.9. Fractured surfaces of carbon carbon/epoxy composites after DCB test (a) is the control specimen, (b-f) PCL modified and (e-f) PVDF and PAN modified specimens	58
Figure 2.4.10. Photograph of open hole test specimen after failure	59
Figure 2.4.11. Photograph of local application of nanofibers around the hole... 59	
Figure 2.4.12. Double Cantilever Beam (DCB) fracture tests curves: left) Force vs. COD; right) Mechanical energy vs. COD	61
Figure 2.4.13. End Notched Flexure (ENF) fracture tests curves: left) Stress vs. Strain; right) Mechanical energy vs. Strain.....	61
Figure 2.4.14. SEM micrographs of DCB and ENF fractured surfaces (A-B) DCB and (C-D) ENF tests, Virgin (A-C) and Nanomodified (B-D) interfaces	62
Figure 2.4.15. Double Cantilever Beam (DCB) fracture tests curves	63
Figure 2.4.16. End Notched Flexure (ENF) fracture tests curves.....	64
Figure 2.4.17. (a) Randomly oriented and (b) aligned PA 6.9 nanofibres.....	65
Figure 2.4.18. Nanofiber bridging and necked nanofibers at interlaminar crossings	66
Figure 3.1.1. SEM images of aramid nonwoven veils.....	68
Figure 3.1.2. SEM images of PA66 nonwoven veils.....	68
Figure 3.1.3. DSC curve of the PA66 veils.	69
Figure 3.2.1. Electrospinning set-up in our laboratory	71
Figure 3.2.2. Deposition of electrospun nanofibers on carbon fabrics and (b) a unidirectional carbon fabric after electrospinning.....	71
Figure 3.2.3. Heat treatment of nano modified unidirectional carbon fabrics after the electrospinning process	72

Figure 3.2.4.(a-b) SEM images of PVA nanofibers deposited on a carbon fabric and (c) PVA nanofibers after heat treatment.	73
Figure 3.2.5 SEM images of electrospun PA66 nanofibers.....	73
Figure 3.2.6. DSC curve of the PA66 nonwoven veils.....	74
Figure 3.3.1. Schematic representation of the (a) reference and (b) interleaved composite laminates	74
Figure 3.3.2. Schematic representation of the (a) reference and (b) interleaved composite laminates	75
Figure 3.4.1. Geometry of a dumbbell-like shape tensile test specimens.....	76
Figure 3.4.2. A dumbbell-like shaped tensile test specimen under tension.....	77
Figure 3.4.3. A composite test specimen under flexural loading	78
Figure 3.4.4. Anti-buckling fixture used for compression tests.....	78
Figure 3.4.5. Schematic representation of the DCB test specimens.	79
Figure 3.4.6. A composite test specimen under Mode-I loading	81
Figure 4.2.1. Stress-strain curves of reference composite specimens	84
Figure 4.2.2. Stress-strain curves of the m-AR composite specimens	85
Figure 4.2.3. Stress-strain curves of m-PA66-17 composite specimens	85
Figure 4.2.4. Stress-strain curves of m-PA66-50 composite specimens	86
Figure 4.2.5. Failed m-PA66-50 composite tensile test specimens	86
Figure 4.2.6. Stress-strain curves of nPVA composite specimens	87
Figure 4.2.7. SEM images of the (a-b) reference, (c-d) nPVA composite test specimens after tensile loading.....	88
Figure 4.2.8. Stress-strain curves of nPA66-AWD-0.525 composite specimens.	89

Figure 4.2.9. Stress-strain curves of nPA66-AWD-1.05 composite specimens .	89
Figure 4.2.10. Bead formations observed in n-PA66 composite specimens	90
Figure 4.2.11. SEM images of n-PA66 composite specimens.....	90
Figure 4.2.12. Elastic modulus of composite test specimens	91
Figure 4.2.13. Tensile strength of composite test specimens	92
Figure 4.3.1. Stress-strain curves of reference composite specimens under flexural loading.....	93
Figure 4.3.2. Stress-strain curves of m-AR composite specimens under flexural loading	94
Figure 4.3.3. Stress-strain curves of m-PA66-17 composite specimens under flexural loading.....	94
Figure 4.3.4. Stress-strain curves of m-PA66-50 composite specimens under flexural loading.....	95
Figure 4.3.5. Stress-strain curves of nPVA composite specimens under flexural loading	96
Figure 4.3.6. Stress-strain curves of nPA66-AWD-0.525 composite specimens under flexural loading	97
Figure 4.3.7. Stress-strain curves of nPA66-AWD-1.05 composite specimens under flexural loading	97
Figure 4.3.8. PVA nanofibers within the epoxy matrix.....	98
Figure 4.3.9. ILSS values of composite test specimens.....	99
Figure 4.4.1. Compressive modulus of composite test specimens	102
Figure 4.4.2. Compressive strength of composite test specimens	102
Figure 4.5.1. Fractured surface SEM images of reference Charpy-impact specimens	103

Figure 4.5.2. Fractured surface SEM images of m-AR Charpy-impact specimens	103
Figure 4.5.3. Fractured surface SEM images of m-PA66 Charpy-impact specimens.	105
Figure 4.5.4. Fractured surface SEM images of (a-b) nPVA and (c-d) n-PA66 Charpy-impact specimens.	105
Figure 4.5.5. n-PA66 composite test specimens before and after impact loading.	106
Figure 4.5.6. Charpy impact energy of composite test specimens	106
Figure 4.6.1. Load-displacement curves of reference composite specimens under Mode-I loading.	107
Figure 4.6.2. G_{IC} vs. delamination length of reference composite specimens. .	108
Figure 4.6.3. SEM fracture surface images of the reference specimens.....	108
Figure 4.6.4. Load-displacement curves of m-AR composite specimens under Mode-I loading.	110
Figure 4.6.5. G_{IC} vs. delamination length of m-AR composite specimens.	111
Figure 4.6.6. SEM images of fractured m-AR composite specimens under Mode-I loading.....	111
Figure 4.6.7. Load-displacement curves of m-PA66-17 composite specimens under Mode-I loading.	112
Figure 4.6.8. Load-displacement curves of m-PA66-50 composite specimens under Mode-I loading.	113
Figure 4.6.9. Schematic representation of the crack propagation in m-PA66 composite specimens	113
Figure 4.6.10. G_{IC} vs. delamination length of m-PA66 composite specimens. .	115

Figure 4.6.11. (a-b) Photographs of m-PA66 composite specimens under Mode-I loading and (c-d) SEM images of fractured surfaces of m-PA66 composite specimens.....	115
Figure 4.6.12. Photograph of the DCB surfaces of fractured m-PA66 composite.....	116
Figure 4.6.13. Load-displacement curves of nPVA composite specimens under Mode-I loading.....	117
Figure 4.6.14. G_{IC} vs. delamination length of nPVA composite specimens.....	117
Figure 4.6.15. SEM images of fractured surfaces of nPVA composite specimens.	118
Figure 4.6.16. Load-displacement curves of nPA66-AWD-0.525 composite specimens under Mode-I loading.	119
Figure 4.6.17. G_{IC} vs. delamination length of nPA66-AWD-0.525 composite specimens.	119
Figure 4.6.18. Load-displacement curves of nPA66-AWD-1.05 composite specimens under Mode-I loading.	120
Figure 4.6.19. G_{IC} vs. delamination length of nPA66-AWD-1.05 composite specimens.	120
Figure 4.6.20. SEM images of Mode-I fractured surfaces of nPA66 interleaved composite specimens.....	121
Figure 4.6.21. Initiation Mode-I fracture toughness (G_{IC}) of composite test specimens	122
Figure 4.6.22. Propagation Mode-I fracture toughness (G_{IC}) of composite test specimens	123
Figure 4.7.1. Storage and loss modulus of composite test specimens	124
Figure 4.7.2. $\tan\delta$ (peak) values of composite test specimens.....	126

Figure 5.2.1. Bonding and debonding in the process zone [112].	133
Figure 5.3.1. (a) Mesh structure and (b) boundary and loading conditions.....	135
Figure 5.3.2. von-Mises stress distribution in DCB composite specimen.....	136
Figure 5.4.1. Comparison between experimental and cohesive zone model in the case of reference specimens	137
Figure 5.4.2. Comparison between experimental and cohesive zone model in the case of n-PA66-AWD-0.525 specimens (a) initial and (b) propagation stage.....	138
Figure 5.4.3. Comparison between experimental and cohesive zone model in the case of n-PA66-AWD-1.05 specimens (a) initial and (b) propagation stage.....	139

LIST OF TABLES

Table 2.1. The roles of the fiber and the matrix in mechanical properties	32
Table 2.2. Comparison of different fibers used in composites [32]	35
Table 3.1. Physical and mechanical properties of the aramid veils	67
Table 3.2. Designation codes for composite test specimens.....	75
Table 4.1. Carbon fiber volume fraction (V_f) of composite specimens.....	83
Table 4.2. Glass transition temperature (T_g) of composite specimens	124
Table 4.3. Comparison of the effectiveness of various microfiber interleaving systems.....	128
Table 4.4. Comparison of the effectiveness of various nanofiber interleaving systems.....	131
Table 5.1. Material properties of composites used for verification	135
Table 5.2. Comparison of experimental and numerical results	136
Table 5.3. Cohesive zone parameters used for numerical modeling of nanomodified composite specimens	140
Table 5.4. Comparison of numerical and experimental Mode-I fracture toughness values for reference and PA66 nanomodified specimens	140

CHAPTER 1

INTRODUCTION

1.1. Background

Fiber-reinforced polymer matrix composites are extensively used in many engineering applications. They were once considered for high-performance applications such as aerospace, aviation and defense. Yet, they have become critical materials for all divisions of engineering over the last few decades. The application of these materials has shown a tremendous growth in many fields ranging from trivial, industrial products such as boxes and covers produced in enormous numbers each day, to pipelines and crucial, load bearing parts of large structures. Some important reasons for this popularity are: their high strength (and stiffness) to weight ratio; the possibility of controlling the anisotropy; and the fact that the fiber composites are resistant to corrosion [1].

Delamination, the separation of two adjacent plies, has long been considered to be the “*Achilles heel*” of these advanced materials. It may occur due to low-velocity impact events, manufacturing imperfections and stress concentrations triggered by sudden changes in structural details. This failure mode provokes severe reductions in the in-plane stiffness and strength values which results in accelerated growth of damage and premature failure. Also, CF/EP composites become more vulnerable to moisture uptake and contaminant penetration due to delamination. Therefore, delamination resistance of these materials needs to be improved for promoting their widespread acceptance in the aerospace, automotive and wind-energy industries [2].

A number of techniques have been developed and evaluated by the researchers to improve delamination resistance of high performance structural composites. 2½D reinforced materials have been developed, such as through-thickness stitched or pinned composites. In recent years, there has been recent development in 3D composites, in

which fiber preforms are knitted or braided. These developments were shown to be very successful in improving damage tolerance of fiber-reinforced composites. However, it was observed that these modifications result with a significant reduction in in-plane mechanical properties of these composites. In addition, these techniques do not hinder the initiation of damage; only enhance the resistance crack growth once has initiated [3].

The incorporation of micro/nano phases into matrix phase has been also studied in recent years. It is well known that this approach has some disadvantages such as the difficulty of dispersing nano-sized phases into the epoxy matrix and the enormous increase of resin viscosity. The latter especially is a critical problem for all infusion applications. Most recently, interleaving technique, based on insertion of a thermoplastic material at the interlaminar region, has been developed by some researchers. Various interleaf materials such as thermoplastic and thermoset films, non-woven veils and self-same resin interleaf materials have been studied. These interleaf materials may cause resin impregnation problems and thickness increase in the resulting composite structure. They resulted in an unavoidable compromise in tensile, flexural and compression properties at the expense of reduced fiber volume fraction and increased thickness [4].

As an alternative to other techniques, the use of electrospun thermoplastic nanofibers between the primary reinforcing fabrics was proposed by Dzenis and Reneker [5] in 2001. Although the idea is not new, there has been increasing attention devoted to this topic in recent years. Some advantages of this approach are as follows [6];

- Increased interlaminar fracture toughness and impact resistance
- Increased interlaminar shear strength
- Reduced ply delamination
- Enhances resin toughness
- Increased flexural strength
- Increased flexural stiffness

- Virtually no added weight
- Virtually no added thickness

Although, this approach requires an extra-step to manufacturing process of composite laminates, and there is no need for a radical change in the processing route. Therefore, it can be easily adapted to the traditional out-of-autoclave composite manufacturing techniques such as resin transfer molding (RTM), vacuum-assisted resin transfer molding (VaRTM) and vacuum-assisted resin infusion (VARI). Further research is required to provide a better understanding of the effects of thermoplastic nanofiber interleaving on the carbon fiber/epoxy composites which put us one step closer to reaching commercialization stage [7].

1.2. Objectives

The main objective of this thesis is to investigate interlaminar Mode-I fracture toughness of carbon fiber/epoxy composites interleaved by micro and/or nano PA66 nonwoven veils. Also, the effects of electrospun PVA nanofibers on the mechanical properties CF/EP composites were investigated. This study also deals with the effects of aramid nonwoven veils on the mechanical properties of CF/EP composites. The specific objectives are as follows;

- Obtain bead-free polyamide 66 (PA 66) nanofibers by electrospinning method.
- Deposit these nanofibers onto carbon fabrics for pre-determined electrospinning duration.
- Prepare electrospun PA66 nonwoven veils at different areal weight densities.
- Manufacture of reference and PA66 nano-interleaved carbon fiber/epoxy composite laminates by VaRTM technique.

- Determine the mechanical properties of the reference and PA 66 nanofiber interleaved composite specimens.
- Investigate the effect of nanofiber areal weight density on the mechanical behavior of manufactured composites by changing electrospinning duration.
- Manufacture of aramid and PA 66 nonwoven fabric interleaved composites by vacuum infusion technique at different areal weight densities.
- Determine the mechanical properties of the aramid and PA66 nonwoven interleaved composite specimens.
- Compare the toughening performance of micro and nano PA 66 nonwoven veils.
- Carry out numerical simulations to provide an opportunity to investigate the effects of PA66 nanointerlayers on real-life engineered structures.

1.3. Thesis outline

In Chapter I, the background information emphasizes the importance and benefits of thermoplastic nanofiber interleaving technique considering the other techniques studied in the literature. The main objectives of this thesis were also listed at the end of this chapter.

Chapter II starts with a brief overview of composite materials. It is important for the reader to be aware of the basic terminology and definitions, particularly if he/she working in an interdisciplinary environment. Failure modes in composite laminates were discussed and a more detailed description of the phenomenon of delamination was provided. The techniques developed by the researchers to mitigate the delamination problem and arrest the crack propagation were presented and discussed via the findings and important observations of the recent studies in the literature. The principles and

working parameters of electrospinning technology were presented with reviews of some polymeric nanofibers published in literature. A detailed literature review on the micro and nanofiber interleaving was provided in order to better interpret the experimental results of this study. This chapter also provides some important insights but also presents conflicting findings and pointing out certain specific gaps in the literature.

Chapter III is the experimental section of this study. This chapter describes the experimental procedures, equipment, raw materials and chemicals used in this work. Chapter III also explicates the conducted experiments with the relevant ASTM standards. The morphologies of aramid and PA66 nonwoven fabrics, electrospun PVA and PA66 nanofibers were determined by scanning electron microscopy (SEM). Differential scanning calorimetry (DSC) was used for determining the thermomechanical properties of the commercial PA66 nonwovens and electrospun PA66 veils.

Chapter IV presents the results of the experimental program that was conducted to study the effects of aramid, micro and nano PA66 interleaf materials on the mechanical behavior of carbon fiber/epoxy composites. The effects of electrospun PVA nanofibers on the mechanical properties of these composites were presented. SEM analysis was used to deduce toughening mechanisms in the composite specimens. Dynamical mechanical analysis (DMA) was used to determine the glass transition temperature of the composites. The results were also discussed based on the literature given in Chapter II. Following this, the conclusions were drawn.

Chapter V is the numerical part of this study. It starts with the delamination techniques in finite element analysis. This chapter mainly focuses on cohesive zone modeling approach which is used for simulating the delamination in the specimens. Then, numerical studies in the literature which focus on the effects of nanofiber interleaving were discussed. The created FEM model was validated with the literature available then it was applied to simulate the behavior of PA66 interleaved composites under Mode-I loading.

Concluding remarks and an outlook on future studies were presented in Chapter VI. At the end of this chapter, the research papers and spoken conference presentations converted from this thesis were listed.

1.4. Unique contributions

This thesis presents the effects of electrospun PA66 nanofiber interleaving on the mechanical performance of carbon fiber/epoxy composites. To our knowledge, there are only a few studies reported in the literature on the investigation of the effects of nanofiber interleaving of the carbon fiber/epoxy composites manufactured by vacuum-infusion method. Additionally, no reports have been published in the literature on the compressive properties of unidirectional carbon fiber/epoxy composites interleaved by PA 66 nanofibers. Also, this is the first study in which electrospun PVA interleaved composites were manufactured and tested under different loading conditions. This study was intended to contribute to the literature and provide better understanding how these composites behave when they are interleaved by different types of thermoplastic nanofibers.

In this thesis, the effects of commercial aramid and PA 66 nonwoven veils on the mechanical performance of carbon fiber/epoxy composites were also investigated. To date, a few studies focused on the effects of these veils on Mode-I fracture toughness of laminated composites. However, there are still question marks over the effects of these veils on the mechanical properties of those composites. Additionally, the effects of aramid nonwovens on the mechanical properties of CF/EP composites are still unknown. Thermomechanical behavior of these composites was unrevealed in this thesis. Thus, this study opens new perspectives and provides a more comprehensive view in understanding of the roles of micro and nano interleaving on the improvement of mechanical performance of laminated composites.

This thesis also deals with the application of Cohesive Zone Modeling (CZM) approach to study Mode-I fracture toughness of reference and PA66 nonwoven veil interleaved composite specimens. A finite element model was also developed to

simulate the delamination behavior of composite specimens under Mode-I loading. The sensitivity of the cohesive zone parameters in predicting the overall mechanical response was first examined; then, cohesive parameters were tuned comparing numerical simulations of the load-displacement curve with experimental results. The successful use of CZM to predict damage initiation and propagation of the composite specimens was described which may help other researchers to deal with such problems.

CHAPTER 2

FUNDAMENTAL CONCEPTS AND RELEVANT LITERATURE

2.1. Introduction to Composite Materials

Composite materials are the most extraordinary engineering materials known to human beings. Although they can be engineered as an alternative to other traditional materials such as steel and aluminum, they are not a human invention. Almost all the materials around us are composites. Woods, bones, stones, etc. are natural composites and they exist in nature or developed by natural processes. Wood is made of cellulose fibers and lignin (phenolic resin). The bone in our body is also a composite. It is made of mineral fibers with high elastic modulus embedded in a soft protein known as collagen. For thousands of years, composite materials have been used in various structural and non-structural applications. Around 3000 B.C., the ancient Egyptians used mud and straw to form the most primitive man-made composite materials in history. The mud gathered from the Nile River was mixed with chopped straw fibers in a pit (mould) and sun-dried (cured) to make stronger bricks for construction. Straw is strong under tension, and dry mud is good at resisting compressive forces. The combination of these materials at a microscopic scale exhibits better performance than the mud alone in both under tension and compression (Figure 2.1.1) [8-9].

In the 12th century, Mongol warriors used bamboo, cattle tendons, horns, and pine resin to craft more flexible and powerful composite bows. They used the cattle tendons on the tension side and sheets of horn were placed on the compression side of the bow over a bamboo core. This composite system is considered as one of the first applications of a special form of laminated composites called composite sandwich structures. Mongolian bows were the most advanced and powerful weapons on the earth until the firearms were developed in the 14th century [10].

The modern era of composites began with the development of modern plastics in the early 1900s. The first synthetic plastic, Bakelite, was invented followed by the development of other plastics such as vinyl, polystyrene, phenolic and polyester. However, these synthetic plastic resins could not exhibit enough mechanical strength for more demanding structural applications. Stronger reinforcement materials were necessary to give additional strength and rigidity for these applications. Fiber glass was first introduced by the Owen Corning Corporation in the 1930s. This is considered as the beginning of the Fiber Reinforced Polymers (FRP) industry [11].

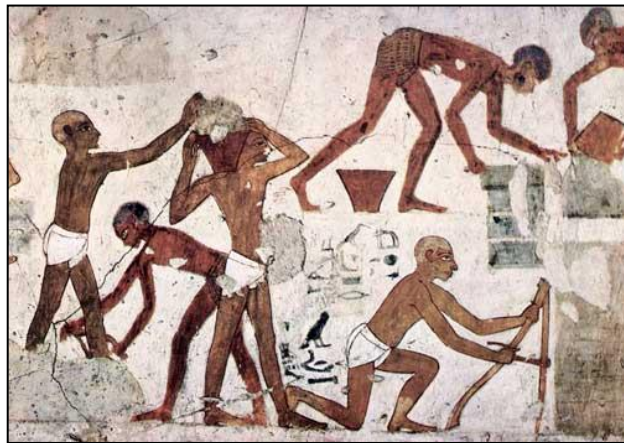


Figure 2.1.1. The process of ancient Egyptian brick making [12].

In early 1950's, various composite manufacturing techniques such as pultrusion, vacuum bag molding, and filament winding were developed. The industry began to mature between the early 1960s and the mid-1970s. Better plastic resins and improved reinforcing fibers were developed in response to demands for lighter and stronger materials in different industries. The first aramid fiber (Kevlar®) was introduced by DuPont in the early 1960s and it has become the best material choice for body armor and tactical vests due to its high tensile strength, density and light weight. Carbon fibers were developed around the same time and started to being used in sporting goods in the 1970s. As the carbon fiber industry matured during the 1980s and costs began to decrease, carbon fibers found wide applications in alternate energy, fuel-efficient automobiles, and construction/infrastructure and oil exploration. Since the 1990s, carbon fiber reinforced polymer composites (CFRPs) have been widely used in defense,

aerospace and construction/infrastructure systems and also have been used in luxury automobiles, wind turbines and gas storage tanks (Figure 2.1.2) [13].



Figure 2.1.2 Some of structural applications of CFRPs [14].

2.1.1. Definition of a composite material

A general definition of composite material is “a combination of two or more dissimilar constituents at a macroscopic level that provides better properties than those of the individual constituents used alone”. Contrary to metallic alloys, each constituent retains its own chemical, physical and mechanical properties and remains distinguishable at the microscopic scale in the composite (Figure 2.1.3) [15].

Composite materials have three main characteristics; (i) macroscopically non-homogenous materials with a distinct interface, (ii) combination of constituents should result in significant property changes, (iii) the property of one constituent is much

greater (≥ 5) than the other (iii) the volume fraction of each constituent is higher than 10% [16].

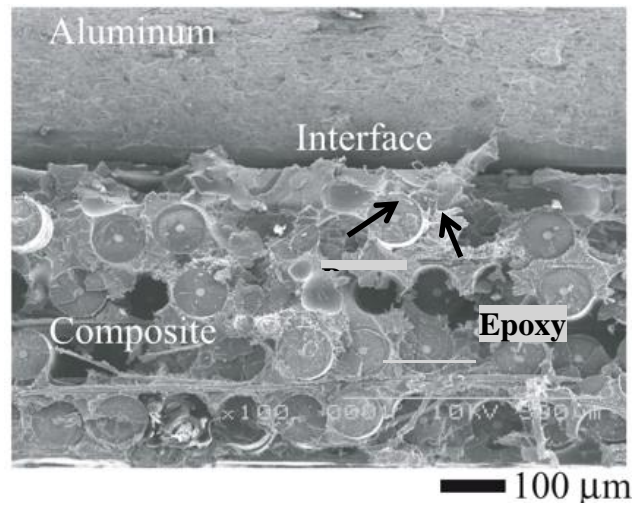


Figure 2.1.3. SEM image of a hybrid composite structure made of boron fiber/epoxy and aluminum layer [17].

2.1.2. Components of composite materials

Modern composites are usually made of two phases; reinforcing phase and matrix phase (Figure 2.1.4). The reinforcing phase provides strength and stiffness. The matrix material acts as a medium to transfer the load to the reinforcement and gives ductility and toughness to the composite material.

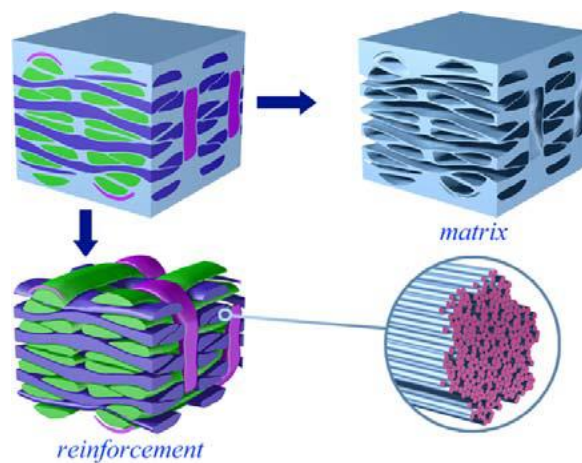


Figure 2.1.4. Material structure of a 3D woven composite [18].

The matrix material also protects the reinforcement from the external loads and environmental damage and provides finish, texture, color, durability and functionality to the composite product. It also carries transverse and interlaminar shear stresses in the composite. Stresses acting on the matrix are transmitted to the reinforcement across the interface. Therefore, the performance of the interface is a critical issue which determines the overall composite performance in particular fracture toughness. Too weak an interface gives low composite strength and stiffness; too strong and the composite will be brittle.

2.1.3. Classification of composite materials

Composite materials can be divided into two main categories based on the geometry of reinforcing phase and the type of matrix phase. Figure 2.1.5 shows the classification of composite materials.

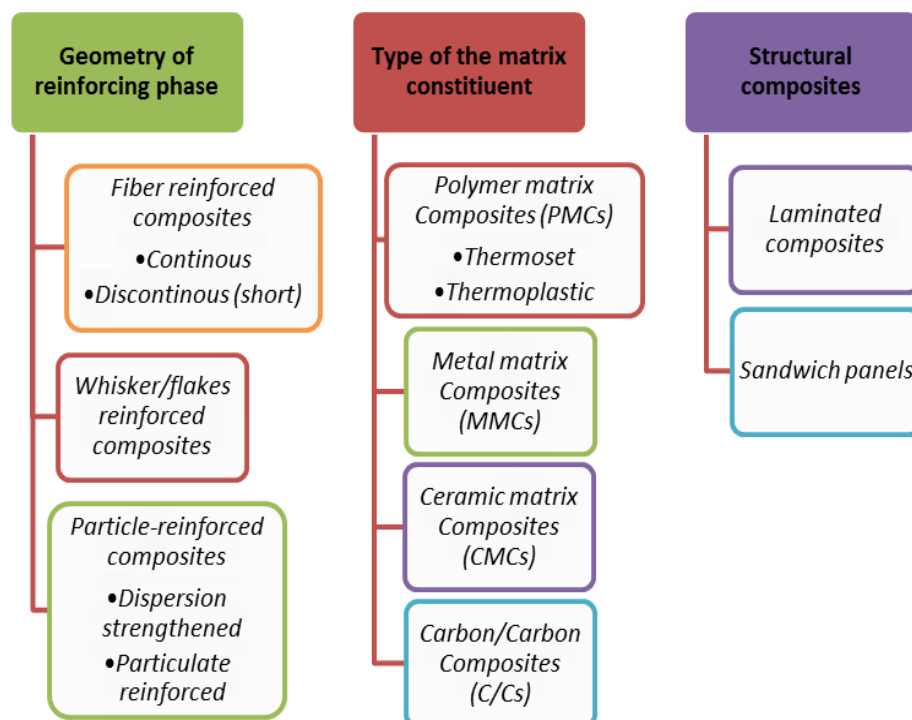
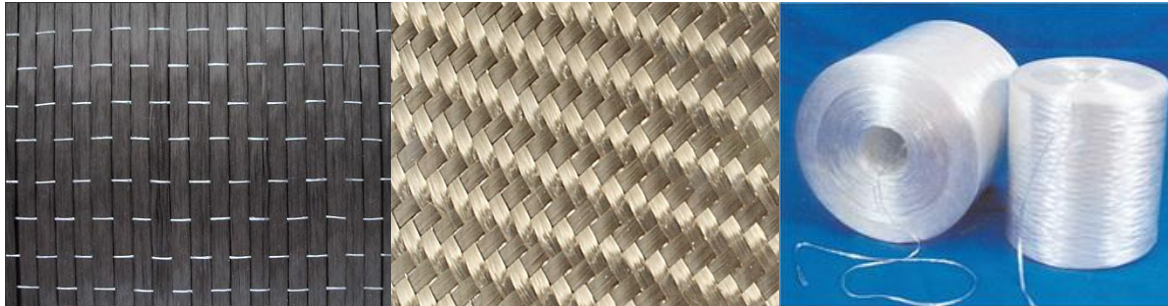


Figure 2.1.5. Classification of composite materials.

Fiber reinforced composites can be classified as either continuous or discontinuous. Continuous-fiber composites normally have a preferred orientation, while discontinuous fibers generally have a random orientation. Examples of continuous reinforcements include unidirectional, woven cloth, and helical winding, while examples of discontinuous reinforcements are chopped fibers and random mat (Figure 2.1.6) [19].

CONTINUOUS REINFORCEMENTS



Unidirectional (UD)

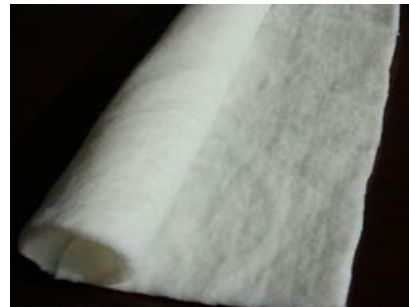
Woven

Rovings

DISCONTINUOUS REINFORCEMENTS



Short fibers



Mat

Figure 2.1.6. Continuous and discontinuous reinforcements [20].

Continuous-fiber composites are often assembled into laminated composites by stacking of continuous plies to obtain desired the strength and stiffness properties at preferred orientations (Figure 2.1.7). A unidirectional composite laminate (Figure 2.7a) are very stiff and strong in the longitudinal direction but very weak in the transverse direction. This is due to the fact that the applied load is carried by the polymeric matrix in this direction. In more detail, the longitudinal tension and compression loads are carried by the continuous fibers while the matrix is the primary load carrier for interlaminar shear and transverse (90°) tension. The roles of the fiber and the matrix in mechanical properties are presented in Table 2.1. Quasi-isotropic laminates (Figure 2.7b) exhibit isotropic in-plane response but they do not behave isotropically under the action of out-of-plane loading [19, 21].

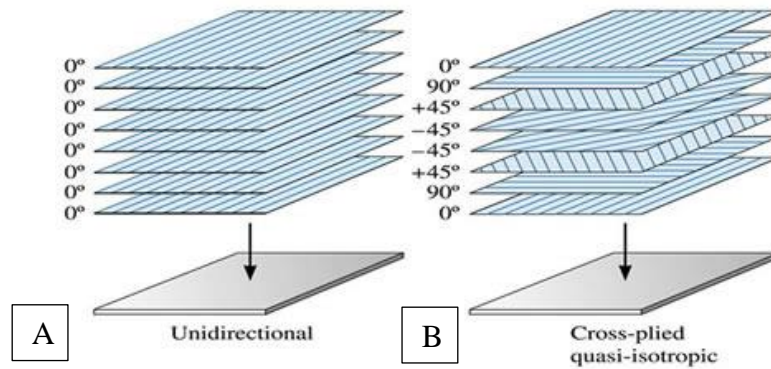


Figure 2.1.7. Examples of composite laminates oriented at different orientations [22].

Table 2.1. The roles of the fiber and the matrix in mechanical properties [19]

Stacking sequence	Mechanical property	Fiber	Matrix
<i>Unidirectional</i>	<i>0°-tension</i>	✓	---
	<i>90°-tension</i>	---	✓
	<i>0°-compression</i>	---	✓
	<i>90°-compression</i>	---	✓
	<i>0°-flexural</i>	✓	---
	<i>90°-flexural</i>	---	✓
	<i>Shear</i>	---	✓
	<i>Interlaminar shear</i>	---	✓

Discontinuous fibers, also known as short fibers, are 0.3 cm or less in length and placed into a matrix randomly. Due to this random orientation, the resulting composite behaves more isotropically than the composite made of continuous fibers. Discontinuous fibers are generally used to produce composite parts with irregular shapes in the composite industry [23].

Whiskers, very thin single-crystals made of SiC (Figure 2.1.8a), can be also used as reinforcement material. Whiskers are used to increase crack-resistance of brittle ceramic matrices. Different toughening mechanisms are observed such as whisker pull-out (Figure 2.1.8b), whisker bridging (Figure 2.1.8c) and crack deflection in the

resulting composites. Although whiskers do not have the same reinforcing potential of continuous fibers, the manufacture of whisker reinforced composites is easier than the other types of composites [24].

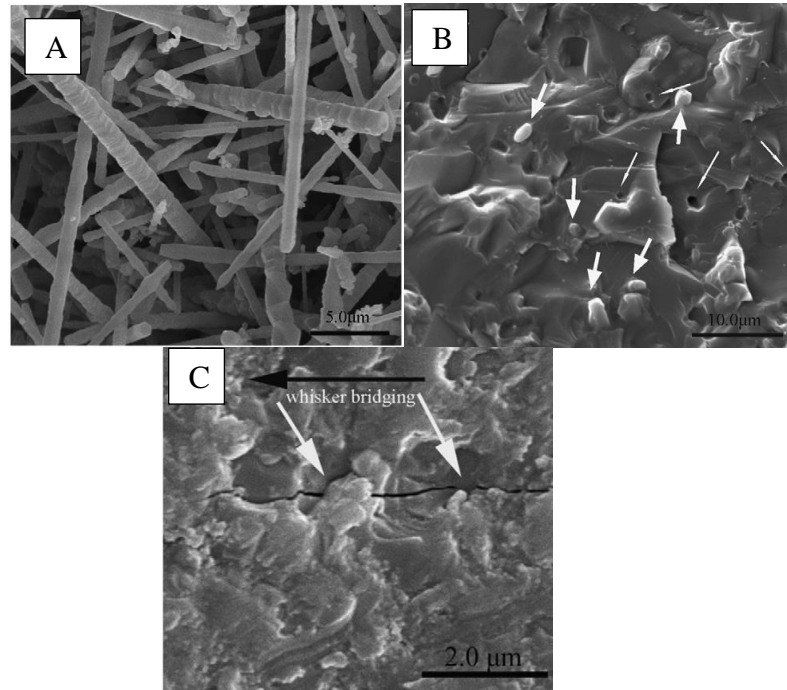







Figure 2.1.8. (a) SEM image of SiC whiskers and (b) whisker pull-out and (c) whisker bridging phenomena observed in ceramic matrix composites [25].

Particle reinforced composites is divided into two main categories; (i) In dispersion-strengthened composites, particles are of 0.01-0.1 μm in size. The strengthening occurs at atomic/molecular level like precipitation hardening observed in metals so that the matrix carries the major portion of an applied load, while dispersoids hinder/impede dislocations. (ii) Particulate composites are other class of particle-reinforced composites. Polymers are frequently reinforced with various micro/nano particles such as carbon black, graphene nanoplatelets and carbon nanotubes etc. These composites are designed to obtain the best combination of different properties, for instance, adding graphene to polymers can improve not only the mechanical properties but also electrical and thermal properties of the resulting nanocomposites [26, 27].

Polymers, metals and ceramics are commonly used as the matrix. Polymer matrix composites (PMCs) are being extensively used in many applications due to their unique advantages such as high weight-saving potential, high specific strength and stiffness, good fatigue and corrosion resistance. They are composed of short or

continuous fiber reinforcement and an organic polymer matrix. In a ceramic matrix composite (CMC), the reinforcement is added to the matrix for improving the fracture toughness on the other hand the reinforcement provides high strength and stiffness in a PMC. The matrix properties determine the resistance of the PMC to most of the degradative processes that eventually cause failure of the structure. These processes include impact damage, delamination, water absorption, chemical attack, and high-temperature creep. Thus, the matrix is typically the weakest link in the PMC structure. The matrix phase of commercial PMCs can be classified as either thermoset or thermoplastic. Thermosetting resins include polyesters, vinyl esters, epoxies, polyurethane. Thermoplastic resins, sometimes called engineering plastics, include polypropylene, polyamide, polyethylene and polyether-etherketone (PEEK). Figure 2.1.9 shows the comparison of general characteristics of thermoset and thermoplastic matrices used in composites [28, 29].

Figure 2.1.9. Comparison of thermoset and thermoplastic matrices [30].

Resin type	Process temperature	Process time	Use temperature	Solvent resistance	Toughness
Thermoset	Low	High	High	High	Low
Toughened thermoset					
Lightly crosslinked thermoplastic					
Thermoplastic	High	Low	Low	Low	High

Typical fiber reinforcements used in PMCs are glass fiber, carbon fiber, and Kevlar® fibers. Glass Fiber Reinforced Plastics (GFRP) are generally used for lower performance applications in the composite industry due to their low cost and high availability. Carbon fiber reinforced Plastics (CFRP) are being used in advanced high performance applications due to its very high specific modulus and strength, excellent durability and low thermal shrinkage. Almost ¾ of carbon fibers reinforce an epoxy matrix. Table 2.2 shows the comparison of different fibers used in composites [31].

Table 2.2. Comparison of different fibers used in composites [32]

Mechanical property	Carbon	E-glass	Aramid
<i>Tensile strength</i>	very good	very good	very good
<i>Compressive strength</i>	very good	inadequate	good
<i>Elastic modulus</i>	very good	good	adequate
<i>Long-term behavior</i>	very good	good	adequate
<i>Fatigue behavior</i>	excellent	good	adequate
<i>Bulk density</i>	good	excellent	adequate
<i>Alkaline resistance</i>	very good	good	inadequate
<i>Price</i>	high	low	high

Although, composites are still overshadowed by glass fibres (85%), but carbon fibres are experiencing strong growth. Figure 2.1.10 clearly shows that the demand of CFRPs has been a continuous growth since 2013. In 2020, CFRPs across all applications will comprise a \$35 billion market, including \$6 billion in automotive CFRPs. People have recently used them in mass market applications under the influence of two factors [33]:

- Prices have dropped significantly and there are an increasing number of suppliers.
- The demand is high for lightweight products that consume less energy (motor vehicles, aviation, wind energy, electronics, etc.)

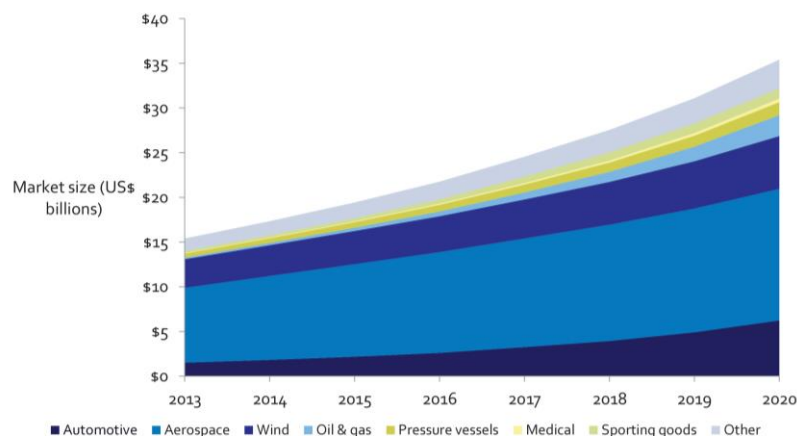


Figure 2.1.10. CFRP composites market forecasts to 2020 [34].

2.1.4. Manufacturing techniques for FRP composites

There are numerous methods for manufacturing FRP composite components. Figure 2.1.11 shows the classification of manufacturing techniques used for FRP composites. In this thesis, vacuum-assisted resin transfer molding (VaRTM) was used to manufacture of carbon fiber reinforced/epoxy composite laminates. Therefore, this technique is explained in more details in coming paragraphs.

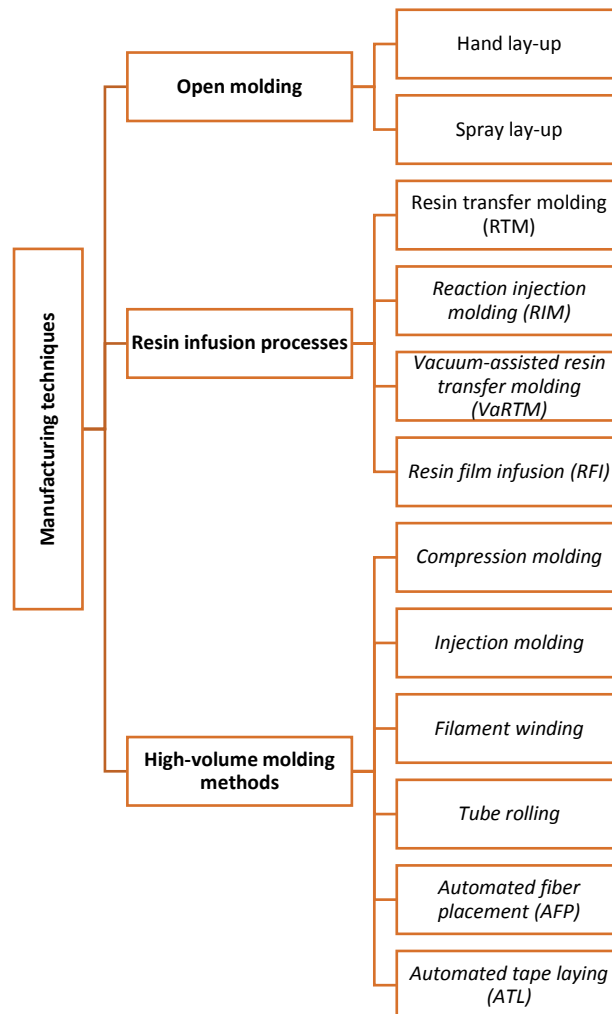


Figure 2.1.11. Classification of composite manufacturing techniques.

Vacuum-assisted resin transfer molding (VaRTM) is one of resin infusion processes that use vacuum pressure to drive resin into a laminate. Due to high strength to weight ratio, design flexibility and excellent cosmetic finish, VaRTM method has been widely used for the manufacture of large-scale energy and military and marine

composite structures. Recently, VaRTM method has been started to use for structural aerospace composites with the advancement of infusible toughened epoxies and automation equipment. Figure 2.1.12 shows some of the recent aerospace structures made by this method [35].



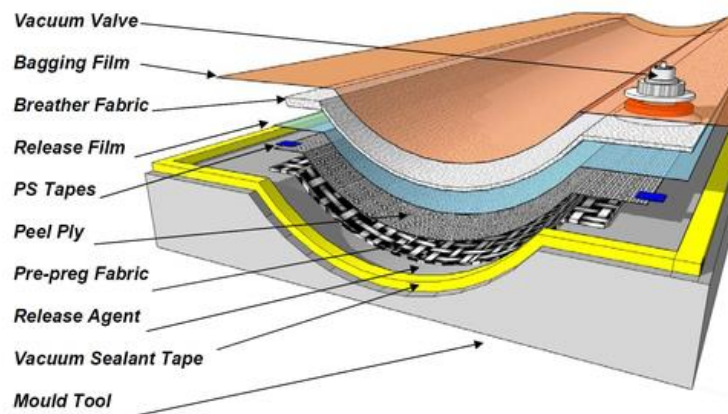
Figure 2.1.12. Recent applications of VaRTM method for aerospace component production [35].

Figure 2.1.13(a) and Figure 2.1.13(b) show schematic representation of VaRTM set-up and experimental VaRTM set-up respectively. VARTM technique consists of four main steps [36];

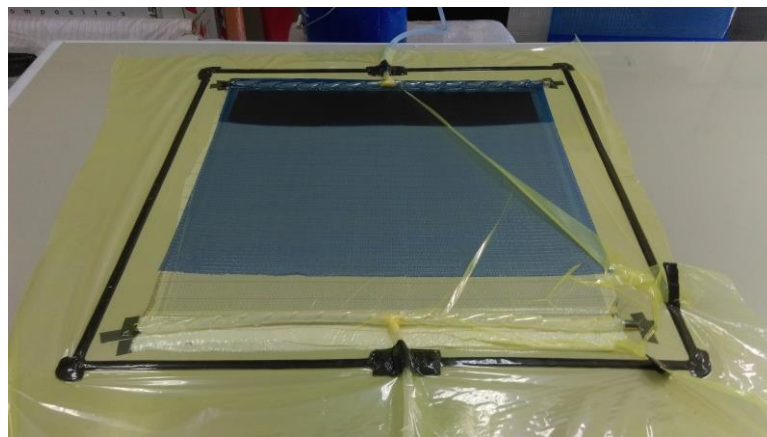
- (i) Placement of the dry reinforcement fabrics into mold cavity,
- (ii) Resin injection,
- (iii) Curing and
- (iv) Demolding.

The process starts with the placement of reinforcement fabrics on a flat surface after the application of release agent on the surface. Then, a peel ply material made of Teflon-treated nylons is placed over these fabrics. A highly permeable distribution

media which induces the resin flow through the thickness is applied on the top of the peel ply. To designate resin permeability, different types of distribution media in various pore geometries such as sphere or triangular can be used. Then, the breather and bleeder layer, surface-treated polyester mat, are applied to provide continuous air path for vacuum and absorbs excess resin bleeding. Finally, the composite is closed and sealed inside a flexible vacuum bag using gum sealing tape. The resin is injected by vacuuming the air out of the mold cavity through one or more inlet ports depending on the geometry and size of the part [37].



(a)



(b)

Figure 2.1.13. (a) Schematic representation of VaRTM set-up and (b) experimental VaRTM set-up [38].

Bag leaks are the most common problem observed in VaRTM process. They may occur due to a defect in the vacuum-bag or improper handling at the sealing-bag interface before resin infusion. Bag leaks may cause dry-stop formation in the resulting laminate which directly affects the mechanical performance and poor surface quality.

2.2. Failure and damage mechanisms in unidirectional composites

The ultimate failure of a composite is triggered by a number of local failures which occur before it is completely fragmented into two or more pieces. The local-level failure is called as “damage”. Here, the term “local” stands for the individual constituent materials- fiber and matrix. Thus, damage in case of fibrous composites is a micro-level event. The failure at lamina/laminate or macro-level is the ultimate result of the local failures. Due to loading conditions, different types of micro-level damage mechanisms can be observed [39].

Figure 2.2.1 shows the micro-level damage mechanisms observed in a fiber reinforced epoxy composite. Fiber failure (A) occurs when the composite is loaded in the fiber direction within a few degrees. It may also occur under shear loading when the shear stress or strain is higher than the allowable shear stress or strain. Fiber pullout (B) occurs under tension in the fiber direction when the bonding between fiber and matrix is weak [39].

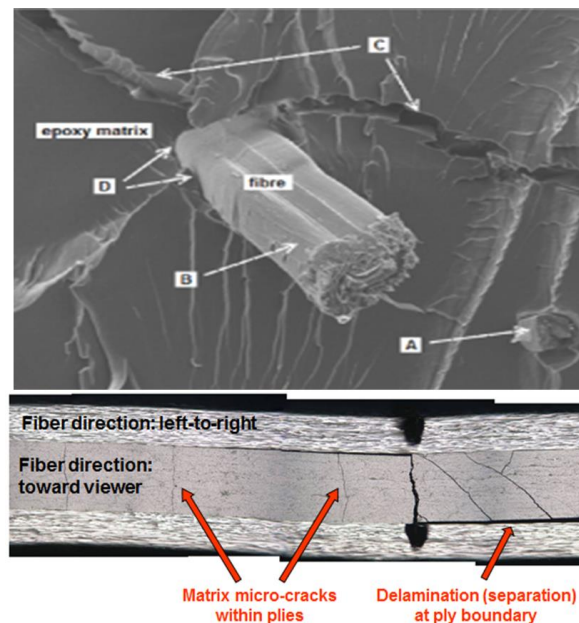


Figure 2.2.1. Damage mechanisms observed in composite materials [40].

Matrix cracking (C) can develop under different loading conditions such as tensile, fatigue, thermal and impact events. The cracks can be either perpendicular or parallel to the fiber direction. Matrix cracks parallel to the fiber direction cause

significant reduction in stiffness whereas the matrix cracks perpendicular to the fiber direction cause less stiffness degradation. However, the matrix perpendicular cracks are more dangerous in terms of structural safety. Because the failure often goes undetected and occurs catastrophically. Matrix cracks in the through thickness direction may lead to delamination (Figure 2.2.1). Fiber-matrix debonding (D) is the separation of the fiber from the matrix. It usually appears as a gap between the fiber and the surrounding matrix. It indicates poor or ineffective contact between the reinforcement and the matrix. The main concern of this thesis is the delamination toughness of carbon fiber/epoxy composites. Therefore, delamination phenomenon and the main reasons of delamination will be explained in the following section [39, 41].

2.3. Delamination

Delamination, one of the macro-level damage mechanisms, has long been considered to be the “Achilles heel” of composite materials. It may occur due to low-velocity impact events, manufacturing imperfections and stress concentrations triggered by sudden changes in structural details. This failure mode provokes severe reductions in the in-plane stiffness and strength values which results in accelerated growth of damage and premature failure. Also, CF/EP composites become more vulnerable to moisture uptake and contaminant penetration. Figure 2.3.1 shows the main reasons for delamination damage which can be classified briefly as follows [2-4, 39];

- (i) Manufacturing defects: This is the most common reason for delamination in a unidirectional composite laminate. Improper ply stacking, insufficient curing temperature and duration, air pockets and dry spots are some of the manufacturing defects causing delamination.
- (ii) Transverse/interlaminar stresses can cause the formation of local delamination.
- (iii) Laminate geometry: Free edges, cutouts, ply drop-offs may cause three dimensional stress state and trigger the delamination failure.

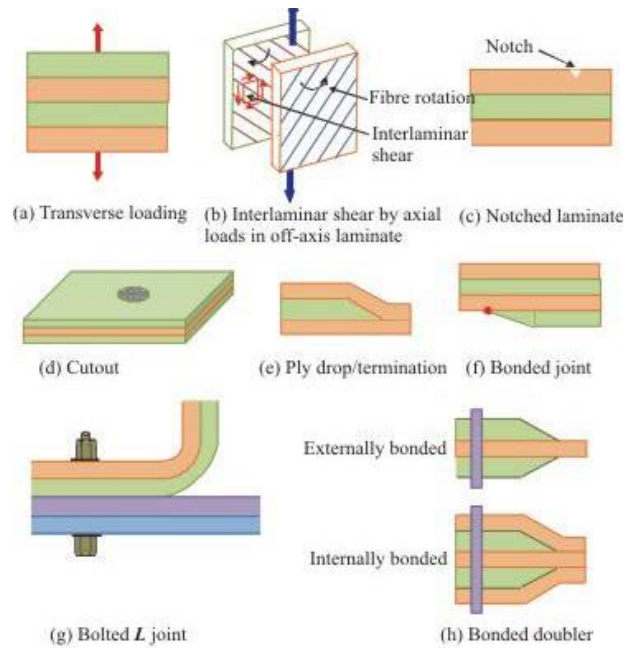


Figure 2.3.1. Damage mechanisms observed in composite materials [39].

2.3.1. Suppression of delamination and toughening mechanism in composite materials

Delamination in fiber-reinforced composites develops in three basic modes of interlaminar fracture. There are three modes of delamination fracture, *i.e.*, Mode I (opening mode), Mode II (sliding mode) and Mode III (tearing mode). Schematic illustration of these fracture modes were shown in Figure 2.3.2. Fiber reinforced composite laminates are generally subjected to combinations of mode I and mode II during their service life [42].

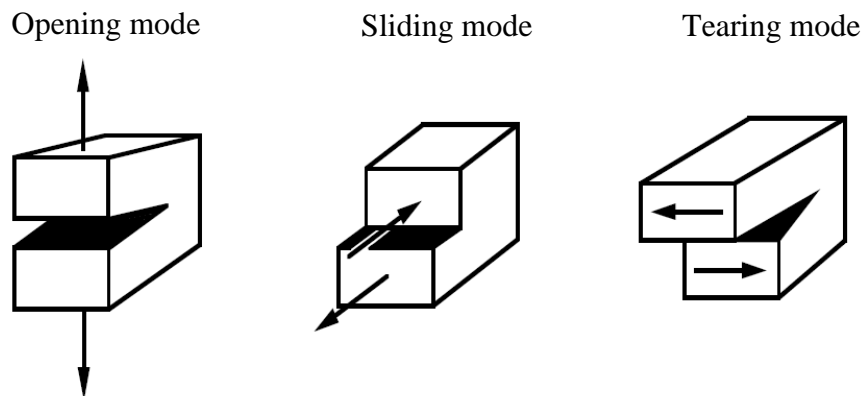


Figure 2.3.2. Three modes of delamination fracture [42].

The focus of various researchers has been the improvement of the delamination resistance of high performance fiber reinforced composites. A variety of toughening mechanisms have been used to improve fracture toughness of fiber reinforced composites. The most common toughening mechanisms in composite materials are [42];

(i) Modulus transfer

(ii) Crack deflection

(iv) Crack bridging

(v) Fiber pull-out

(vi) Crack shielding

Modulus transfer can be defined as the placement of continuous fibers with high elastic modulus in a less stiff matrix material. The stress is transferred to the fibers via matrix material. The main portion of the load was carried by the high stiff reinforcement material. Crack deflection is the formation of new surfaces as the crack propagates in the interlaminar region. Dispersing different types of materials such as particles, plates, whiskers, or chopped fibers leads to an increase in crack deflection which results in higher fracture toughness. Crack bridging is the bridging of the crack surfaces behind the crack tip by using reinforcing phase. It is the major toughening mechanism in the fiber reinforced composites. Fiber pull-out generally forms with the crack bridging mechanism and effectively increases the fracture toughness. Crack shielding occurs when microstructural changes in the composite reduce the intensity of the crack tip stress [42].

There are three different approaches to activate the aforementioned toughening techniques for preventing the delamination failure in fiber reinforced composites; (i) mechanical approach and (ii) material approach and (iii) interleaving approach.

In the following subsections, these approaches will be presented and discussed via the findings and important observations of the recent studies in the literature [42].

2.3.1.1. Mechanical approach

Mechanical approach includes stitching, z-anchoring, weaving and braiding of the composite plies. Stitching is the through-thickness application of high-tensile-strength yarns made of glass, carbon or Kevlar using an industrial sewing machine. The yarns in the composite act like a bridging element and keeping the plies together as shown in Figure 2.3.3. Stitching can be performed on both dry fabrics and uncured prepregs. However, the sewing of prepreg tape is very difficult to achieve because the needle action is restricted by the tackiness of the uncured resin matrix. Different types of stitch patterns are being used for improving mechanical properties of FRPs. Generally, lock stitch is used in order to reduce in-plane fiber disorientations within the composite. The most important stitching parameters are stitch pattern, stitch density (stitch spacing), thread material, stitching direction [43-45].

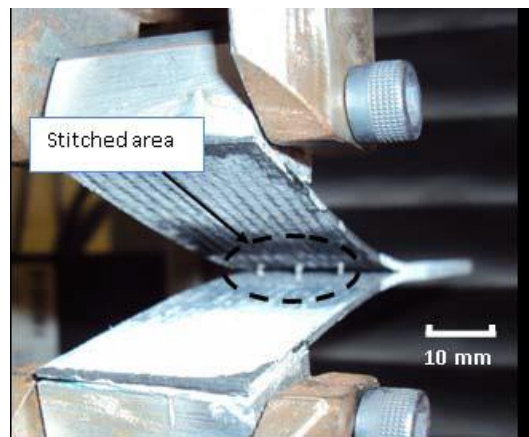


Figure 2.3.3. A stitched composite specimen under Mode-I loading [46].

There are many studies investigating the effect of through-the-thickness stitching on the mechanical performance of FRPs. Sharma and Sankar [47] showed that Mode I fracture toughness was 15 – 30 times higher than that of unstitched laminates, while Mode II fracture toughness increased by 5 – 15 times in the presence of stitching. Although stitching can dramatically enhance damage tolerance, stitching causes local fiber misalignment, resin-rich sites and voids around the stitch thread within the

composites. These defects reduce significantly in-plane mechanical properties of composites (Figure 2.3.4). Kan and Lee [48] showed that increasing stitch density reduces by approximately 45% the tensile strength and 30% tensile modulus of the laminate. Yun et al. [43] showed that the open-hole compressive strength of stitched laminate decreased while open-hole tensile strength increased as compared to the unstitched laminates. Yudhanto et al. [49] proved that stitching generally reduces the compression strength of carbon/epoxy composites of up to 16%.

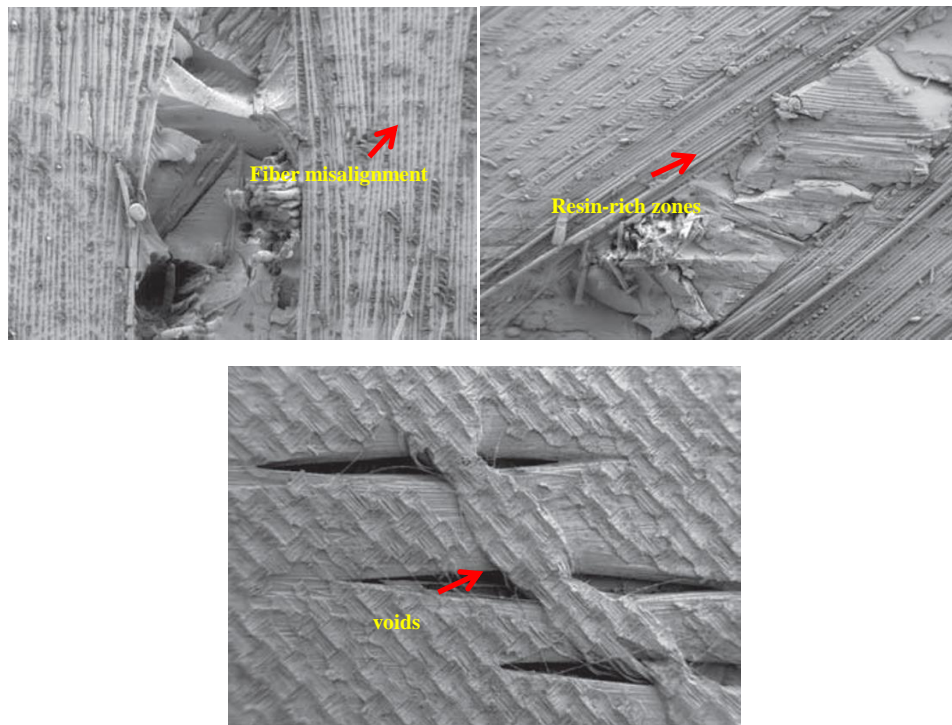


Figure 2.3.4. Microstructural defects caused by stitching process [2, 3].

Z-anchoring is the application of high stiff and very thin z-pins through the thickness of a composite. This technique can be only used for reinforcing prepreg laminates. Figure 2.3.5 shows the manufacturing steps of z-anchoring process. The collapsible preform consists of z-pins is placed on the laminated prepregs. Then, the z-pins are inserted to the laminated prepregs by using an ultrasonically actuated tool during autoclave curing process. After the application of the z-pins, the preform and the excess z-pin are removed by a cutter [50].

Delamination toughness is the most extensively studied property of z-pinned laminates by the researchers. It was shown that delamination toughness is significantly improved about 5 times when the z-pin density is 2% [51]. The reason for this increase

is that the formation of a bridging traction zone due to z-pins behind the delamination crack front. Figure 2.3.6 shows the effect of percentage volume content of z-pins on the mode I interlaminar toughness. The improved delamination resistance often results in higher impact and post-impact properties. Zhang et al. [52] found that z-pinning reduced the impact damage area by 19–64%, depending on the impact energy level and laminate thickness. Childress and Freitas [53] measured reductions of 30–50% in the amount of damage sustained by hailstone impacts.

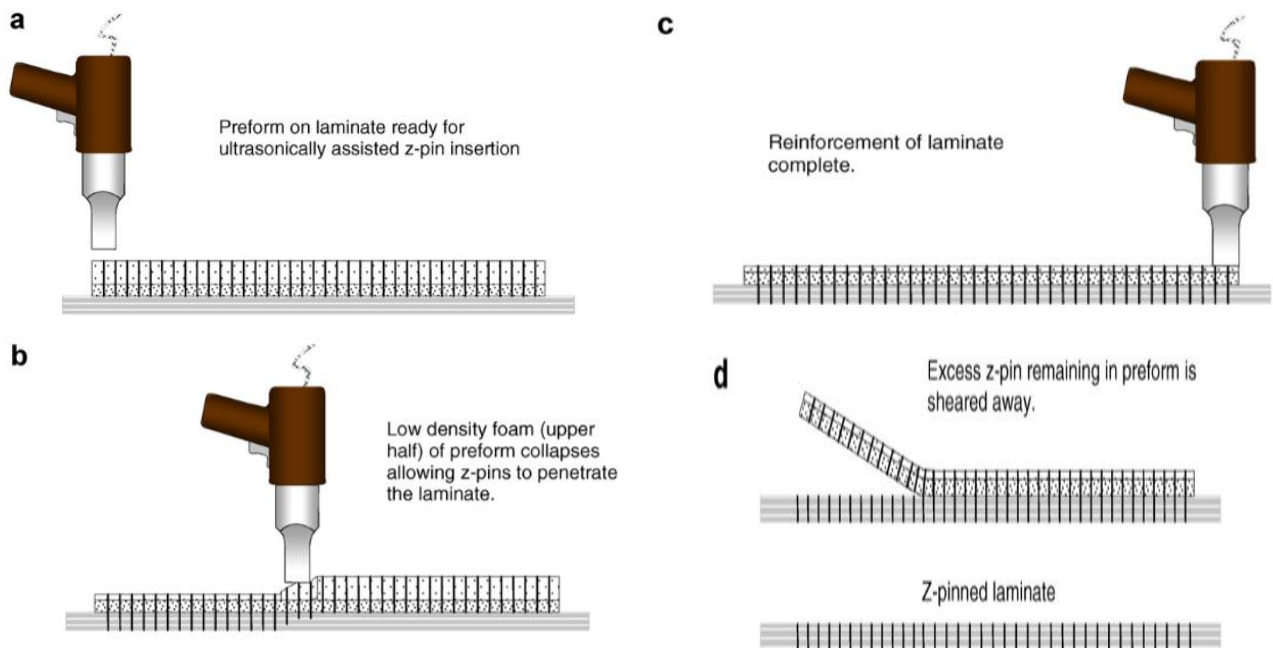


Figure 2.3.5. (a) Manufacturing steps of z-anchoring [50].

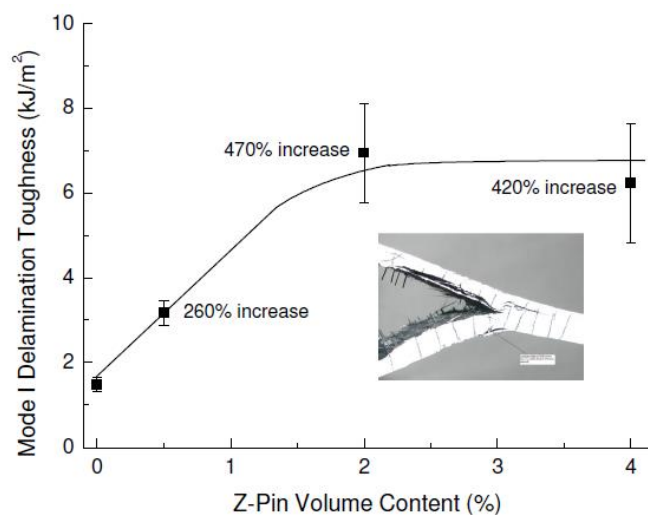


Figure 2.3.6. (a) Effect of z-pin volume content on the Mode-I fracture toughness [50].

The biggest problem of this process is that z-anchoring causes significant reduction in stiffness, strength and fatigue life. The reason was the formation of microstructural defects around the z-pins (Figure 2.3.7). The effect of z-pinning on the in-plane elastic properties of laminates was studied by using material testing and finite element method in the literature. The reduction of the elastic properties is the highest for unidirectional laminates and becomes less and less severe when the percentage of load-bearing 0° fibers in the laminate is reduced. The in-plane tensile, compressive and bending strengths were found to be reduced by z-pinning. Stringer and Hiley [54] measured a 20% reduction of the tensile failure stress of a carbon/epoxy laminate reinforced with z-pins. Steeves and Fleck [55] studied the effect of z-pins on the compression properties of unidirectional and cross-ply carbon/epoxy laminates. No significant change observed in compression strength of z-pinned cross-ply specimens as compared to the control specimen. On the other hand, unidirectional z-pinned specimens are experienced about 33% reduction in compression strength against the control specimens.

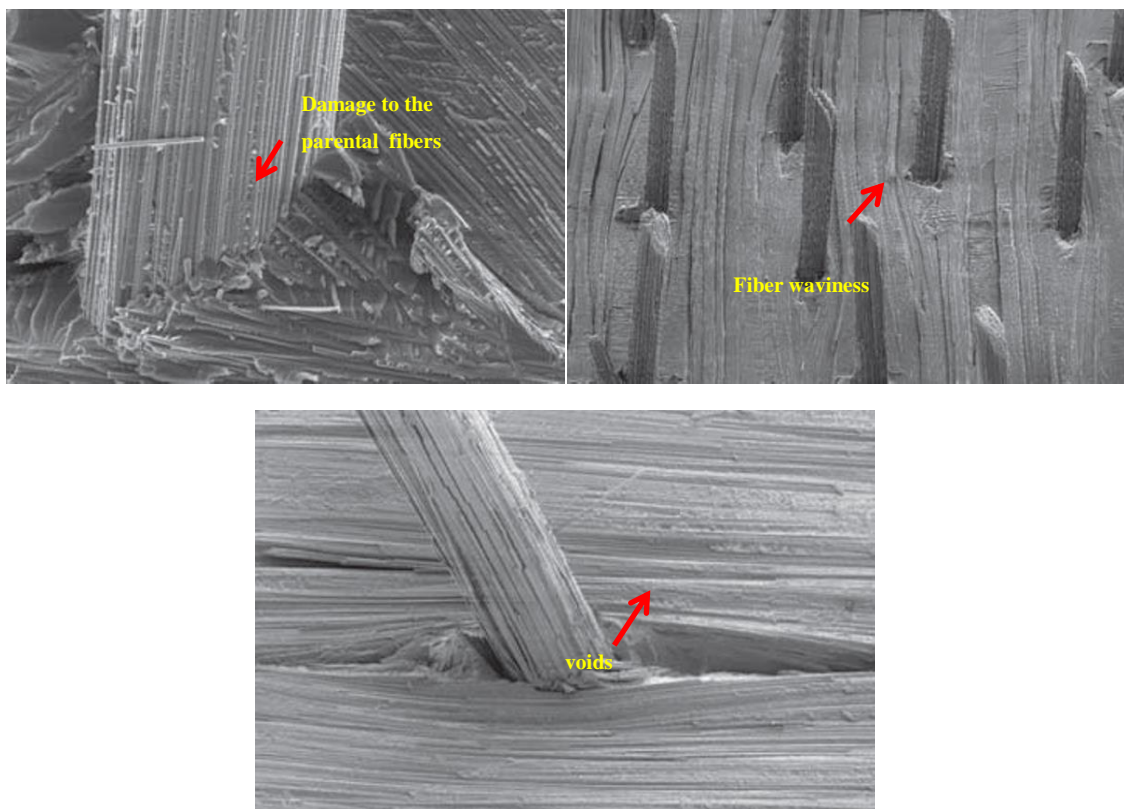


Figure 2.3.7. Microstructural defects caused by z-anchoring operation [2, 3].

2.3.1.2. Material approach

The use of nano-sized particles as reinforcement of polymer composites has attracted great attention of researchers due to their superior mechanical, electrical, optical and thermal properties. In material approach, different types of micro or nano-sized fillers such as alumina, silica, carbon black, graphene, carbon nanotubes (CNTs) are mixed/stirred/sonicated (Figure 2.3.8) with the matrix phase for improving delamination resistance.

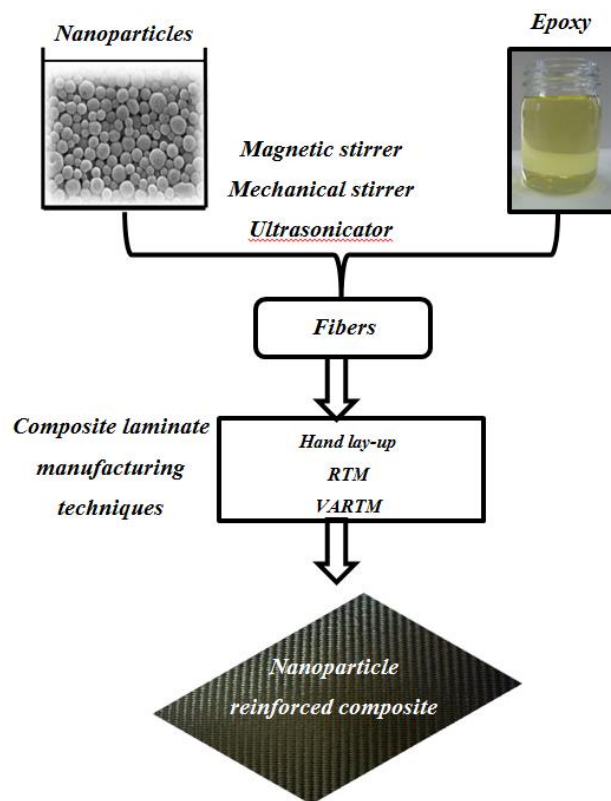


Figure 2.3.8. Manufacturing steps of a nanoparticle reinforced composite.

The increase in IFT achieved by filler addition can be in the range between 15-100% depending on the filler type and its content in the resin. Yokozeki et al. [56] showed that the IFT of composite laminates containing short cup-stacked carbon nanotubes (CSCNTs) was 200% higher than the unmodified ones. Recently, Ragosta et al. [57] used silica nanoparticles to toughen epoxy matrix and obtained 288% increase in IFT of composites. Particle debonding with subsequent plastic void growth and

matrix shear banding are found to be the main toughening mechanisms of nanosilica filled composites. To the best of authors' knowledge, this is the highest improvement reported in the literature.

Polymer nanofibers are also possible candidates to modify epoxy matrix due to their unique physicochemical properties such as large specific surface area, excellent adhesion and superior mechanical properties. More than 100 polymers have been electrospun into nanofibers with different morphologies. Recently, Phong et al. [58] examined if PVA electrospun nanofibers (nPVA) were applicable to epoxy matrix for modifying carbon/epoxy composites. nPVAs were dispersed into the epoxy matrix with different contents by using a process homogenizer at very high speed (15,000 rpm) then the mixture was sonicated by using an ultrasonic homogenizer. The results were so encouraging that the initiation and propagation interlaminar fracture toughness in Mode I was significantly improved by about 65% and 73%, respectively. There was a slight increase of the tensile strength by about 5%. The fatigue life of the modified composite was extended 10-30 times.

Although this approach is moderately effective for improving mechanical performance of composite structures, it has some clear drawbacks such as enormously increased resin viscosity and non-uniform distribution of fillers in resulting laminates due to the filtration effects of reinforcing fabrics during the resin infusion.

2.3.1.3. Interleaving technique

Most recently, interleaving technique, based on insertion of an interleaf material at the interlaminar region, has been developed by some researchers. Various interleaf materials such as thermoplastic and thermoset films, non-woven veils and self-same resin interleaf materials have been studied. Compared to filler toughening, this technique does not increase the uncured resin viscosity and the veil fibers are uniformly distributed in the resulting laminate. The use of toxic and/or harmful, and also expensive fillers such as CNTs and graphene is not necessary in this technique. Also,

the initial investment and maintenance cost of industrial textile machines used for weaving and stitching is not an issue in this technique, which leads to significant financial savings.

Saz-Orozco et al. [59] investigated the effects of polyamide (PA) and polyethylene terephthalate (PET) veils on the interlaminar fracture toughness (IFT) of a glass fiber/ vinyl ester (GF/VE) composite. They showed that PET veils had no significant effect on the IFT of composites while PA veils increased the mode I interlaminar fracture toughness values at crack initiation and propagation levels improved by 59 and 90%, respectively. Fitzmaurice et al. [60] also showed that PET veils were not effective for improving Mode-I interlaminar fracture toughness of the glass fiber/ polyester resin (GF/PE) composites due to the weaker glass/resin interface providing an alternative crack propagation path. They also showed that the incorporation of PET veils had positive effects on the flexural strength, interlaminar shear strength and damping properties of the composites. O'Donovan et al. [61] showed that the maximum G_{IC} for crack propagation of a PA interleaved composite increased by almost 170% over the baseline GF/PE composite. The main toughening mechanism was fiber bridging observed during the crack propagation (Figure 2.3.9). Due to good adhesion between epoxy matrix and thermoplastic veil, the veil acts as a strain energy absorber and the veil fibers are bridging the crack opening. Miller et al. [62] observed a 40% increase in G_{IC} with the addition of polyurethane (PU) veil.

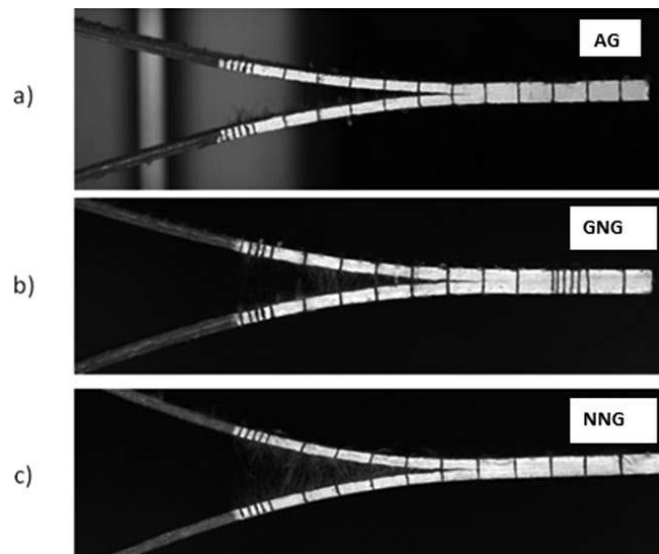


Figure 2.3.9. Fiber bridging under Mode-I loading [61].

Other types of nonwoven veils such as aramid and carbon were also studied by the researchers. Ni et al. [63] investigated the effects of aramid nonwoven veils on the mechanical properties of CF/bismaleimide (BMI) composite. The results showed that the loss factor could be improved 108%. Mode I interlaminar fracture toughness (G_{IC}), Mode II interlaminar fracture toughness (G_{IIC}) and interlaminar shear strength of CF/BMI composites were also improved 38.6%, 15.5% and 10.2%, respectively with the incorporation of aramid nonwoven veils. Lee et al. [64] investigated the effects of carbon nonwoven veils on the Mode-I fracture toughness under different temperatures. They concluded that the Mode-I fracture toughness was not significantly affected with the incorporation of carbon nonwovens under room temperature.

Although some studies exist in the literature on the effects PA66 veils on Mode-I fracture toughness of composites, further research is needed to clarify the effects of PA66 veils on the other mechanical properties of existing CF/EP composites. There is no report in the literature investigating the effects of PA66 nonwoven interleaving on the mechanical properties of the carbon fiber/epoxy composites manufactured by vacuum-infusion technique. Additionally, the effects of aramid nonwoven veils on the in-plane mechanical properties of CF/EP composites are still unrevealed. This thesis aims to make a unique contribution on this research gap and develop a better understanding of the effects of aramid and PA 66 nonwovens on the mechanical performance of the composites.

2.4. Toughening of polymeric composite materials with nanofibrous mats

To overcome the disadvantages of mechanical and material approaches described in the previous sections, a novel approach (both mechanical and material) was proposed by Dzenis and Reneker [6]. They used electrospun polymeric nanofibers as a second reinforcement in between the primary reinforcing fabrics prior to infusion (Figure 2.4.1). This cost-effective approach only requires an extra-step to manufacturing

flow, and there is no need for a radical change in the processing route. Although the idea is not new, there has been increasing attention devoted to this topic in recent years.

Various types of polymeric nanofibers have already been studied. Some researchers investigated the effects of thermoplastic nanofibers dissolved in the matrix resin and they reported significant improvements in interlaminar fracture toughness values due to particulate phases exist in the final laminate.

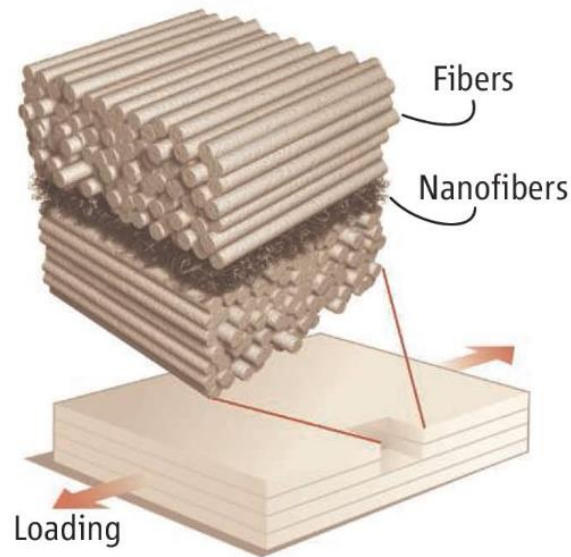


Figure 2.4.1. Laminated composite with nanofiber-reinforced interfacial layer [6].

Before literature review of recent studies on electrospun nanofiber toughened composites, a brief introduction to electrospinning process is given in the following subsection since this process plays a crucial role in this study.

2.4.1. Electrospinning

Electrospinning is a unique technology not only for its low cost set-up and simple operation but also it can be effectively up-scaled, opening actual perspectives for industrial production [65].

A typical electrospinning system (Figure 2.4.2) consists of a syringe pump, a high voltage source and a collector (usually a metal screen, plate or rotating mandrel). A charged polymer solution is fed through a small opening or nozzle. Because of its

charge, the solution is drawn to a collector, typically 5 – 30 cm away, as a jet. During the jet's travel, the solvent evaporates quickly and the fibers solidify on the collector. End product is a non-woven fiber mat that is composed of tiny fibers (50 nm-10 μ m) in different morphologies [66].

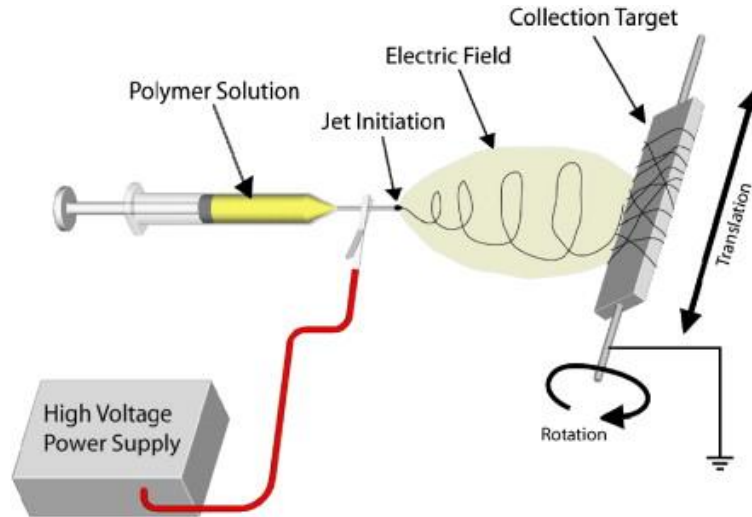


Figure 2.4.2. Schematic representation of an electrospinning device [67].

The morphology and diameter of electrospun fibers depends on (i) solution parameters such as concentration, molecular weight, viscosity, surface tension, solvent type and conductivity and (ii) working parameters such as applied voltage, working distance and feeding rate [68].

As the concentration is very low, polymeric particles will be obtained. As the concentration is little higher, bead-formation is observed. If the concentration is very high, helix-shaped micro-ribbons will be obtained. Within the electrospinning process, applied voltage is the key factor among the others. The effect of applied voltage on the nanofiber diameter can be different according to type of polymer. In some cases, the higher voltage leads to large nanofibers [69]. For instance, polyethylene oxide (PEO) nanofiber diameter increased with the increase of applied voltage. On the other hand, Yuan et al. [70] showed the increase in applied voltage decreased polysulfone (PSF) nanofiber diameter. If the working distance is too long, bead fiber can be obtained. Generally, lower flow rate is more suitable to provide enough time for polarization. If the flow rate is too high, thick nanofibers with bead formation will be obtained instead

of smooth and thin nanofibers. Therefore, these parameters should be optimized to obtain uniform bead-free thin nanofibers.

2.4.2. Literature review on electrospun nanofiber toughened composites

In 2008, Li et al. [71] toughened carbon/fiber epoxy composite by using electrospun polysulfone (PSF) nanofibers. The authors also used PSF films in the interlaminar region and compared the test results with the PSF nanofiber modified and reference specimens. Figure 2.4.3 shows manufacturing steps of electrospun PSF nanofiber toughened CF/EP composite.

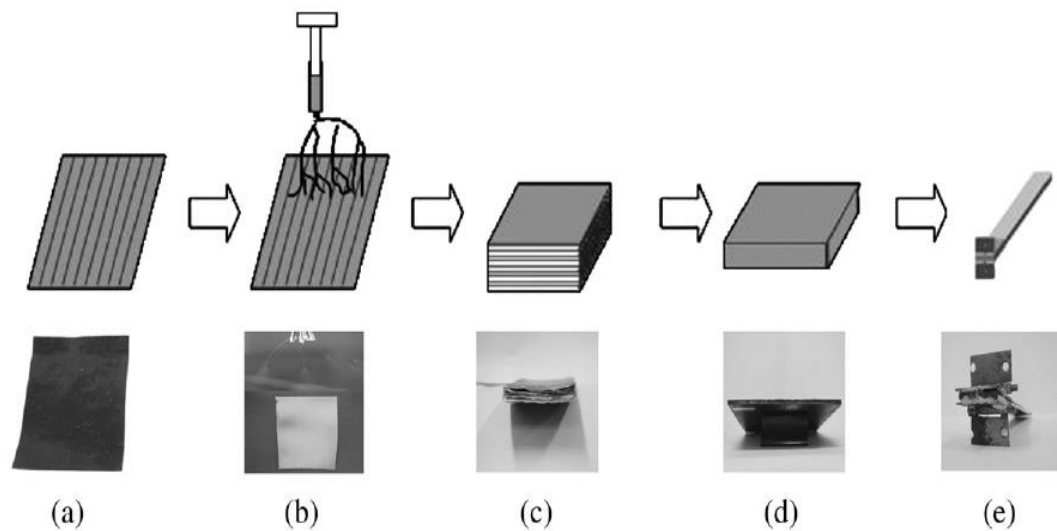


Figure 2.4.3. Fabrication steps of PSF nanofibers toughened CF/EP composite [71].

Electrospun PSF nanofibers with an average diameter of 230 nm were produced and directly deposited onto carbon fiber prepreps. The carbon prepreps were hot-pressed into composite and left to cure. During the curing process, the morphology PSF nanofibers were changed to nano-scaled PSF spheres and dispersed uniformly between the composite plies (Figure 2.4.4). It was shown that the Mode I fracture toughness test results of PSF nanofibers toughened composite was 140% and 280% higher than those of PSF films toughened and reference composite respectively. The main reason for this increase was the uniform distribution of polysulfone spheres.

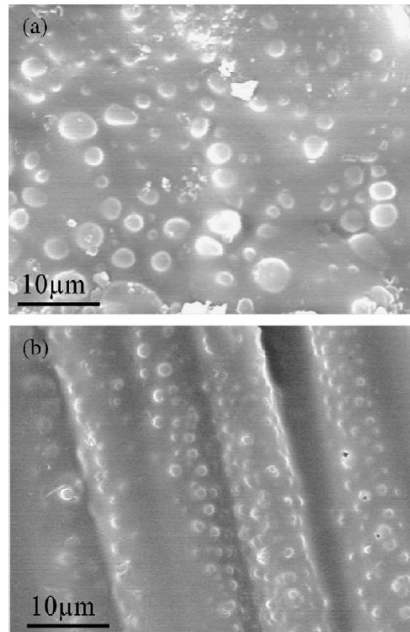
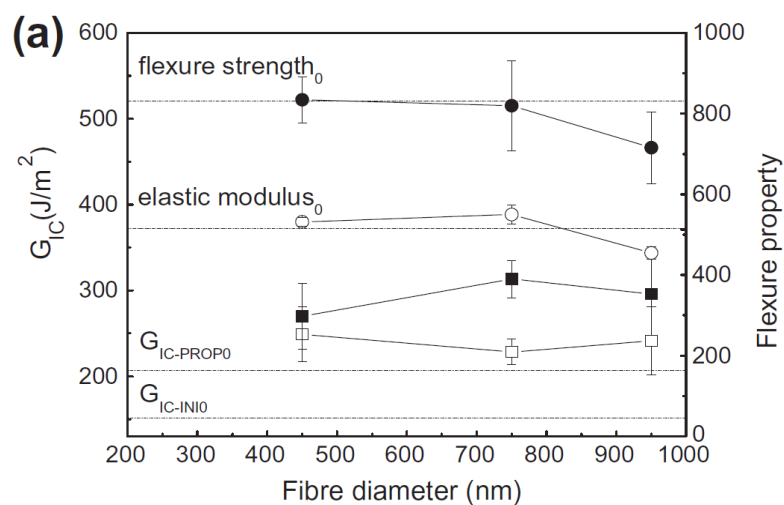


Figure 2.4.4. (a) PSF nanofibers and (b) PSF films toughened composite specimens [71].

Zhang et al. [72] used polyetherketone cardo (PEK-C) nanofibers as interleaf material to improve delamination resistance of CF/EP composite. PEK-C nanofibers were directly electrospun to one side of the dry carbon fabric. The effects of nanofiber diameter and nanolayer thickness on the fracture toughness, flexural properties and thermal mechanical properties were investigated (Figure 2.4.5). The authors showed that the flexural strength and modulus decreases with the increase of nanofiber diameter and thickness. The Mode-I strain energy release rates for crack initiation (G_{IC} -ini) and for crack propagation (G_{IC} -prop) were also influenced by the nanofiber diameter as shown in Figure 2.24.



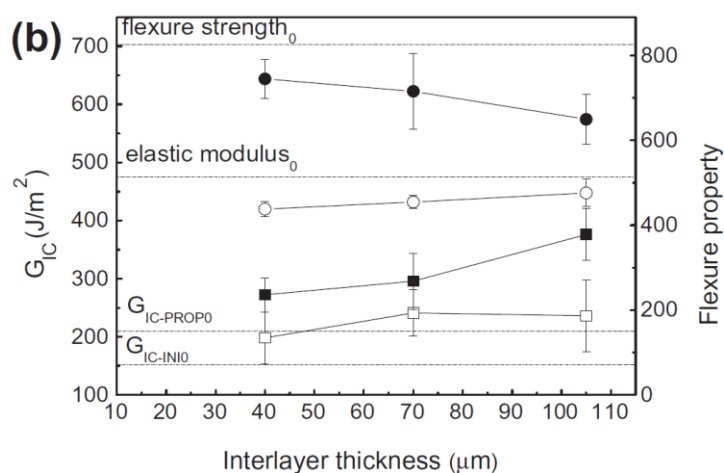


Figure 2.4.5. Mode I delamination fracture toughness and flexure properties as a function of (a) nanofiber diameter and (b) interlayer thickness [72].

The average G_{IC-ini} for the control specimen was 151 J/m^2 . The G_{IC-ini} value of the nanofiber-modified specimens with 450 nm, 750 nm and 950 nm average nanofiber diameter was determined as 249 J/m^2 , 228 J/m^2 and 241 J/m^2 respectively. The nanofiber diameter had no significant effect on $G_{IC, ini}$ values. The thicker nanofiber interlayer led to higher average $G_{IC-prop}$. The weight increase in the composite due to the nanofibers was negligible around 0.4%. They concluded that the composites with smaller nanofibers showed better performance without compromising the in-plane properties of the toughened composites. The PEK-C nanofibers retained the glass transition temperature of the cured resin. Figure 2.4.6 shows the fracture surfaces of DCB test specimens. In this figure, the dark spots show the PEK-C rich particulate phases removed by the DMF solvent before SEM observations. The size of PEK-C rich zones and their distance increased with the increase in the fiber diameter.

Same research group [73] used polycaprolactone (PCL), polyvinylidene fluoride (PVDF) and polyacrylonitrile (PAN) nanofiber interlayers to toughen CF/EP composite laminates. Figure 2.4.7 shows the SEM images of electrospun nanofibers. Bead-formation was observed in PCL nanofibers whereas PVDF and PAN nanofibers were bead-free. The average PCL nanofiber diameter was determined as 103 nm, 125 nm and 210 nm spun from 12 wt. %, 15 wt. % and 20 wt. % solutions, respectively. The average fiber diameter of PVDF and PAN nanofibers were determined as 542 and 607 nm respectively.

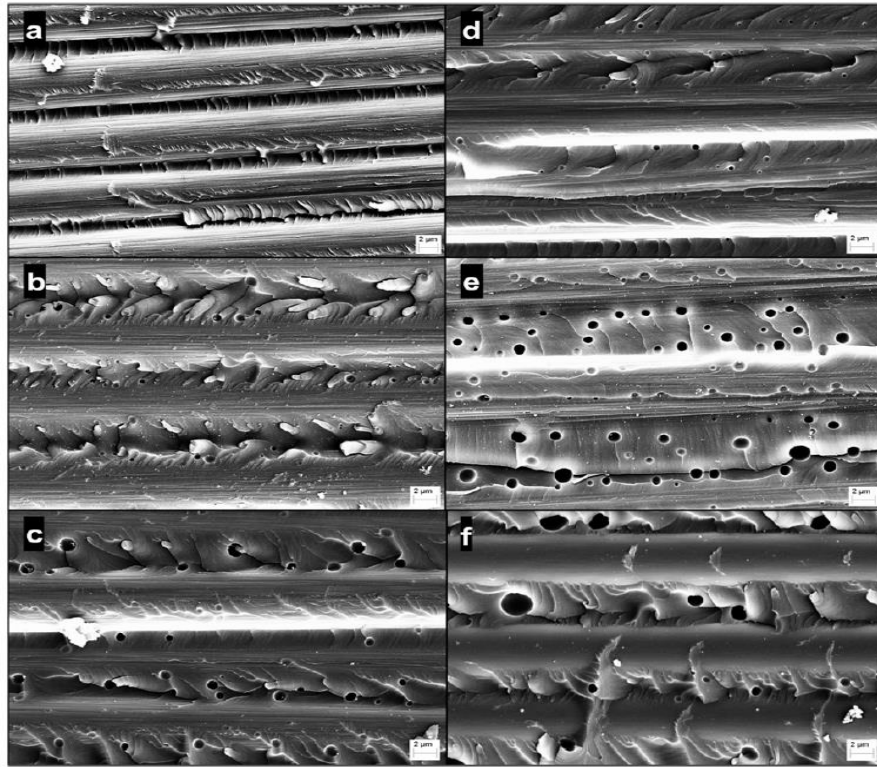


Figure 2.4.6. SEM images of fractured DCB test specimens (a) control specimen, (b) nanofiber diameter: 450 nm, (c-d) nanofiber diameter: 750 nm, (e-f) nanofiber diameter: 950 nm [72].

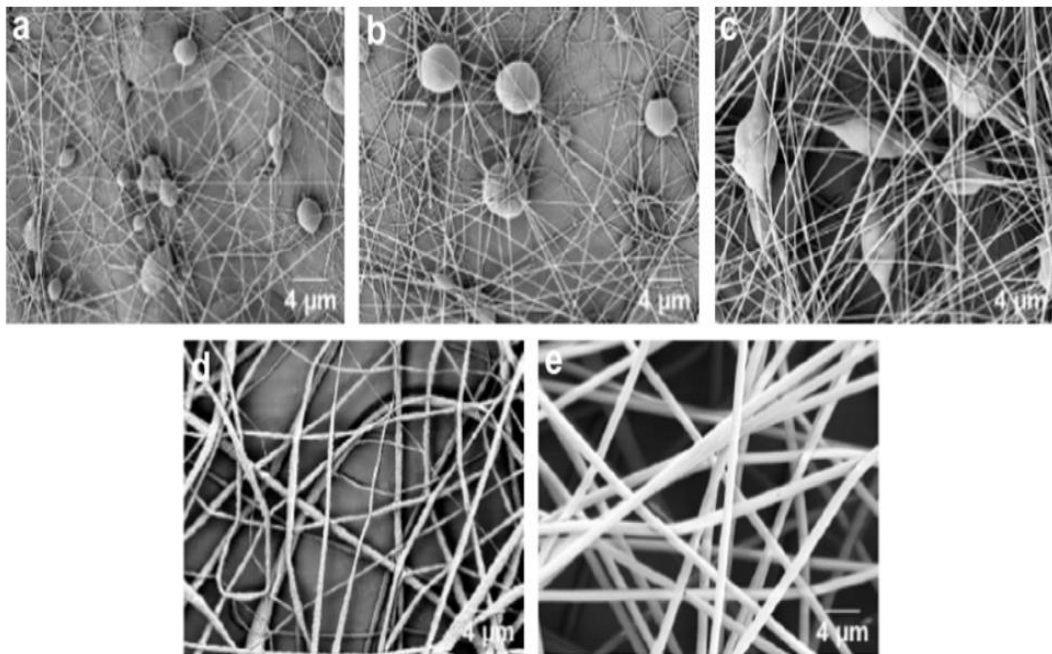


Figure 2.4.7. SEM images of electrospun nanofibers; PCL nanofibers; (a) 12 wt.%, (b) 15 wt.% and (c) 20 wt.% solutions (d) PVDF nanofibers and (e) PAN nanofibers [73].

The authors manufactured reference and nano-modified composite laminates with a stacking sequence of $[0/90]_4$ by hand lay-up technique. The nanofiber weight fraction was approximately 0.2%. Figure 2.4.8 shows the Mode I interlaminar fracture toughness of the reference and nano-modified composites. As can be seen in the figure, composites interleaved by PCL nanofibers showed higher fracture toughness than the reference specimen. The PCL nanofiber modified composites improved G_{IC-ini} values about 55% for 103 nm, 92% for 125 nm and 87% for 210 nm. No significant change in $G_{IC-prop}$ was observed due to PCL nanofibers. On the other hand, no toughening effect was observed for PVDF and PAN nanofibers.

Figure 2.4.9 shows the delaminated fracture surfaces of DCB specimens. For PCL nanomodified specimens, inhomogeneous phase separation occurred as can be seen in Figure 2.4.9b-f. The PCL-rich particulate microphases resisted crack growth and stress concentrations around these particles led to form plastic zones. The result was more energy absorption. For the PVDF and PAN modified composites, the polymerization-induced phase separation was not occurred, Figure 2.4.9e-f, therefore toughening effect was not observed. The authors stated that the polymerization-induced phase separation was one of the toughening mechanisms for the interlayer toughening by thermoplastic nanofibers.

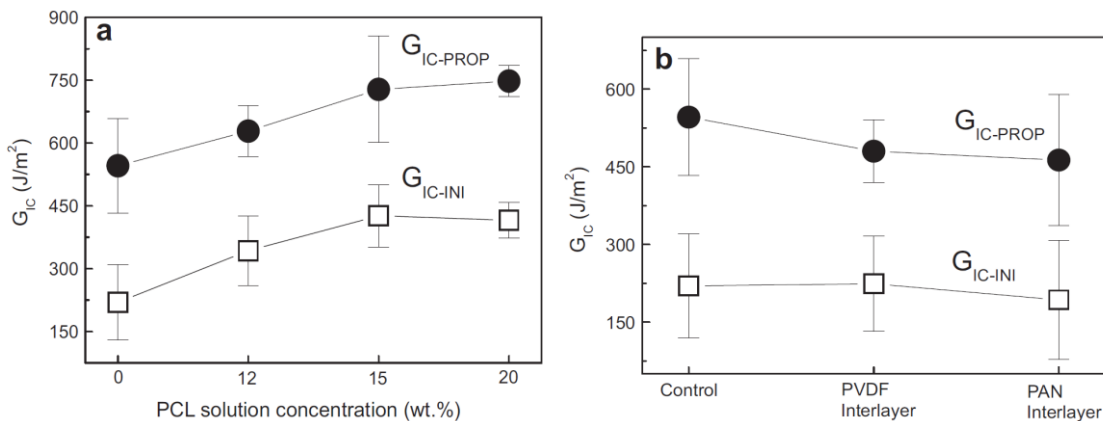


Figure 2.4.8. Mode I fracture toughness (a) PCL and (b) PVDF, PAN interlayers [73].

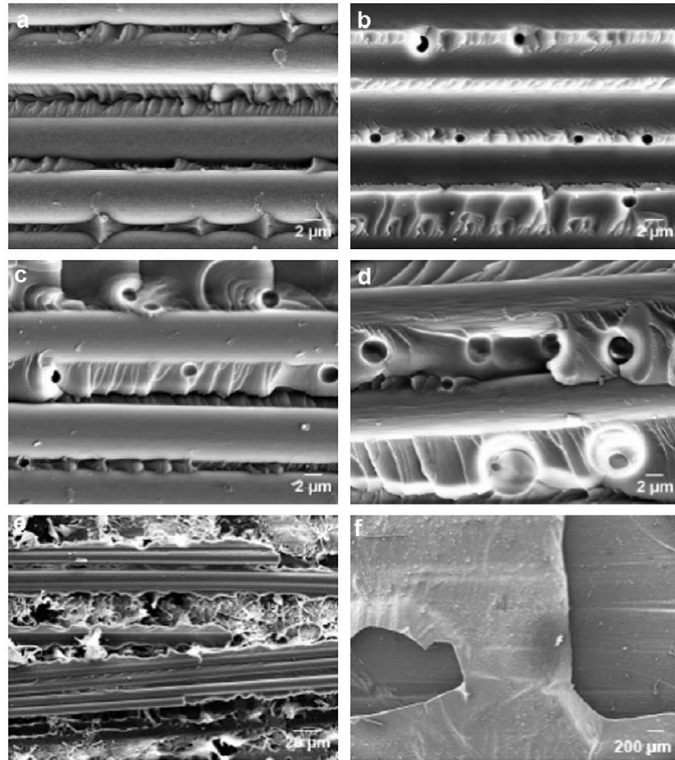


Figure 2.4.9. Fractured surfaces of carbon carbon/epoxy composites after DCB test (a) is the control specimen, (b-f) PCL modified and (e-f) PVDF and PAN modified specimens [73].

Several types of polymers which retain their nanofiber structure in the final laminate were studied by other researchers. van der Heijden et al. [74] aimed to increase the interlaminar fracture toughness of infusion molded laminates by using electrospun PCL nanofibers without compromising other mechanical properties. The authors introduced PCL nanofibers into laminates in three different configurations; (i) a single layer of nanofibers was directly electrospun on one side of the glass-fibre mats (SLD), (ii) a single layer of nanofibers was deposited on each side of the glass fiber mats (DLD) and (iii) standalone nanofiber nonwovens placed in between the glass-fiber mats. The glass fibre mats were stacked into a steel mold in both $[0]_8$ and $[0/90]_{2s}$ configurations and the composite laminates were manufactured by vacuum-assisted resin transfer molding (VaRTM). The authors performed Mode I fracture toughness (DCB), tensile and open hole strength tests on the composites. They obtained significant improvement almost 100 % in the initiation Mode-I fracture toughness values in the DLD specimens. The improved interlaminar fracture of DLD configuration was also observable in the open hole strength tests. Figure 2.4.10 shows the photograph of reference and PCL-modified open hole test specimens. Delamination zones became

smaller than the reference specimens around the hole after the incorporation of PCL nanofibers. The tensile, shear and dynamic mechanical properties were not significantly influenced by the PCL nanofibers.

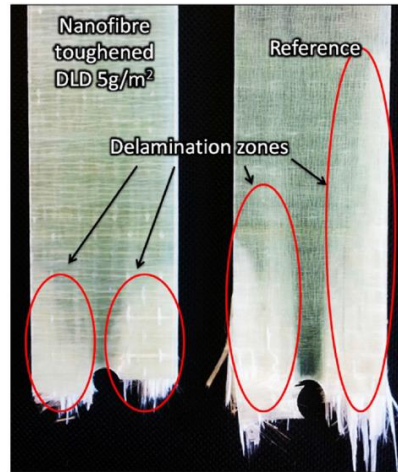


Figure 2.4.10. Photograph of open hole test specimen after failure [74].

Herwan et al. [75] proved that load-bearing capacity of pin joined composite laminates can be improved by introducing PAN nanofibers between dry carbon fabrics. Bilge et al. [76] were deposited epoxy compatible P(St-co-GMA) copolymer based electrospun nanofibers onto unidirectional and 0/90 twill weave carbon/fiber epoxy prepreg systems. The authors performed uniaxial tensile tests on the laminates with a stacking sequence of $[0]_6$ and $[0/90]_{6\text{woven}}$ laminates. For the specimens without holes, the nanofibers were collected on the whole surface of each ply. For open hole test specimens, local toughening were done by collecting nanofibers on the prepreg layers around the holes (Figure 2.4.11). The results showed that the tensile strength and open-hole failure stress were increased by 18% and 9%, respectively.

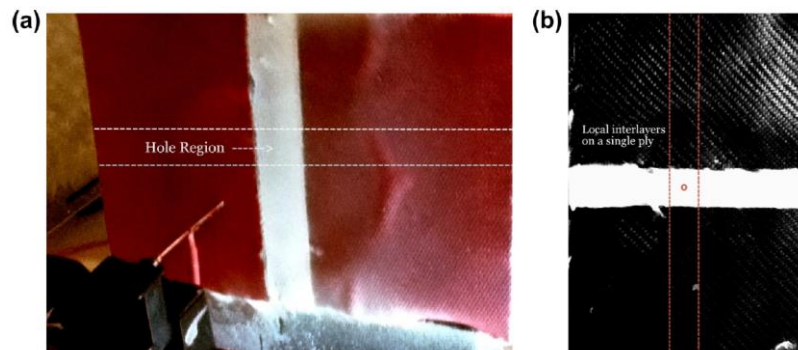


Figure 2.4.11. Photograph of local application of nanofibers around the hole [76].

Liu et al. [77] investigated the effects of CNTs-polyurethane (PU) nanowebs on the tensile and flexural properties of the CF/EP prepreg laminates. They manufactured three types of specimens; (i) reference specimens with no CNTs nanowebs, (ii) the specimens having CTNs/PU nanoweb interlayers with 1 wt. % MWCNT concentration and (iii) specimens containing CTNs/PU nanoweb interlayers with 5 wt. % MWCNT concentration. The results showed that the in-plane tensile strength and modulus of the interleaved laminates could be improved by 8.4% and 4.7% respectively. Improvement of 15.6% and 2.7% in flexural strength and modulus were obtained for the interleaved laminates. The authors also showed that the presence of CNTs could cause a reduction of tensile strength due to the local agglomerations in the inner parts of nanofibers.

Polyamide (PA) nanofibers have attracted researchers' attention in recent years. PA, a biodegradable and biocompatible synthetic polymer, has a superior fiber forming ability with good mechanical properties. PA 66 has high melting temperature (262 °C) which allows the nanofibers to maintain their morphology during the curing process of the laminate. Unlike other polymers, such as polyethylene oxide and polyvinyl alcohol, PA is resistant to both water and humidity. PA can be dissolved in the solutions of formic or formic/acetic acids; this ensures environment-friendly processes in comparison with other toxic solvents such as dimethylformamide (DMF) [78].

Sanatgar et al. [79] investigated the effects of two different solvent types and three solution concentrations on the electrospinning of polyamide 66 (PA 66) nanofiber yarns. Nanofiber yarns were electrospun from PA66 solutions in formic acid and formic acid/chloroform (3/1 v:v). SEM and X-ray diffraction (XRD) were used to characterize the morphology and properties of the nanofibrous yarns. Experimental results showed that the addition of chloroform to formic acid increases viscosity of polymer solution and the nanofibers diameter significantly. XRD patterns reveal that the presence of chloroform affects the crystallinity and the mechanical properties of the produced nanofibrous yarns. Compared to other solution concentrations, PA66 nanofiber yarn from 10 wt % formic acid/chloroform (3/1 v:v) solution was successfully electrospun with the highest strength and modulus.

Saghafi et al. [80] studied PA 66 nanofibers as interleaf material due to its chemical compatibility with the epoxy matrix and mechanical properties. 14 wt. % PA

66 electrospinning solutions were prepared using acid/chloroform (50:50 v/v) solvent system. The electrospinning duration was about 60 minutes and final mat thickness was $25 \pm 8 \mu\text{m}$. The average PA66 nanofiber diameter was $150 \pm 15 \text{ nm}$. The authors investigated the influence of electrospun PA 66 nanofibrous layers on the both Mode-I and Mode-II fracture toughness of CF/EP prepreg composites. Force-displacement curves of the specimens under Mode-I and Mode-II loading were shown in Figure 2.4.12 and Figure 2.4.13 respectively.

It can be seen from Figure 2.4.12 that the modified laminates sustained higher loads about 40% as compared to reference specimens during the tests. The mode-I fracture toughness of the nanomodified specimens were increased about 62% with respect to reference specimens. The ENF results (Figure 2.4.13) showed that the maximum stress was increased about 41% by incorporating of PA66 nanofibers in the interlaminar region. The presence of nanofibrous mat significantly increased the absorbable mechanical energy.

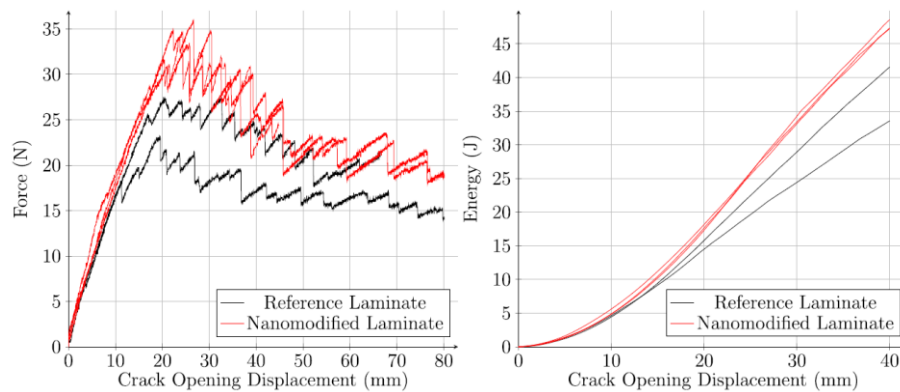


Figure 2.4.12. Double Cantilever Beam (DCB) fracture tests curves: left) Force vs. COD; right) Mechanical energy vs. COD [80].

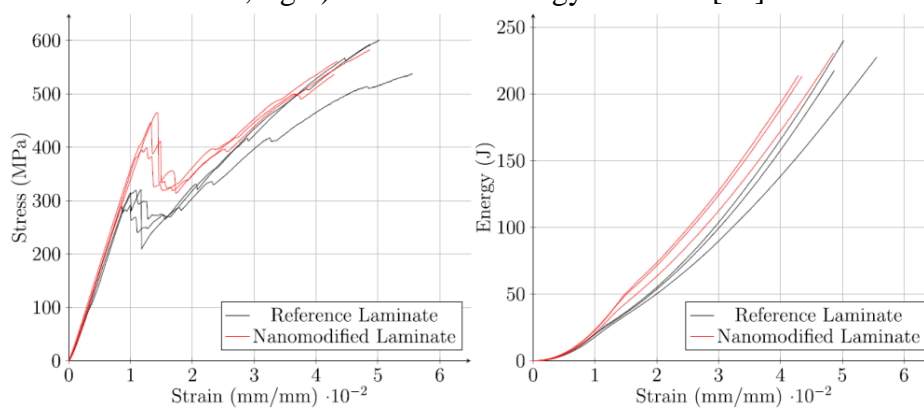


Figure 2.4.13. End Notched Flexure (ENF) fracture tests curves: left) Stress vs. Strain; right) Mechanical energy vs. Strain [80].

Saghafi et al. [80] also showed that the effect of PA 66 nanointerleafs was more effective for improving Mode II fracture toughness than Mode I fracture toughness IFT. The authors showed that the improvement in G_{IIC} was 2 times higher than the improvement in G_{IC} . SEM micrographs showed that nanofiber bridging mechanism improved the fracture toughness of modified specimens and kept the plies together when the matrix cracks occurred. The fracture surface of nanomodified specimens (Figures 2.4.14b and 2.4.14d) was more complex and irregular than the fracture surface of non-modified ones (Figures 2.4.14a and 2.4.14c) which smooth and featureless. In Figure 2.33b, the nanofibers pulling out from the epoxy in the composite interface can be seen. During the crack propagation, the PA 66 nanofibers keep the plies together and hinder the crack propagation. Due to the higher ductility of the PA66 nanofibers, these nanofibers act like bridging elements in the interlaminar region and gives significant amount of resistance to the interface even if the matrix epoxy fails due to excessive strain.

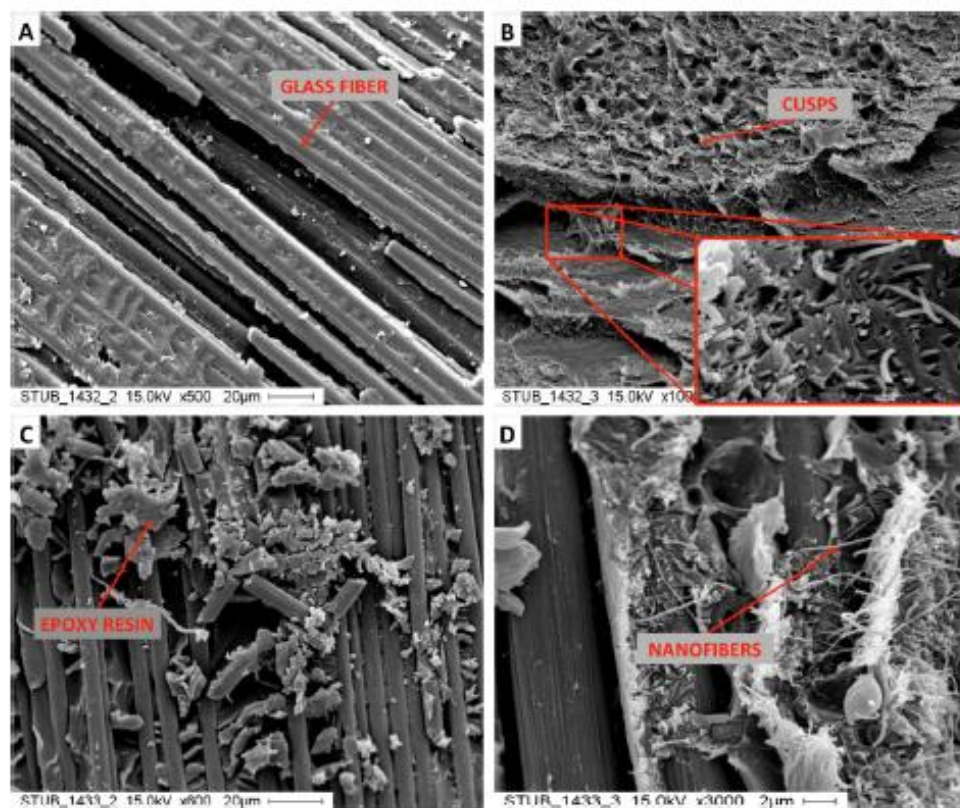


Figure 2.4.14. SEM micrographs of DCB and ENF fractured surfaces (A-B) DCB and (C-D) ENF tests, Virgin (A-C) and Nanomodified (B-D) interfaces [80].

Palazzetti et al. [81] investigated the effects of electrospun PA 66 nanofibrous mat on the Mode I (DCB) and the Mode II (ENF) fracture toughness of composite laminates. Figure 2.4.15 and Figure 2.4.16 show DCB and ENF fracture load-displacement curves; respectively. As seen in Figure 2.4.15, the maximum load of nanomodified specimens was lower about 12% than that of the reference specimens. On the contrary, the incorporation of the nanoveils improved the absorbable mechanical during the crack propagation. The increase in the absorbed energy was 23% as compared to reference specimens. The improvement in critical strain energy release rate (G_{IC}) was 5% higher than that of the reference specimens. It can be concluded that Mode-I fracture toughness was not significantly due to the PA66 nanofibers.

As seen in Figure 2.4.16, the PA66 nanomodified specimen has a maximum stress value 6% higher than the maximum value of the reference specimen. It could be noted that the nanomodified specimens reached the maximum stress at higher strain values as compared to reference specimens. Therefore it can be said that the nanofibers increased the stress level where the first material failure occurred. Moreover, the stress values of the nanofiber modified specimens were higher than that of the reference specimens during the crack propagation.

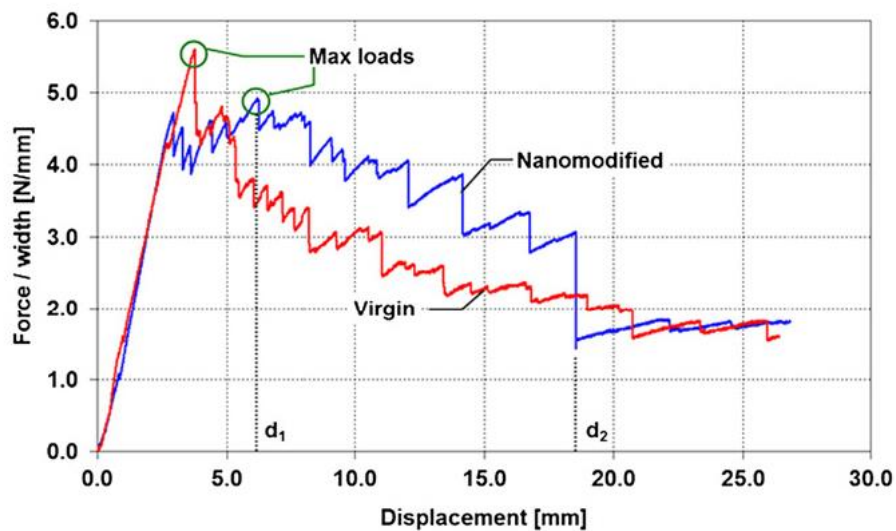


Figure 2.4.15. Double Cantilever Beam (DCB) fracture tests curves [81]

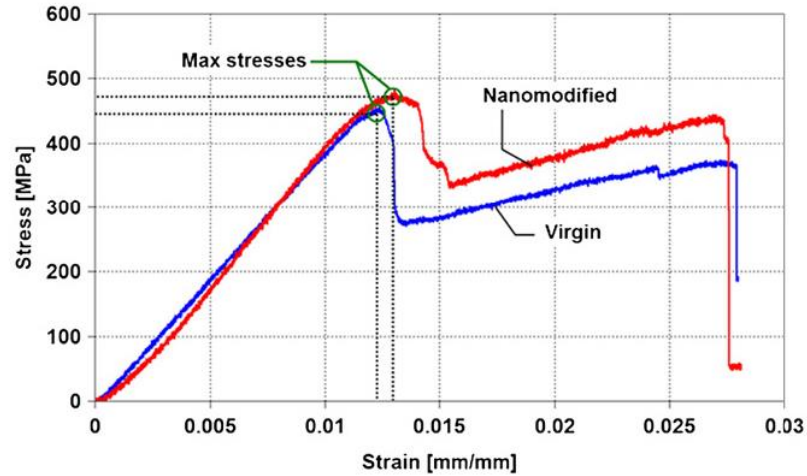


Figure 2.4.16. End Notched Flexure (ENF) fracture tests curves [81]

Daelemans et al. [82] studied PA 6/6 and PA 6/9 nanofibers to improve fracture toughness of carbon fiber/epoxy composites. PA 6/6 and PA 6/9 nanofibers caused an increase in Mode-I fracture toughness about 28% and 42%; respectively. The main mechanism was the bridging of micro-cracks by PA nanofibers. The nanofiber interleaved showed better performance under Mode-II loading as compared with the reference specimens under Mode-I loading. This was due to the optimal loading condition in which the shear stresses were more dominated between the plies in the interlaminar region.

Another study by Daelemans et al. [83] investigated the effects of PA 69 nanofiber orientation on the Mode-II fracture toughness of unidirectional CF/EP laminates with a stacking sequence of $[0]_{12}$. A formic acid (FA)/acetic acid (AA) (1:1) solvent was used to prepare 20 wt% PA 69 electrospinning solutions. Randomly oriented nanofibers were obtained by rotating the collector at a low speed of 150 rpm (Figure 2.4.17a). In order to obtain aligned PA 69 nanofibers, the rotational speed of the drum collector was changed to 4000 rpm (Figure 2.4.17b). The average diameter of the randomly oriented and aligned nanofibers were 457 ± 53 nm and 464 ± 110 nm respectively. The nanofibrous areal weight was 11 ± 0.5 g/m².

In their study, two distinct failure regions were observed in the interleaved laminates; intralaminar failure (Type A) and interlaminar crossings (Type B) as shown in Figure 2.4.18. The main toughening mechanism is the formation of nanofiber bridging zones in Type A failure regions. This failure mechanism occurred when the PA

69 nanofibers were oriented parallel to the crack growth direction. On the other hand, when the aligned nanofibers oriented transversely to the crack growth direction, the nanofiber bridging zones developed mainly at the interlaminar crossings in Type B failure regions. The toughening effect was more significant if the nanofibers were oriented transversely to the crack growth direction. High amount of nanofibers were able to bridge cracks in this case.

CF/EP composite laminates interleaved with a random deposition of nanofibers resulted in the highest increase in Mode II IFT. Due to their random orientation, nanofiber bridging mechanism was seen in both Type A and Type B failure regions. The Mode II initiation interlaminar fracture toughness value was increased about two times after the incorporation of randomly oriented PA69 nanofibers as compared to reference specimens. The success of randomly oriented nanofibers is an advantage for composite industry because randomly oriented nanofibers can be easily produced using electrospinning process and a dedicated collector rotating at very high speed is not necessary to obtain these nanofibers.

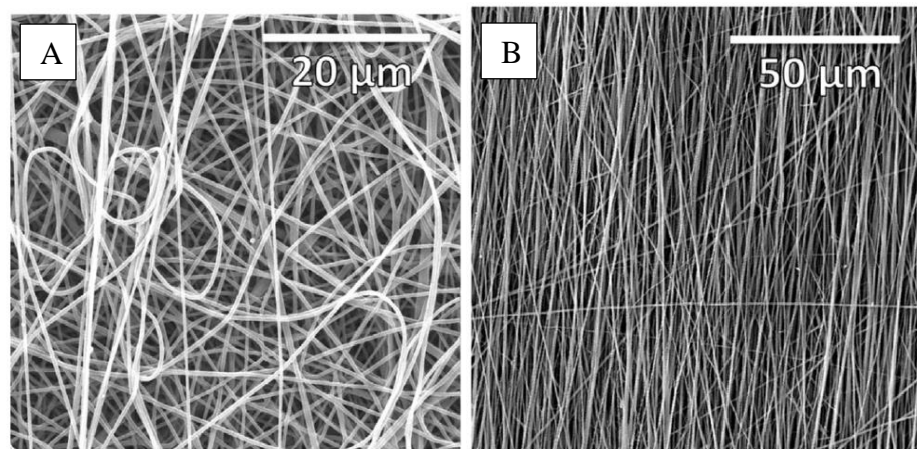


Figure 2.4.17. (a) Randomly oriented and (b) aligned PA 6.9 nanofibres [83]

The result of this literature review showed that there is a lack of research on the topic of electrospun nanofiber toughened composites. Although, most of the studies were made to reveal the effects of electrospun nanofibers on the Mode-I and Mode-II fracture toughness of the CF/EP composites, there is a lack of research on the effects of these nanofibers on the other mechanical properties of these composites. Also, it was observed that prepreg materials were used in the most of the studies available in the

literature. However, there are few studies on the effects of electrospun nanofibers on the CF/EP composites manufactured by VaRTM technique.

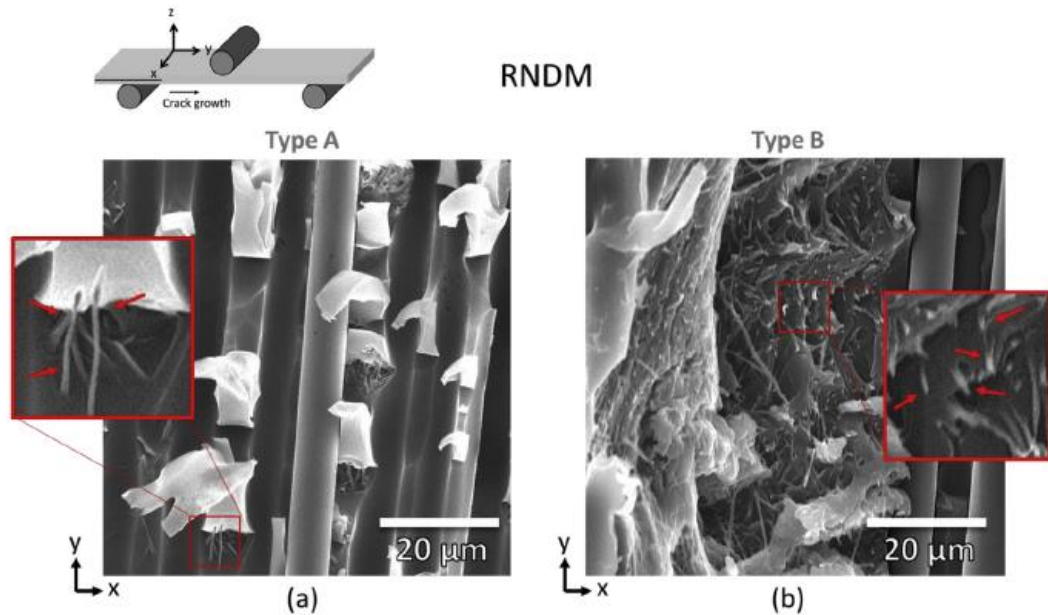


Figure 2.4.18. Nanofiber bridging and necked nanofibers at interlaminar crossings [83].

Additionally, the transition of the nanofiber-interleaving technique into commercial products has already started, and now the first commercial supplies of thermoplastic nanoveils are on the market. For wider acceptance of this technique in composite industry, much more research must be done. The effects of these nanoveils on the other in-plane mechanical properties are still unknown. This thesis aims to make a unique contribution to the literature and provide better understanding of the behavior of CF/EP composites modified by PA66 electrospun nanofibers.

CHAPTER 3

EXPERIMENTAL

3.1. Materials

In this thesis, unidirectional carbon fabrics were used as primary reinforcement material. Unidirectional carbon fabrics with a unit weight of 350 g/m^2 were supplied from Kordsa Global Inc., Turkey. The epoxy resin (Momentive L160, Hexion Inc., Columbus, Ohio) and its hardener (Momentive H160, Hexion Inc., Columbus, Ohio) were used as matrix material with the weight ratio of 80:20, respectively.

Different types of micro and nano-scaled nonwoven veils were used as secondary reinforcement (interleaf materials). Commercial aramid veils with an areal density of 8.5 g/m^2 were supplied from ACP Composites Inc., USA. The average fiber diameter was determined as $15.36 \pm 3.67 \text{ }\mu\text{m}$ by measuring at least 25 fibers per sample using ImageJ software (National Institute of Mental Health, Bethesda, MD, USA). Some physical and technical properties of the aramid veils were listed in Table 3.1. SEM images of the aramid veils are shown in Figure 3.1.1. Commercial micro PA 66 nonwoven veils (N-FusionTM) at two different areal densities 17 and 50 gsm were provided by Cerex Advanced Fabrics Inc., USA. SEM images of the PA 66 veils are shown in Figure 3.1.2. The thickness of PA66 17 and 50 gsm veils were $80 \mu\text{m}$ and $150 \mu\text{m}$, respectively.

Table 3.1. Physical and mechanical properties of the aramid veils

Fiber type	Binder	Average tensile (lb/in.) MD ¹	Average tensile (lb/in.) CD ²	Thickness (in.)	Areal weight density (g/m ²)
Kevlar29	Polyester	3.0	3.0	0.025	8.5

¹MD: machine direction, ²CD: cross direction

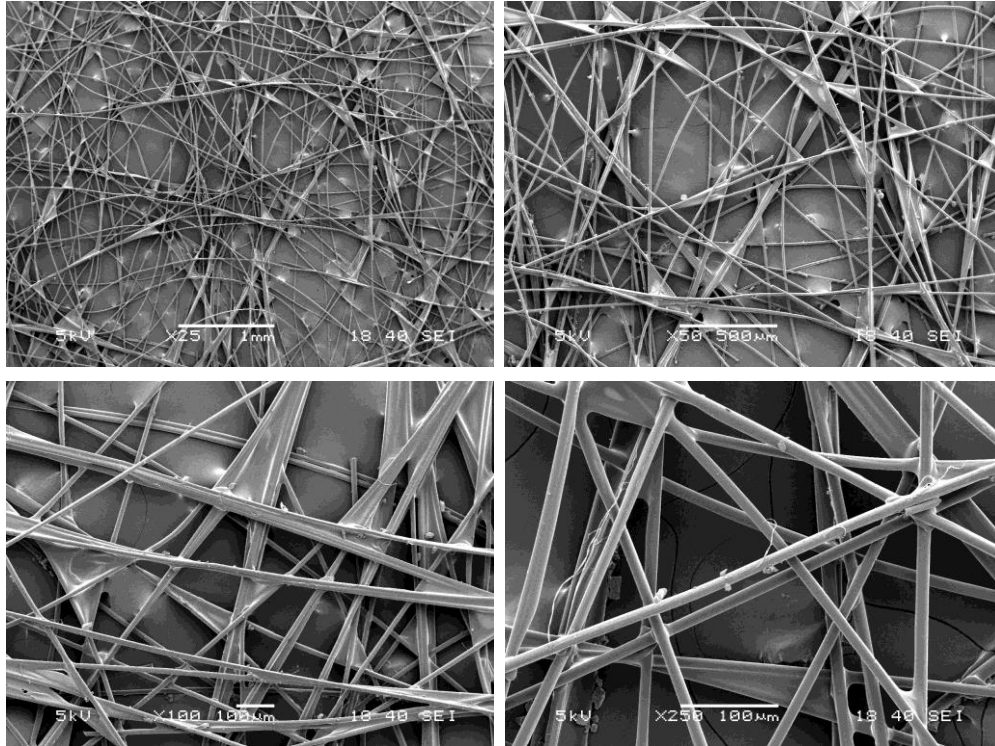


Figure 3.1.1. SEM images of aramid nonwoven veils

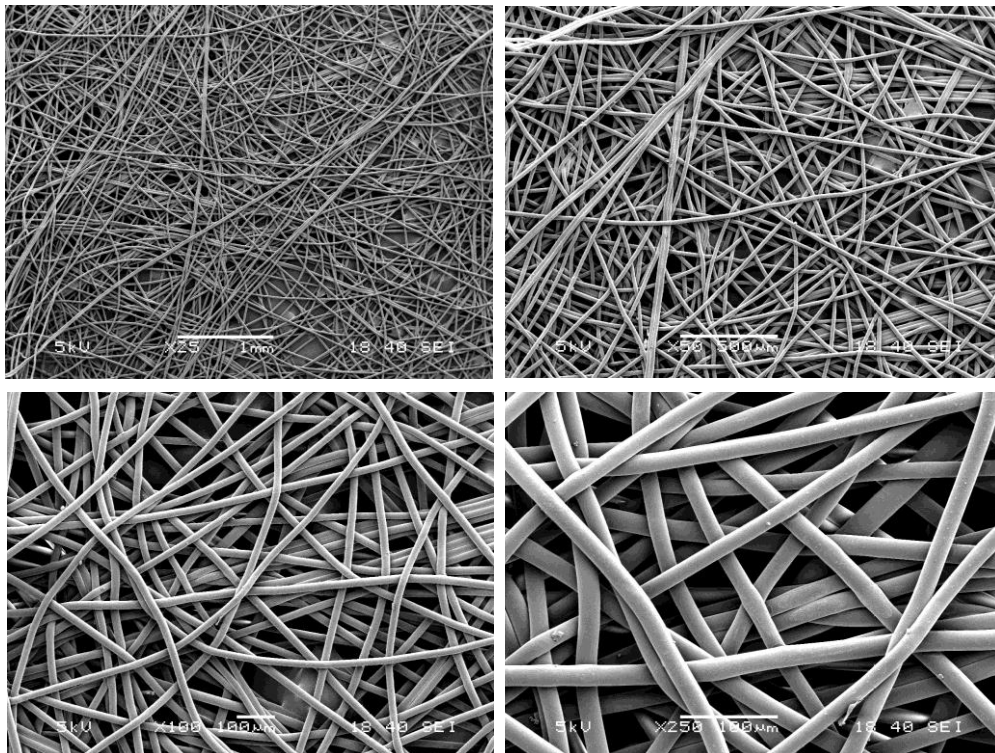


Figure 3.1.2. SEM images of PA66 nonwoven veils

Differential scanning calorimetry (DSC) was used to determine the melting point and glass transition temperature (T_g) of the PA66 veils. The samples were heated

from room temperature to 350 °C at a heating rate of 10°C/min under a nitrogen atmosphere. Figure 3.1.3 shows DSC curve of the PA66 veils. The melting and glass transition temperature of the PA66 veils were determined as 259.3°C and 67.02°C, respectively.

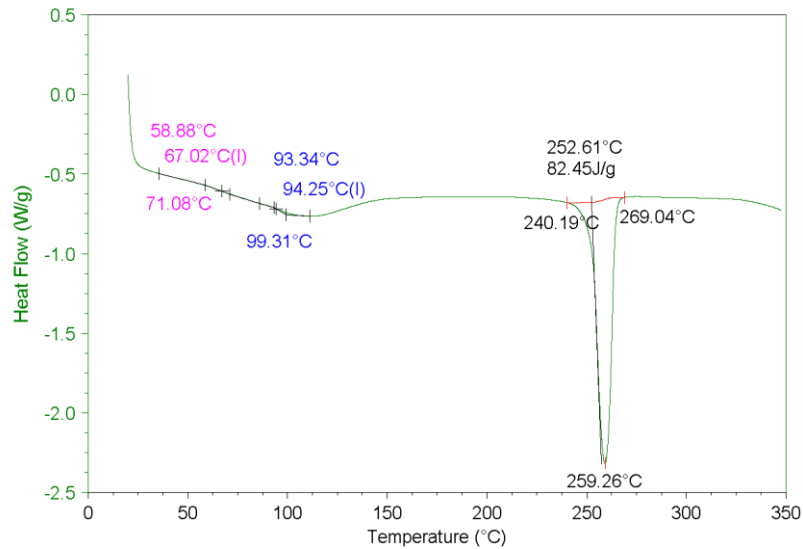


Figure 3.1.3. DSC curve of the PA66 veils.

PVA and PA66 pellets were used in their commercial form in order to produce electrospun PVA and PA66 nonwoven veils. Distilled water was used as solvent for PVA pellets whereas formic acid and chloroform were used for dissolving of PA66 pellets. The raw materials used in this study were listed below;

- PVA pellets (Oksilab Grade: BP-17)
- PA66 pellets (Sigma Aldrich- 429171)
- Formic acid (Sigma Aldrich- 27001)
- Chloroform (Sigma Aldrich- 24216)
- Distilled water

3.2. Electrospinning and deposition of electrospun nanofibers onto carbon fabrics

For electrospinning process, PVA and PA66 electrospinning solutions were prepared following the procedure given below;

- To produce PVA electrospun nanofibers, a 15 wt. % of PVA solution was prepared by dissolving 15 g of PVA powder in 100 ml distilled water at 80°C for 6 hours by using a magnetic stirrer. A transparent and homogenous gel solution was obtained then the prepared solution was left to cool down to room temperature before electrospinning.
- To prepare PA 66 electrospun nanofibers, a 10 wt % PA 66 solution was prepared by dissolving 10 g of PA 66 pellets in 100mL of formic acid/chloroform (75:25 v/v) at room temperature. This specific concentration was selected to prepare the PA 66 nanofibers with the optimum properties as suggested by Sanatgar et al [79].

The prepared PVA solution was placed into a 50-ml syringe which is attached to a syringe pump. The flow rate of the PVA solution was adjusted to 8 ml/h (1.6 ml/h for each nozzle), and the applied positive voltage was set in the range of 32–35 kV. The tip-to-collector distance was 12 cm.

The PA 66 solution was loaded into a 20-mL syringe that is attached to a syringe pump. The flow rate of the PA 66 solution was adjusted to 6 mL/h (1.0 mL/h for each nozzle), and the applied voltage and the tip-to-collector distance were kept as 30 kV and 12 cm, respectively. These working parameters were selected to produce uniform and bead-free PA 66 nanofibers based on our experience and the recommendation by Matulevicius et al. [78].

Figure 3.2.1 shows the electrospinning set-up used in this study. It consists of 5-6 nozzles that are suited for the production of relatively larger area of uniform nanofibrous nonwovens, a cylindrical translating-rotating collector and a syringe pump. The rotation speed of the collector was kept low enough to produce randomly oriented nanofibers as suggested by Daelemans et al [83]. Unidirectional carbon fabrics were

attached to the collector to produce the electrospun nanoveils directly onto the carbon fabrics. The PVA nanofibers were collected onto the unidirectional carbon fabrics for the duration of 60 minutes whereas the electrospinning duration for PA66 nanofibers were selected as 30 and 60 minutes. During the electrospinning process, the color of the carbon fabric was changed from black to white due to the nanofiber deposition. Figure 3.2.2 shows the deposition of the electrospun nanofibers onto unidirectional carbon fabrics.

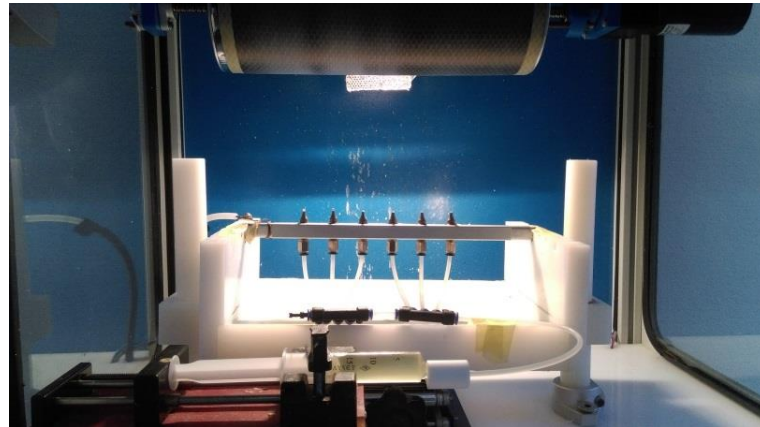


Figure 3.2.1. Electrospinning set-up in our laboratory

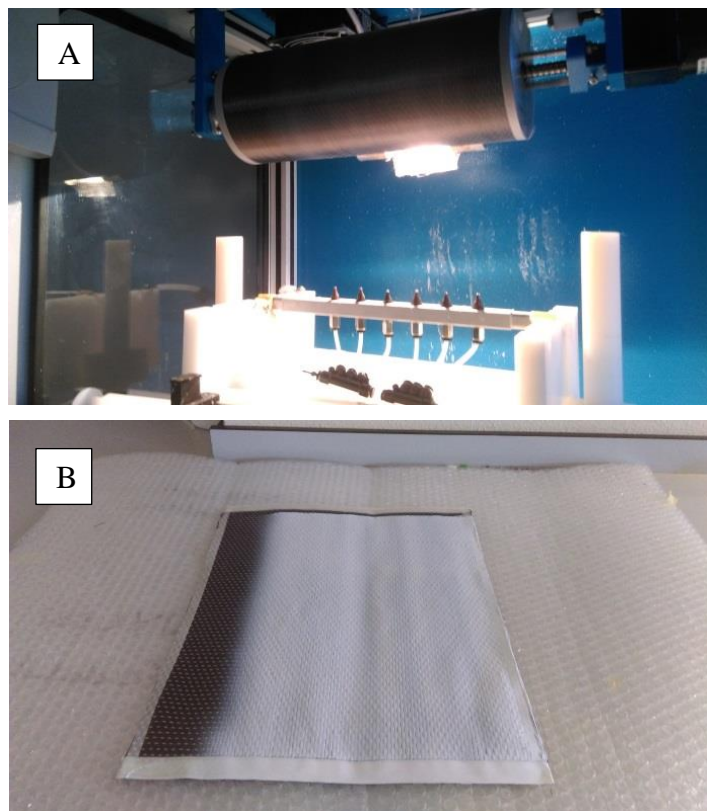


Figure 3.2.2. Deposition of electrospun nanofibers on carbon fabrics and (b) a unidirectional carbon fabric after electrospinning

Once the PVA nanofiber deposited fabrics were coated, they were heat treated (physically crosslinked) for 10 minutes at 150 °C to stabilize the PVA nanofibers and improve their mechanical strength. To remove residual solvents, the carbon fabrics with PA 66 nanofibers were kept at 60° C for 3 hours (Figure 3.2.3). Figure 3.2.4 shows the SEM image of PVA nanofibres deposited on a carbon fabric and the PVA nanofibers after heat treatment. The average PVA nanofiber diameter was measured to be 257±58 nm before heat treatment. After heat treatment, the average diameter of nanofibres was increased to 329±58 nm.

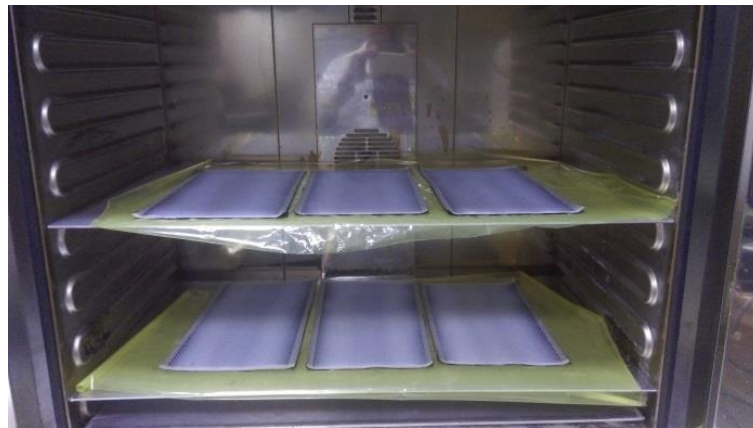


Figure 3.2.3. Heat treatment of nano modified unidirectional carbon fabrics after the electrospinning process

Figure 3.2.5 shows SEM images of PA66 electrospun nanofibers. The average PA66 nanofiber diameter was measured as 87±22 nm. It is well known that the nanofiber diameter has a significant effect on the interlaminar fracture toughness of the composites. Therefore, in this study, diameters of the nanofibers were statistically analyzed by Weibull distribution at a reliability level of 0.90. The PA 66 nanofiber diameter was determined as 110 nm with a reliability level of 0.90. Figure 3.2.6 shows the DSC curve of the PA66 nonwoven veils. The melting temperature (T_m) and T_g of the PA66 nonwoven veils were determined as 256.2°C and 48.80°C; respectively.

The nanofibrous veil was carefully peeled off from the surface of the carbon fabric and cut into small pieces. They were weighted with an accuracy of 0.0001g. The average PVA nanofiber areal weight was measured to be approximately 7.1 ±0.70 g/m² whereas the average PA nanofiber areal weight density (AWD) for 30 and 60 minute deposition were determined approximately as 0.525 g/m² and 1.05 g/m², respectively. This corresponds to 2% for PVA nanofibers and 0.15 and 0.30% for PVA nanofibers

weight increase in the carbon fabric that is insignificant for those fabrics (350 g /m² areal density).

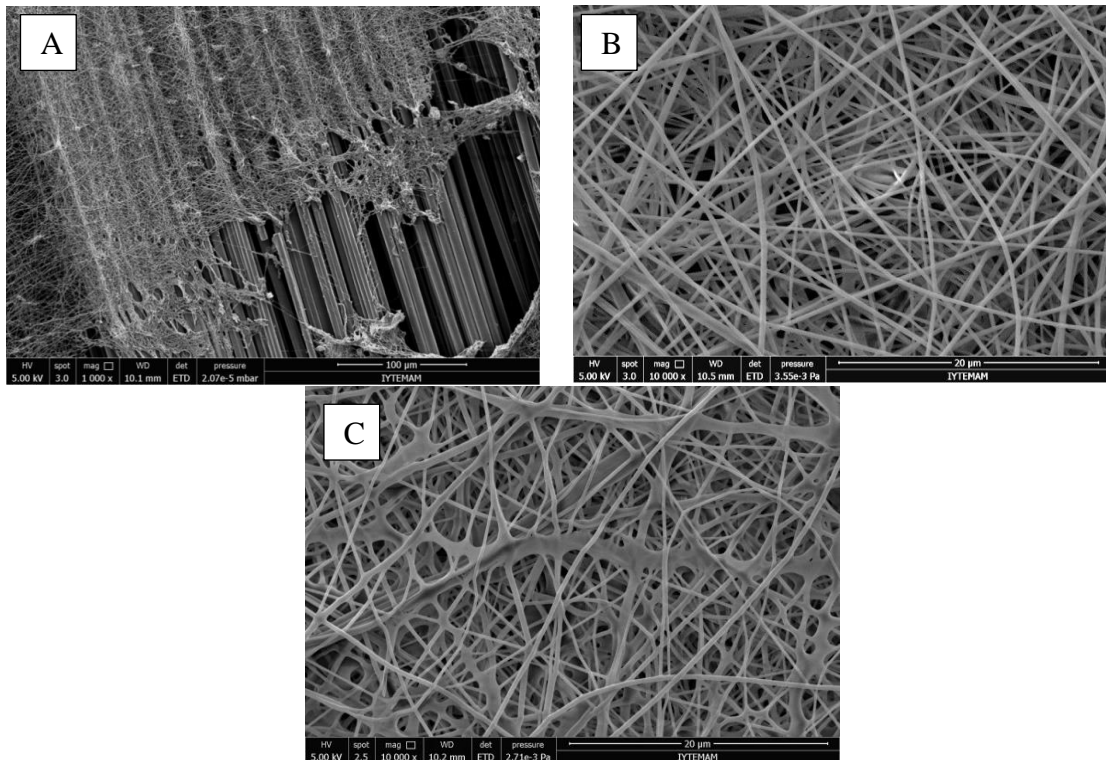


Figure 3.2.4.(a-b) SEM images of PVA nanofibers deposited on a carbon fabric and (c) PVA nanofibers after heat treatment.

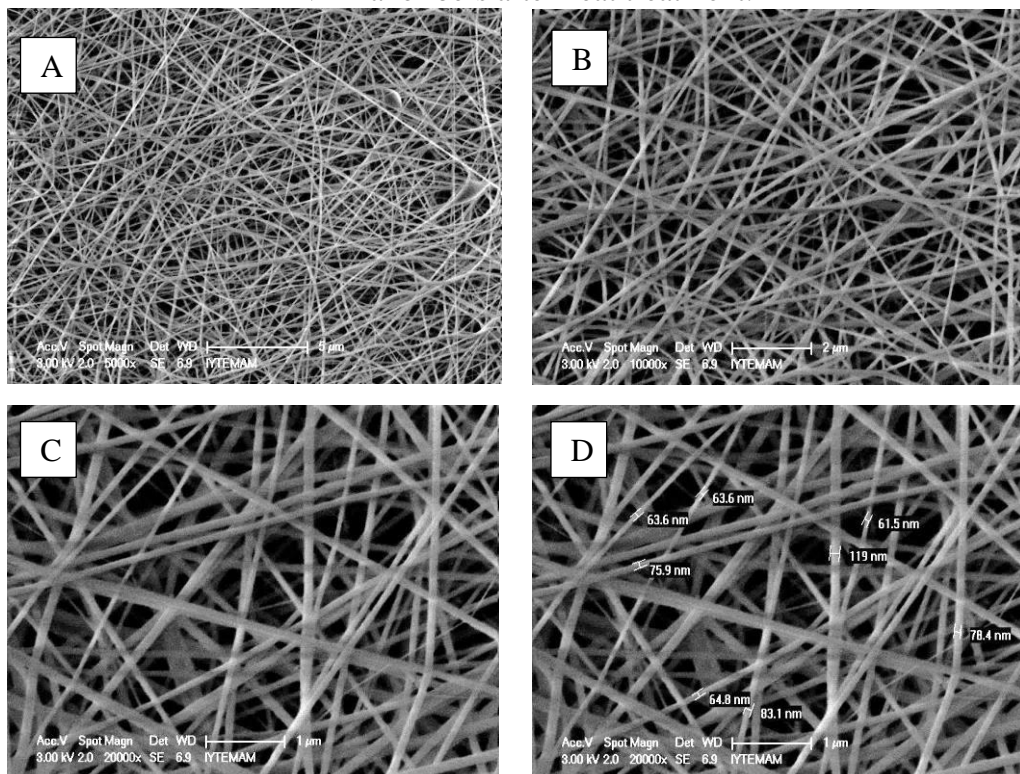


Figure 3.2.5 SEM images of electrospun PA66 nanofibers

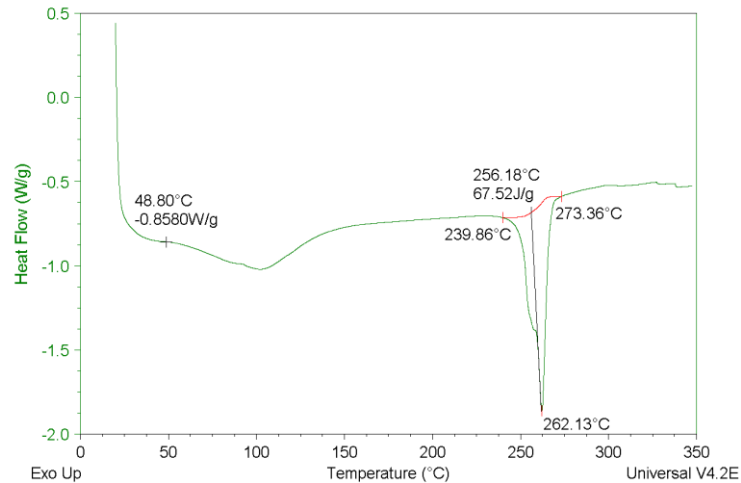


Figure 3.2.6. DSC curve of the PA66 nonwoven veils

3.3. Manufacturing of composite laminates

The reference and interleaved composite laminates with four layers of unidirectional carbon fabrics were fabricated by VaRTM process. Figure 3.3.1 shows the VaRTM set-up used in this study. In the interleaf laminates, one veil was placed between the second and third unidirectional plies for Mode-I fracture toughness tests. For the other in-plane mechanical tests, one veil was between each unidirectional carbon fabric. Figure 3.3.2 shows schematic representation of the (a) reference and (b) interleaved composite laminates. A polyimide film (Kapton, 50 μm thick) was inserted in the middle of the plies to form an initial crack along the interlaminar region of the DCB specimens.

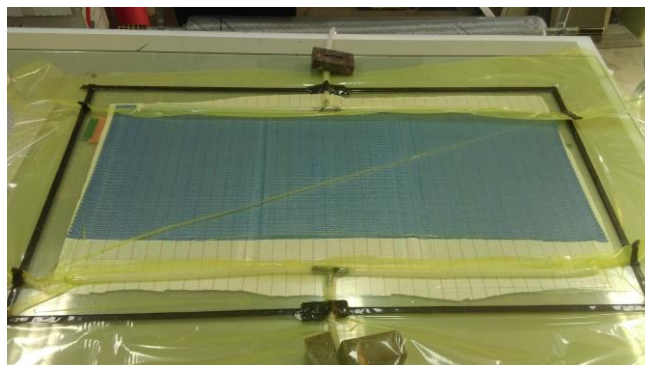


Figure 3.3.1. Schematic representation of the (a) reference and (b) interleaved composite laminates

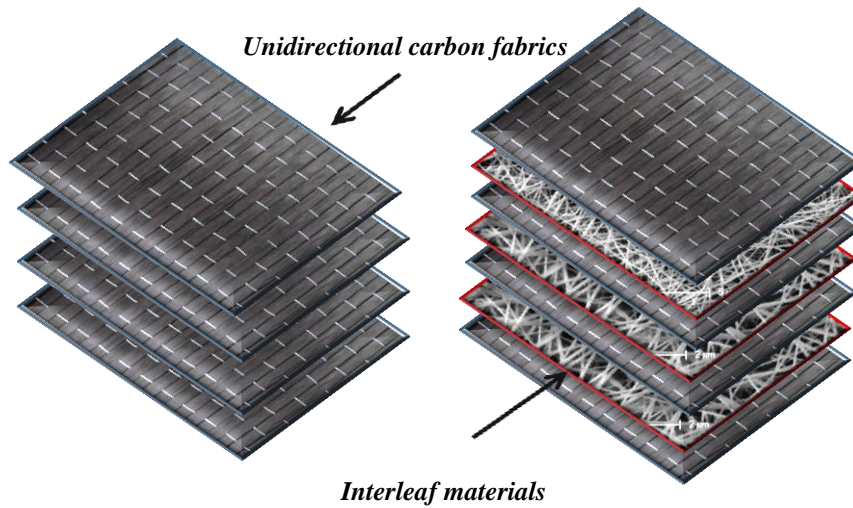


Figure 3.3.2. Schematic representation of the (a) reference and (b) interleaved composite laminates

In order to observe the change in resin flow during the manufacturing process, reference and interleaved specimens were prepared in the same vacuum bag. Based on the visual observations during the VaRTM process, no change of the resin flow due to the interleaf materials was detected. Demolding of the manufactured composites was carried out after complete curing at room temperature, followed by a post curing in an oven at 80°C for 12 h. The fabricated composites were cut into the desired dimensions using a water-cooled diamond saw and a water-jet. The cut edges of the specimens were lightly sanded with 280 grit sandpaper by hand. Non-interleaved composite specimens were coded hereinafter as “Reference”. The average thickness of reference composite specimens was 1.32 mm. Table 3.2 presents the interleaved composite test specimens with their designated group codes.

Table 3.2. Designation codes for composite test specimens

Interleaf material	Fiber type	Fiber diameter	Areal weight density (AWD) (g/m²)	Average thickness (mm)	Designated group code
Aramid	Micro	16 μm	8.5	1.54	m-AR
PA66	Micro	20 μm	17	1.62	m-PA66-17
PA66	Micro	20 μm	50	1.82	m-PA66-50
PVA	Nano	330 nm	0.70	1.35-1.37	nPVA
PA66	Nano	87 nm	0.525	1.35-1.37	nPA66-AWD-0.525
PA66	Nano	87 nm	1.05	1.35-1.37	nPA66-AWD-1.05

3.4. Mechanical characterization of composite specimens

In order to determine the effects of interleaf materials on the mechanical properties of CF/EP composites, a series of mechanical tests such as tensile, three-point bending, compression, Mode-I fracture toughness and Charpy impact tests were carried out on the reference and interleaf-modified specimens. All mechanical tests were carried out under room temperature in accordance with the relevant ASTM standards. In this section, the mechanical tests were described in this section.

3.4.1. Tensile tests

The tensile tests were carried out at a constant crosshead speed of 2.0 mm/min up to failure in order to determine tensile modulus and strength of the reference and interleaved composite specimens. A clip-on extensometer with knife edges was used to measure the strain. Instead of using rectangular specimens, dumbbell-like shape specimens were prepared and tested to prevent failure occurred underneath the end tabs. Tensile gripping end tabs were attached to reduce stress concentrations in the grip areas. Figure 3.4.1 shows the geometry of the tensile test specimens used in this study. The stress concentration factor was calculated as 1.30 due to the curved length in the specimens.

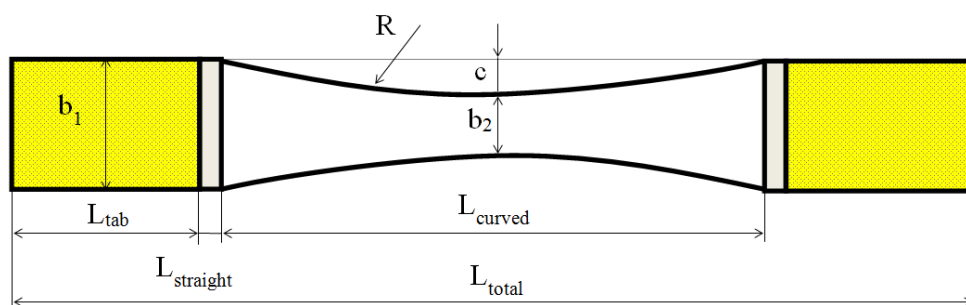


Figure 3.4.1. Geometry of a dumbbell-like shape tensile test specimens

The total length (L_{total}) and the width (b_1) of the specimen were 250 and 25 mm respectively. The length (L_{curved}) and radius of the curve (R) were 150 and 964.65 mm

respectively. Detailed information about the geometry of the tensile specimens can be found in Refs. [84, 85]. Figure 3.4.2 shows a tensile test specimen under tension.

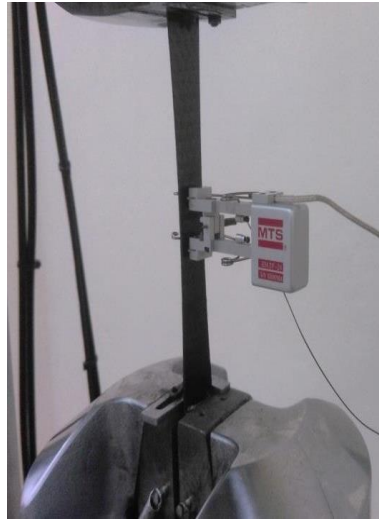


Figure 3.4.2. A dumbbell-like shaped tensile test specimen under tension

For numerical simulations, the reference tensile test specimens were also tested in the transverse direction. In order to determine shear modulus (G_{12}), the composite specimens were cut at a 45° orientation and tested under tension at a crosshead speed of 2 mm/min. First, E_x was determined then G_{12} was calculated by using the following formula [86];

$$G_{12} = \frac{1}{\left(\frac{4}{E_x} - \frac{1}{E_1} - \frac{1}{E_2} + \frac{2\nu_{12}}{E_1} \right)} \quad (1)$$

where E_1 and E_2 represent the longitudinal and transverse modulus respectively. ν_{12} is the poisson ratio in plane of 1–2.

3.4.2. Three-point bending and interlaminar shear strength (ILSS) tests

The flexural properties (flexural modulus and strength) of the reference interleaved specimens were determined from three point bending tests. Figure 3.4.3

shows a composite specimen under flexural loading. A span-to-thickness ratio of 32:1 was used on the test fixture. The rate of crosshead motion was calculated for each group of specimens as recommended in the ASTM standard. The interlaminar shear strength (ILSS) tests were determined using the short beam shear test. A span-to-thickness ratio of 8:1 was used with a span of 10 mm on the test fixture. The test speed was 1 mm/min.

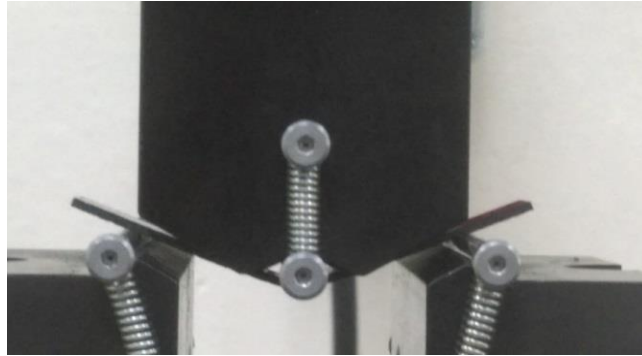


Figure 3.4.3. A composite test specimen under flexural loading

3.4.3. Compression tests

The compressive strength and modulus of the specimens were determined using an anti-buckling fixture (Figure 3.4.4). The dimensions of the compression test specimens were 140 mm in length and 12.7 mm in width. The gauge length was 12.7 mm. The specimens were loaded until failure at a constant crosshead speed of 1.3 mm/min.

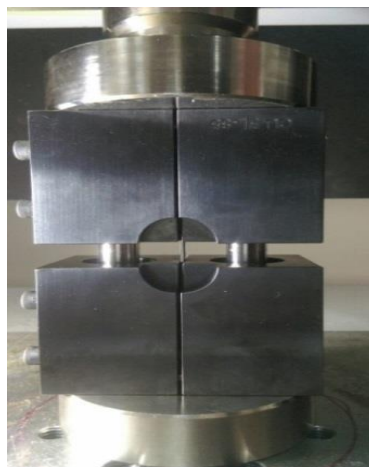


Figure 3.4.4. Anti-buckling fixture used for compression tests.

3.4.4. Charpy-impact tests

Charpy impact tests were carried out according to ISO-179 standard on 10 x 80 mm rectangular notched specimens, using the CEAST® Resil Impactor having maximum hammer energy of 15 J and hammer tangential speed of 3.46 m/s. The Charpy impact strength was calculated dividing the energy by the area under the notch. At least ten specimens were tested for each group to obtain consistent average and standard deviation values.

3.4.5. Mode-I fracture toughness tests

The Mode-I interlaminar fracture toughness of the composite specimens was determined by double cantilever beam (DCB) experiments. The configuration of the specimens for DCB testing was shown in Figure 3.4.5.

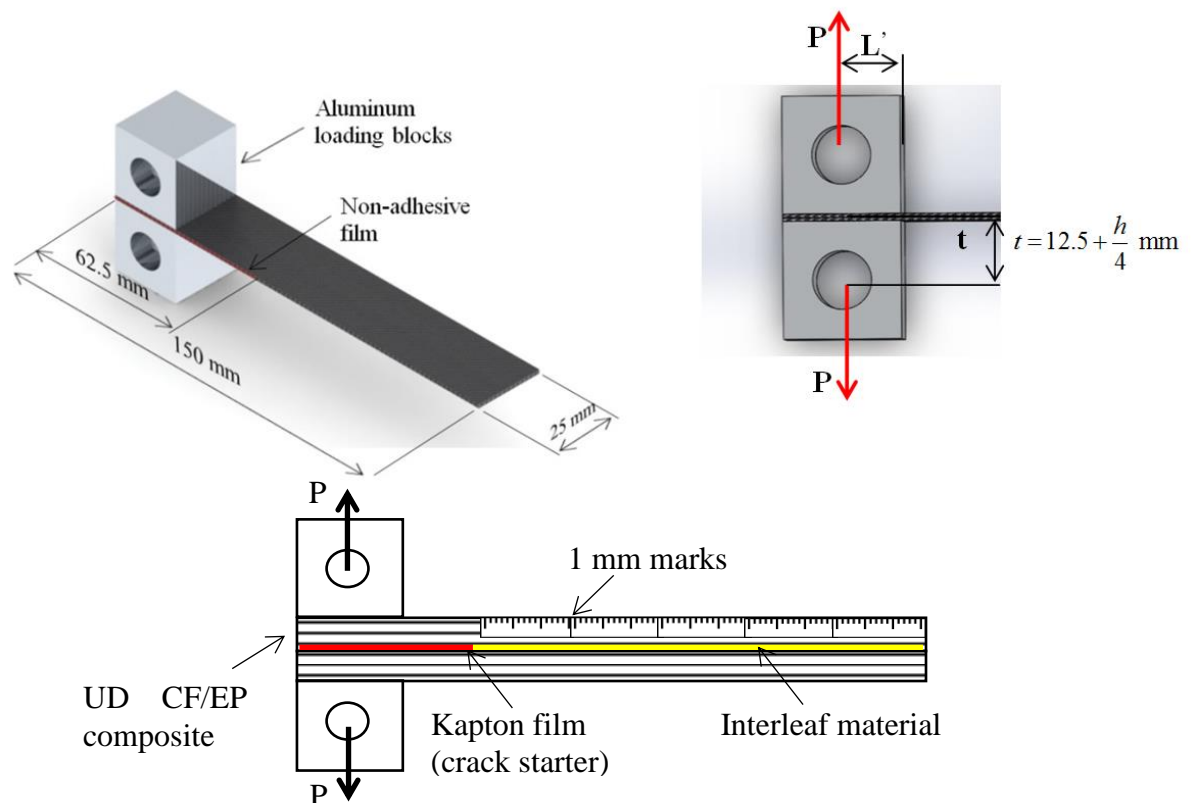


Figure 3.4.5. Schematic representation of the DCB test specimens.

The dimensions of the DCB test specimens were L=150 mm in length and b=25 mm in width. Aluminum blocks were bonded to outer surfaces of the DCB specimens to transfer the opening forces. Before testing, the edges of the specimens were painted with white color and marked with a 1-mm interval in order to observe the crack propagation. The force, displacement and crack length values were recorded simultaneously until the separation of the test specimen was completed. Each specimen was initially loaded with a crosshead speed of 1 mm/min and the crack was allowed to propagate a short distance (3–5 mm) before the specimen was unloaded. Then, the specimen was loaded until the crack propagates about 50-60 mm from tip of the crack. Load, opening displacement and crack length were recorded for the energy release rate (G_I) calculation during the tests. G_I was calculated from Modified Beam Theory data reduction method given as follows [87]:

$$G_I = \frac{F}{N} \frac{3P\delta}{2b(a + |\Delta|)} \quad (2)$$

where G_I is the Mode I interlaminar fracture toughness, P is the applied load, δ is the load point displacement, b is the specimen width, a is the delamination length (crack length), Δ is a value that is determined experimentally by generating a least squares plot of the cube root of compliance ($C^{1/3}$) as a function of delamination length. F and N are the correction parameters to take into account large displacement and the stiffening of the specimens by loading blocks, respectively. These correction factors can be calculated by using the following equations [87];

$$F = 1 - \left(\frac{3}{10}\right)\left(\frac{\delta}{a}\right)^2 - \left(\frac{3}{2}\right)\left(\frac{\delta t}{a^2}\right) \quad (3)$$

$$N = 1 - \left(\frac{L'}{a}\right)^3 - \left(\frac{9}{8}\right)\left[1 - \left(\frac{L'}{a}\right)^2\right]\left(\frac{\delta t}{a^2}\right) - \frac{9}{35}\left(\frac{\delta}{a}\right)^2 \quad (4)$$

where t and L' were shown in Figure 3.4.5. The G_{IC} initiation ($G_{IC, ini}$) value was determined as the value of G_{IC} at which the delamination was visually observed on the edge of the specimen. G_{IC} propagation ($G_{IC, prop}$) value was calculated as the average of

the values of G_{IC} during crack propagation. Figure 3.4.6 shows a composite test specimen under Mode-I loading.

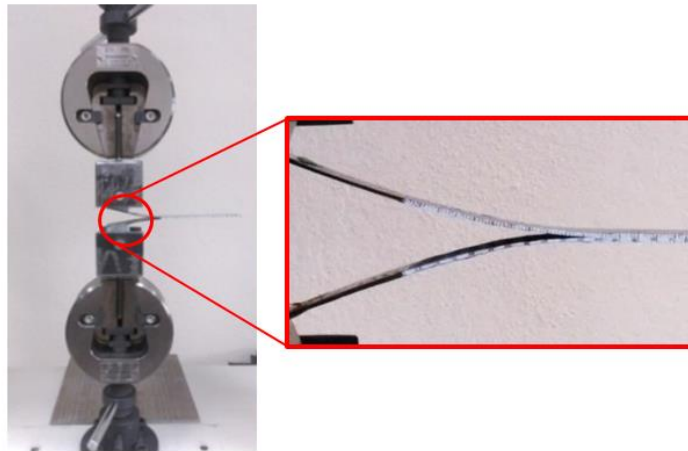


Figure 3.4.6. A composite test specimen under Mode-I loading

3.5. Fractured surface observations and dynamic mechanical analysis (DMA)

Scanning electron microscopy (SEM) observations were made to determine micro and nanofiber morphologies and to better understand the toughening mechanisms in the interleaved composites. The specimens were sputter-coated with gold for 90 seconds and examined under a Philips XL 30S FEG scanning electron microscope. Dynamic mechanical analysis (DMA) was carried out on the specimens by using a DMA Q800 (TA Instruments, USA) equipment in a dual cantilever mode. The dimensions of the specimens were 65 mm in length and 10 mm in width. At least three specimens were tested for each laminate. The heating rate was $2^{\circ}\text{C}/\text{min}$ from room temperature to 150°C and the frequency was 1 Hz. The glass transition temperature (T_g) of the reference and modified composite specimens were determined from the $\tan\delta$ (peak) spectrum. Dynamic and loss modulus of the composite specimens were also determined.

3.6. Calculation of carbon fiber volume fraction (V_f)

The carbon fiber content of the composite specimens was determined by using the density method. This method is very effective for determining the fiber volume fraction of fiber reinforced composite laminates. The carbon fiber volume fraction of the specimens (V_f) was calculated by measuring the density of the composite in air and in distilled water.

In order to determine the V_f of composite laminates, five composite specimens from each group were prepared using a water-cooled diamond saw. Each specimen was dried in an oven at 40°C for 30 minutes. Then the specimens were weighted in air then weighted in distilled water. The densities of carbon fiber and resin were assumed as 1.80 g/cm³ and 1.16 g/cm³, respectively. The density of the composite materials was calculated by Archimedes' Principle using the following equation [88]:

$$\rho_c = \frac{W_{air}\rho_{water}}{W_{air} - W_{water}} \quad (5)$$

where ρ_c and ρ_{water} is density of composite and distilled water, respectively. W_{air} and W_{water} is the weight of specimen in air and the weight of sample in distilled water. The fiber volume fraction of composite plate was measured using the rule of mixtures using the following equation [88]:

$$V_f = \frac{\rho_c - \rho_{resin}}{\rho_{fiber} - \rho_{resin}} \quad (6)$$

CHAPTER 4

RESULTS AND DISCUSSION

4.1. Effects of interleaf materials on carbon fiber volume fraction (V_f) of CF/EP composites

Table 4.1 shows the carbon fiber volume fraction (V_f) of composite specimens. The V_f of the reference specimens were determined as 0.55. It was observed that the presence of micro-scaled interleaf materials in the interlaminar region reduced the V_f of composites. The decrease in V_f was about 10.9, 15.1 and 25.9 % for m-AR, m-PA17 and m-PA50 composites, respectively. The main reasons for reduced V_f were the addition of high amount of less stiff fibers in the interlaminar region and the increased thickness of resulting laminate. For nPVA, nPA66-AWD-0.525 and nPA66-AWD-1.05 composites, no significant change was observed in the V_f of composites as compared to reference specimens. The V_f was varied as in the range between 0.55-0.54 for reference nano interleaved specimens. The amount of nanofibers in the interlaminar region was very low therefore the V_f was not significantly affected with the addition of these nanofibers.

Table 4.1. Carbon fiber volume fraction (V_f) of composite specimens

Code	Nonwovens in composite (wrt. total carbon fiber weight, %)	The average carbon fiber volume fraction (V_f)	% decrease
Reference	-	0.55	-
m-AR	1.82	0.49	10.9
m-PA17	3.64	0.47	15.1
m-PA50	10.71	0.41	25.9
nPVA	0.15	0.54-0.55	<i>No significant change</i>
nPA66-AWD-0.525	0.11	0.54-0.55	<i>No significant change</i>
nPA66-AWD-1.05	0.225	0.54-0.55	<i>No significant change</i>

4.2. Effects of interleaf materials on the tensile properties of CF/EP composites

Figure 4.2.1 and Figure 4.2.2 show the stress-strain curves of the reference and m-AR interleaved specimens, respectively. The elastic modulus and tensile strength of the reference composites were determined as 122.2 ± 3.4 GPa and 1792.0 ± 96 MPa, respectively. The shear modulus (G_{12}) of the reference specimens was determined as 4.2 GPa. The incorporation of m-AR interleaves in the interlaminar region reduced the elastic modulus of the composites from 122.2 GPa to 114.7 GPa. Also, the tensile strength decreased from 1792 to 1560 MPa with the addition of m-AR nonwovens. The decrease in elastic modulus and tensile strength was 6.1 and 13% respectively. The main reason for this decrease was reduced carbon fiber volume fraction with increased thickness in the composites. Also, the void formation formed in the resulting composite caused reduction in the tensile properties as reported in the literature.

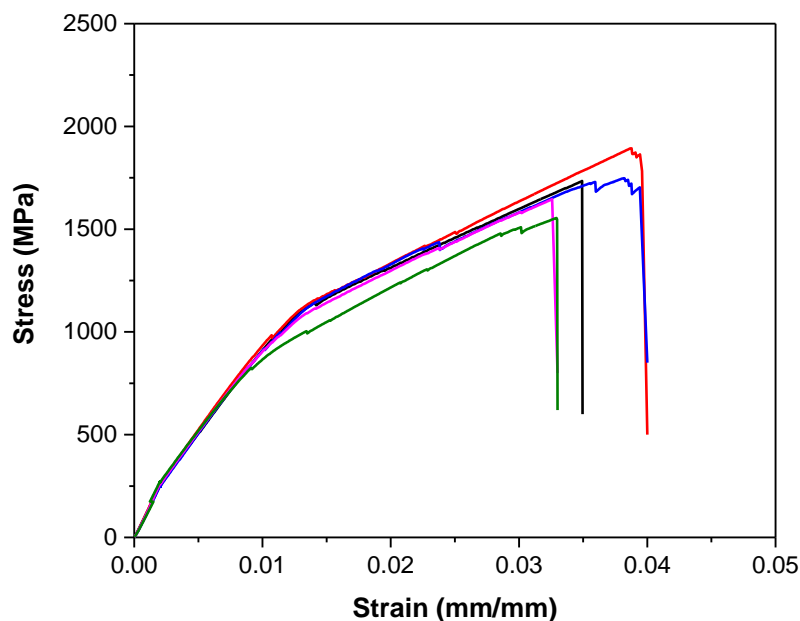


Figure 4.2.1. Stress-strain curves of reference composite specimens

Figure 4.2.3 and Figure 4.2.4 show stress-strain curves of the m-PA66-17 and m-PA66-50 composite specimens respectively. Incorporating m-PA66-17 veil into the interlaminar region reduced fiber volume fraction from 55 to 47%, and hence, the

elastic modulus and tensile strength of the composites reduced by 10.97 and 19.70% respectively. The addition of denser m-PA66-50 in the interlaminar region led to higher reduction in the carbon fiber volume fraction and increased the thickness of the composites. Therefore, the elastic modulus and tensile strength of m-PA66-50 interleaved specimens were 33.59 and 41.26% lower than those of the reference specimens. The failed m-PA66-50 composite tensile test specimens were shown in Figure 4.2.5.

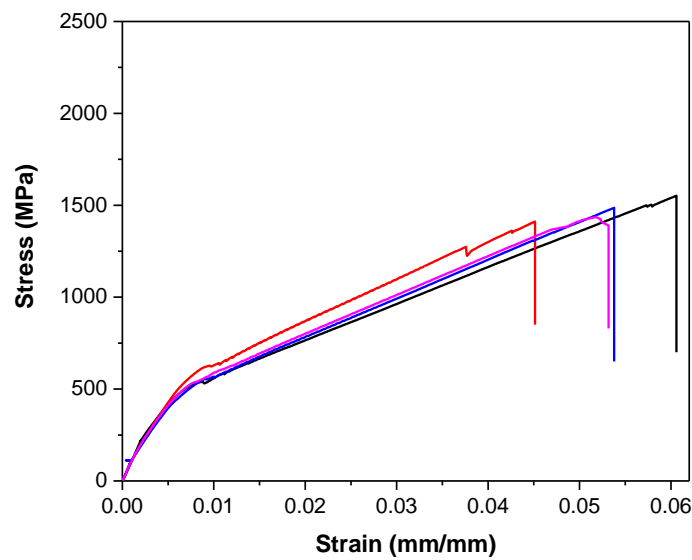


Figure 4.2.2. Stress-strain curves of the m-AR composite specimens

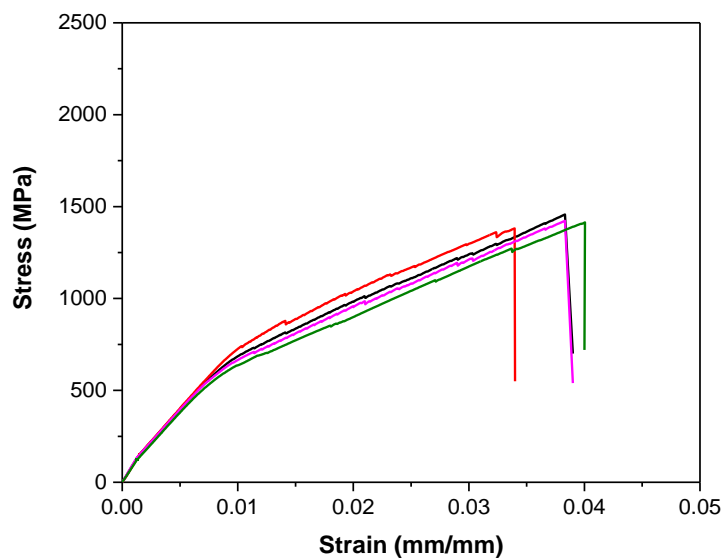


Figure 4.2.3. Stress-strain curves of m-PA66-17 composite specimens

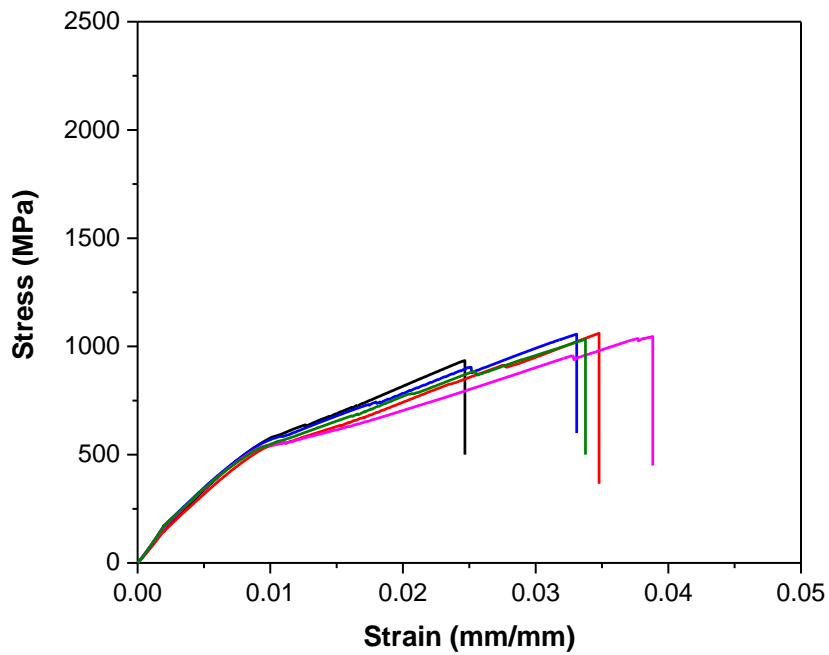


Figure 4.2.4. Stress-strain curves of m-PA66-50 composite specimens

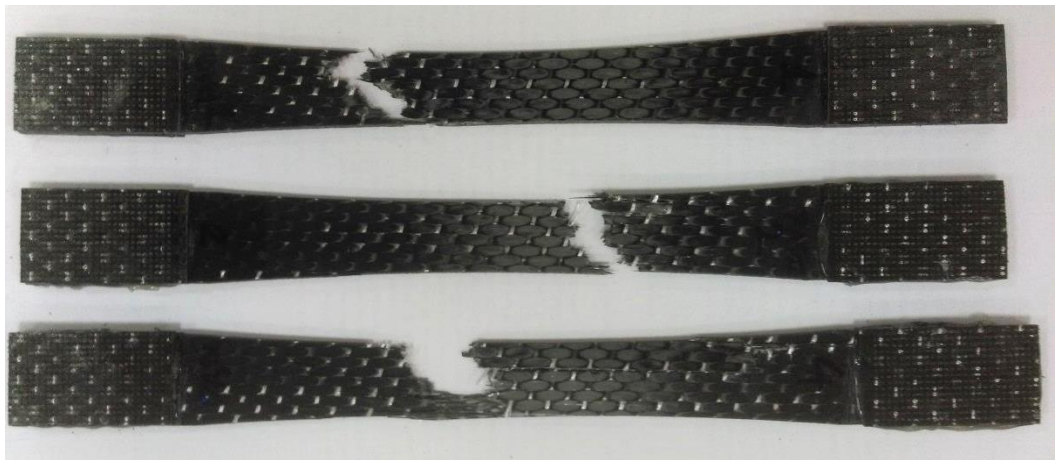


Figure 4.2.5. Failed m-PA66-50 composite tensile test specimens

Figure 4.2.6 shows stress-strain curves of the nPVA composite specimens. The elastic modulus of the specimens was calculated as 121.2 ± 6.12 GPa. No significant change observed in the elastic modulus as compared to reference specimens. This is due to the fact that the amount of PVA nanofibers was very low and the thickness of the specimens was not significantly changed after the addition of these nanofibers. Also, the carbon fiber volume fraction of the specimens was almost the same with the reference

specimens. Another important observation was that the presence of PVA nanofibers on the interlaminar region increased the tensile strength of the composites from 1792 MPa to 1917 MPa which corresponds to 7% increase. This is due to improved matrix cracking resistance at the free edges. The plastically deformed and necked PVA nanofibers and excessive deformation of epoxy matrix can be seen in Figure 4.2.7. These results also confirm previous study by Bilge et al. [76], demonstrating PVA nanofiber interleaving can improve the tensile strength of carbon/epoxy composites.

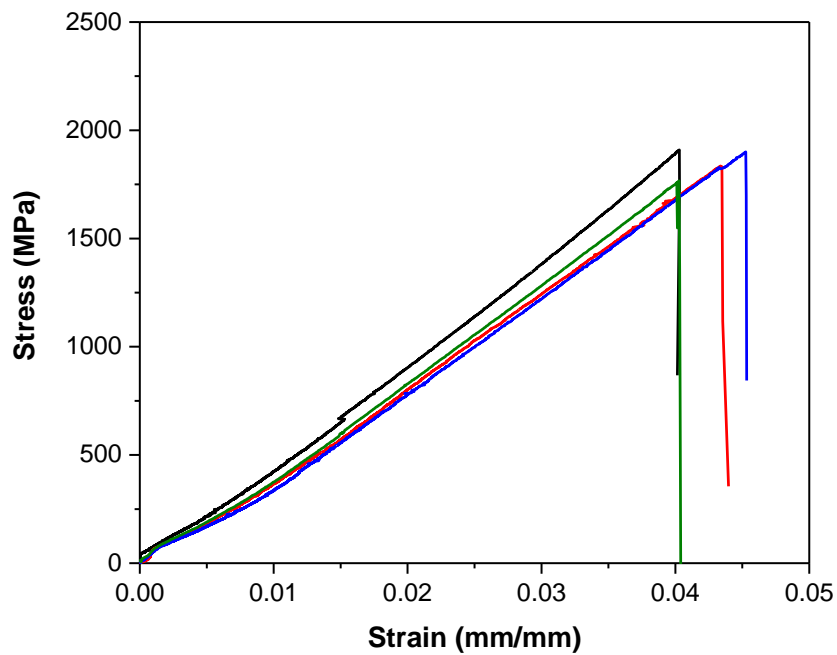
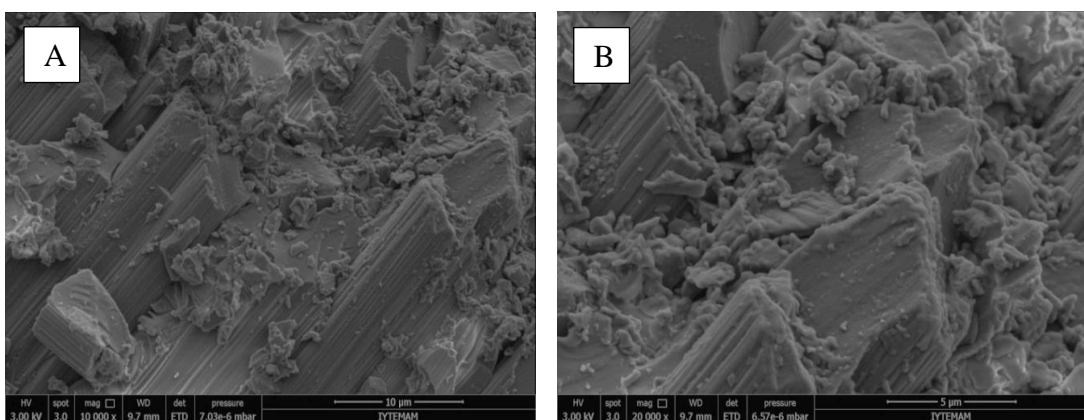


Figure 4.2.6. Stress-strain curves of nPVA composite specimens



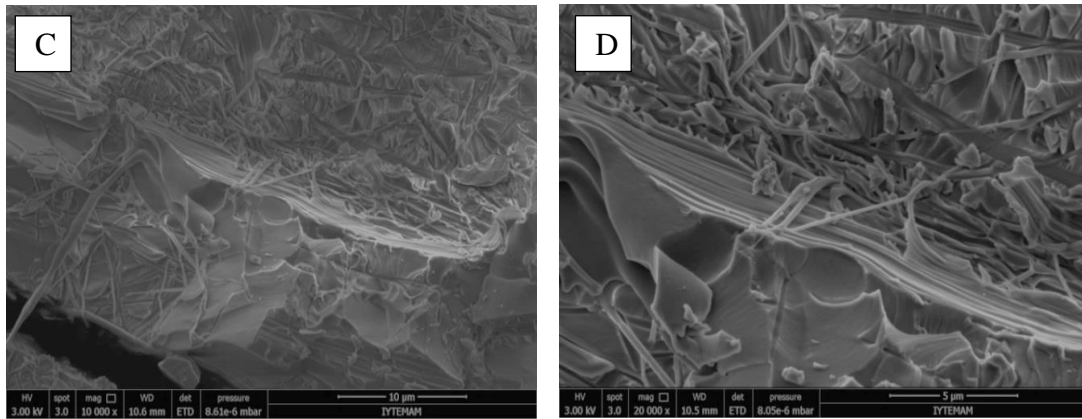


Figure 4.2.7. SEM images of the (a-b) reference, (c-d) nPVA composite test specimens after tensile loading.

Figure 4.2.8 and Figure 4.2.9 show stress-strain curves of the nPA66-AWD-0.525 and nPA66-AWD-1.05 composite specimens. The elastic moduli of the nPA66-AWD-0.525 and nPA66-AWD-1.05 specimens were determined as 121.5 ± 8.8 GPa and 120.8 ± 3.93 GPa respectively. No significant change was recorded in the elastic modulus of nPA66 interleaved composites as observed in nPVA composite specimens.

The tensile strength of the nPA66-AWD-0.525 and nPA66-AWD-1.05 composite specimens was determined as 1713.4 ± 195 MPa and 1616.2 ± 208 MPa respectively. The nPA66-AWD-1.025 composite specimens reduced the tensile strength about 9.8%. This can be attributed to the formation of local beads in the interlaminar region of the composites. Figure 4.2.10 shows the SEM image of the presence of the local beads in the tensile n-PA66 composite test specimens. As it is well-known, nanofibers with beads have lower strength and stiffness values as compared to bead-free ones. This is due to the higher stress concentrations around the beads which occur when the nanofibers are stretched. Also, these beads cause local defects in the matrix and reduce the tensile strength of the composites. The lower tensile strength in n-PA66 interleaved specimens can be associated with the possible moisture uptake before resin infusion in composite manufacturing step. Another observation was that the standard deviations of the tensile strength data of nPA66 composite specimens were higher than those of the reference specimens. This may be related with the local mat thickness variations in the interlaminar region. It was also note-worthy that small load-drops were observed during the tensile tests. Therefore it can be said that PA66 nanofibers were able to suppress the onset and growth of delamination and delay final failure of

composite. Figure 4.2.11 shows the SEM images of nPA66 nanofiber interleaved composite specimens under tensile loading.

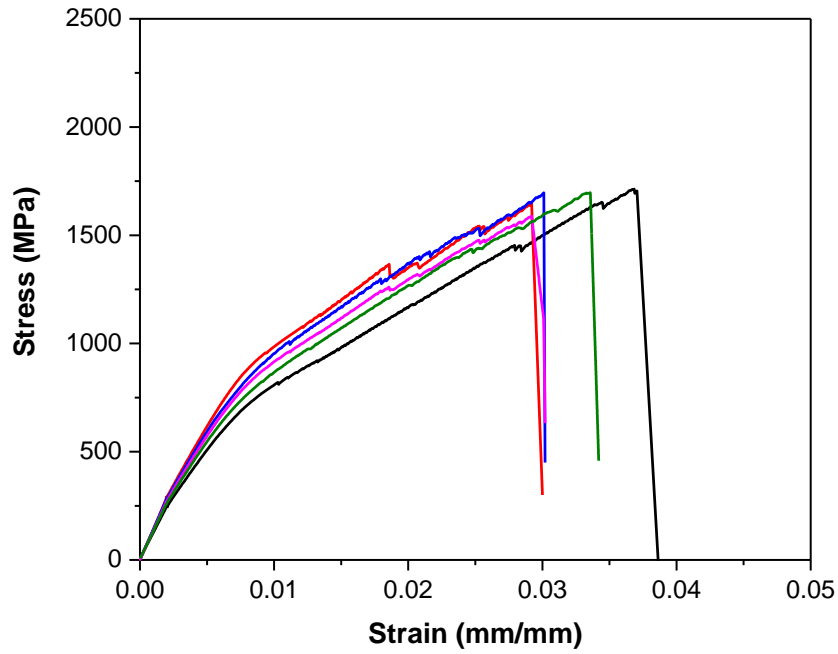


Figure 4.2.8. Stress-strain curves of nPA66-AWD-0.525 composite specimens.

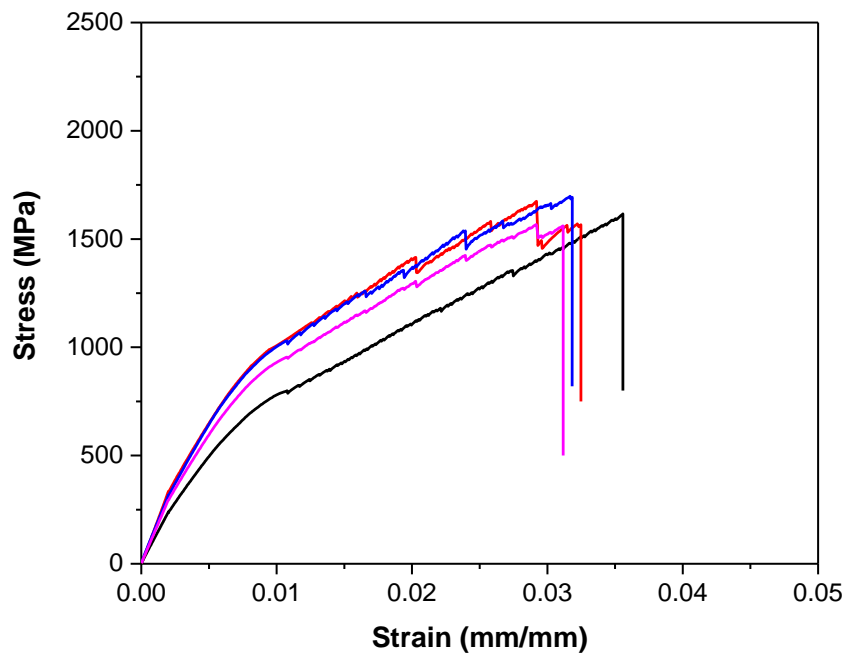


Figure 4.2.9. Stress-strain curves of nPA66-AWD-1.05 composite specimens

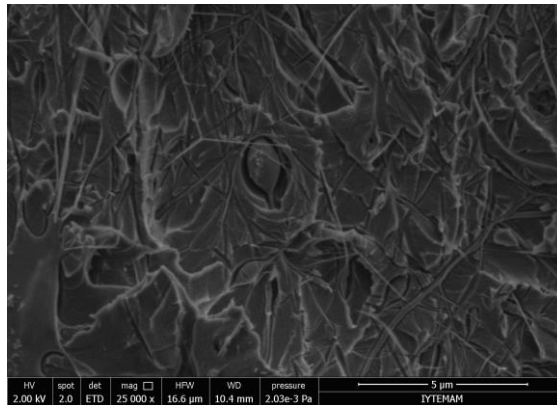


Figure 4.2.10. Local bead formations observed in n-PA66 composite specimens

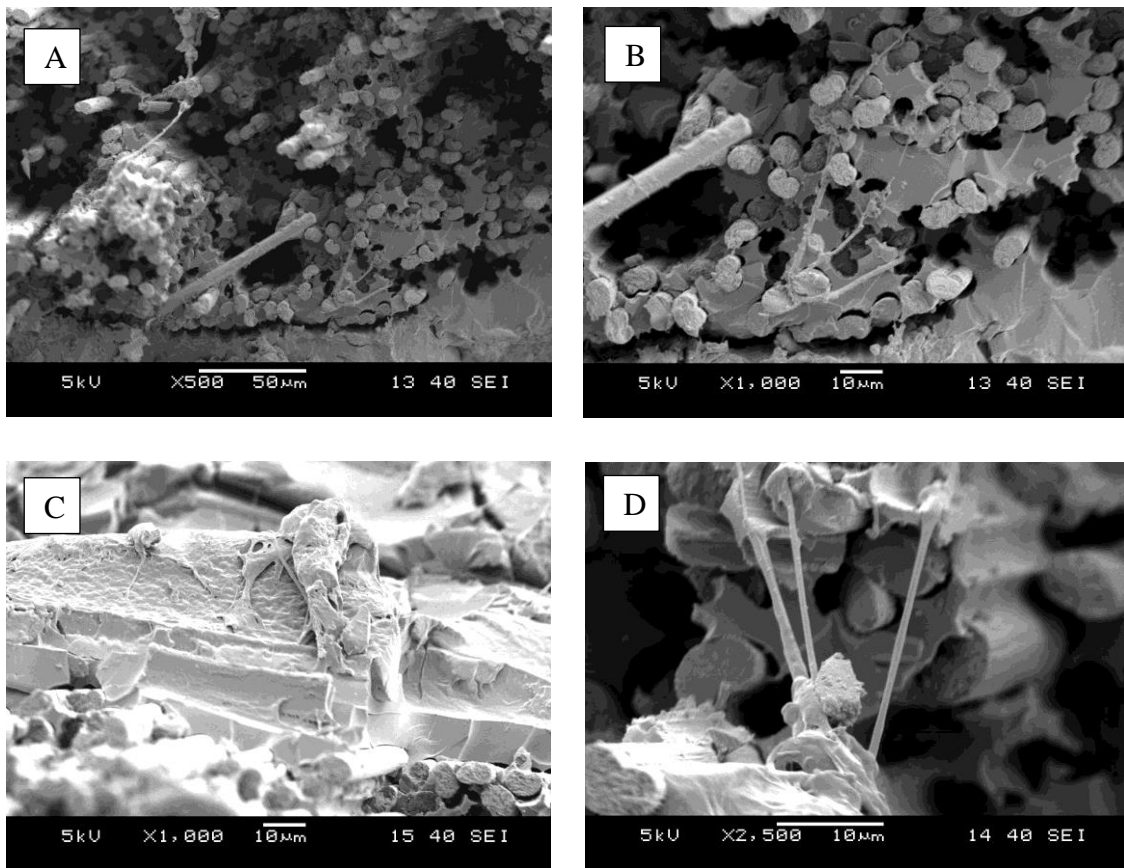


Figure 4.2.11. SEM images of n-PA66 composite specimens

Figure 4.2.12 and Figure 4.2.13 summarize the tensile test results of the composite specimens with/without interleaf materials. The micro-scaled PA66 interleaf materials caused a significant decrease in both elastic modulus and tensile strength of the composites. There is a decreasing tendency in tensile properties with the increase of ADW values of nonwovens. The increase in AWD reduced the tensile properties of composites due to the lower fiber volume fraction and increased thickness of the

resulting composite. It was also observed that the elastic modulus and tensile strength were less negatively affected by aramid nonwovens. This is due to lower amount of addition aramid microfibers (8.5gsm) in the interlaminar region of composites. Also, these microfibers were stiffer than the PA66 microfibers which resulted in lower decrease in these values.

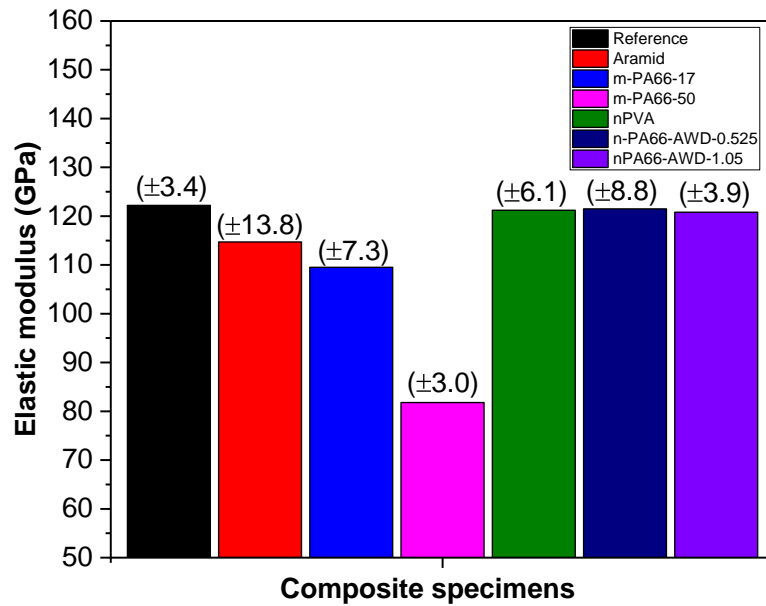


Figure 4.2.12. Elastic modulus of composite test specimens

As compared to micro-scaled interleaf materials, it is obvious that the nanofibers were less likely to have a negative effect on the tensile properties of the composites. No significant change in elastic modulus was observed in the case of nano-scaled interleaf materials. The reason was that the fiber volume fraction and thickness of the composite specimens were not significantly influenced by the addition of PVA and PA66 nanofibers. The PA66 nanofibers in the interlaminar region caused a reduction in tensile strength of composite unexpectedly whereas PVA nanofibers increased the tensile strength about 7% as compared to reference specimens interestingly. This increase can be associated with the reduction in stress concentrations at free edges of the composite specimens due to PVA nanofibers. There are other studies in the literature which support this hypothesis as in the study of Bilge et al [76]. It was believed that the reduction in tensile strength of nPA66 composites was most probably due to the local

thickness variations in the nonwoven veil thickness possibly occurred during the electrospinning process and most probably due to the manufacturing imperfections during the production of composite laminates. As a result of nonwoven thickness variations, higher standard deviation was recorded for tensile strength as compared to the reference specimens.

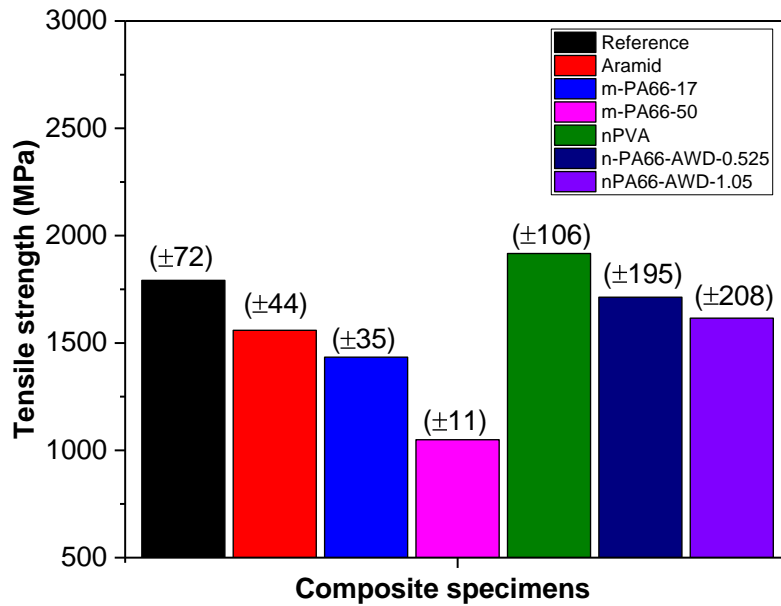


Figure 4.2.13. Tensile strength of composite test specimens

4.3. Effects of interleaf materials on the flexural and interlaminar shear properties of CF/EP composites

Figure 4.3.1 and Figure 4.3.2 show the stress-strain curves of the reference and m-AR interleaved specimens under flexural loading, respectively. As expected, the force increased until it reached to its maximum value and sudden failure occurred. The flexural modulus and strength of the reference composites were determined as 104.7 ± 5.9 GPa and 1207.2 ± 49.6 MPa, respectively. On the other hand, as seen in Figure 4.3.2, the m-AR specimens failed in a different manner so that the carbon plies of m-AR interleaved specimens were broken one by one which was observed during the tests

with small load-drops in load-displacement curves. Therefore, it can be said that the aramid interleaf materials changed the failure mode from catastrophic to non-catastrophic failure. The incorporation of m-AR interleaves in the interlaminar region reduced flexural modulus from 104.7 GPa to 84.0 GPa. Also, the flexural strength decreased from 1207 MPa to 1120 MPa. The addition of m-AR interleaf material reduced the flexural modulus and strength values about 19.7 and 7.2% respectively. The main reason for this decrease was reduced carbon fiber volume fraction and increased thickness of the composites.

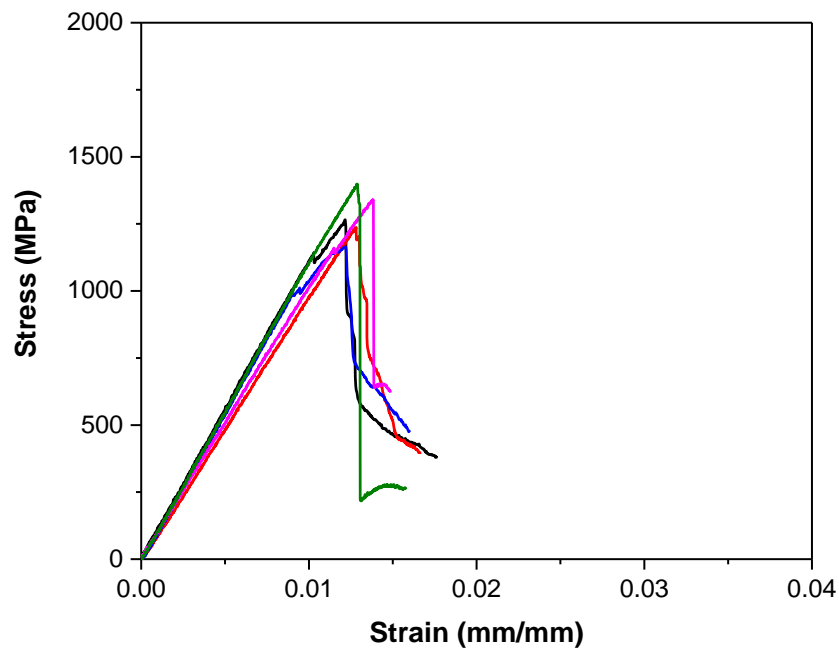


Figure 4.3.1. Stress-strain curves of reference composite specimens under flexural loading

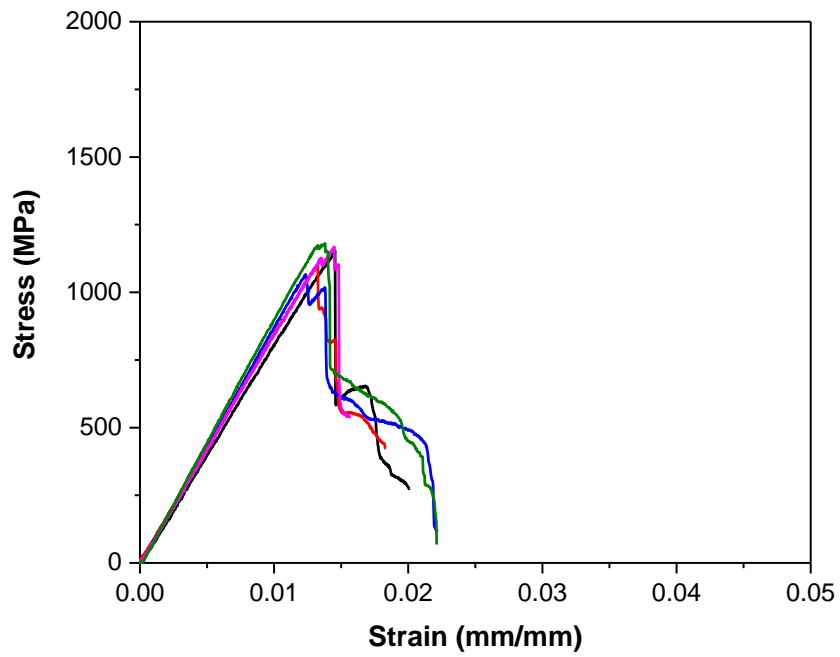


Figure 4.3.2. Stress-strain curves of m-AR composite specimens under flexural loading

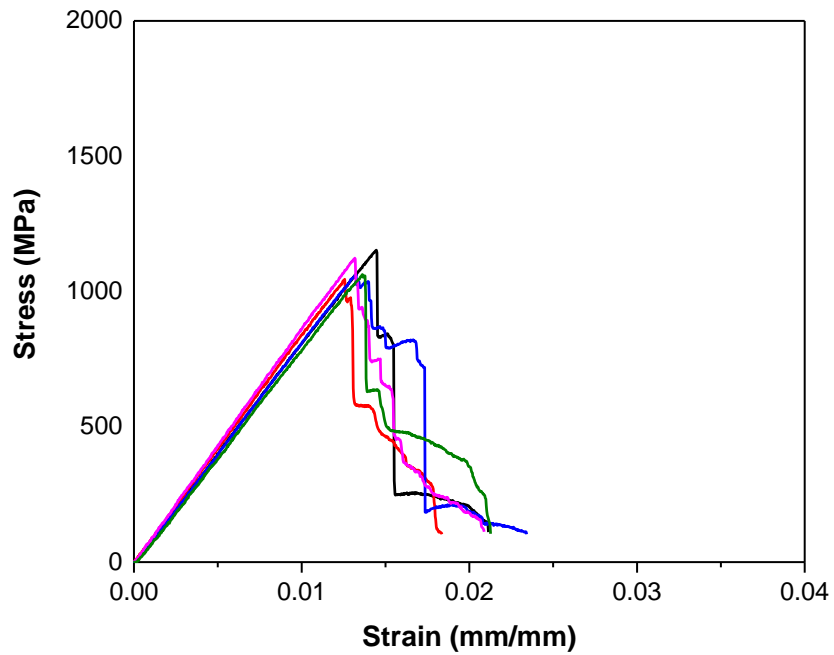


Figure 4.3.3. Stress-strain curves of m-PA66-17 composite specimens under flexural loading

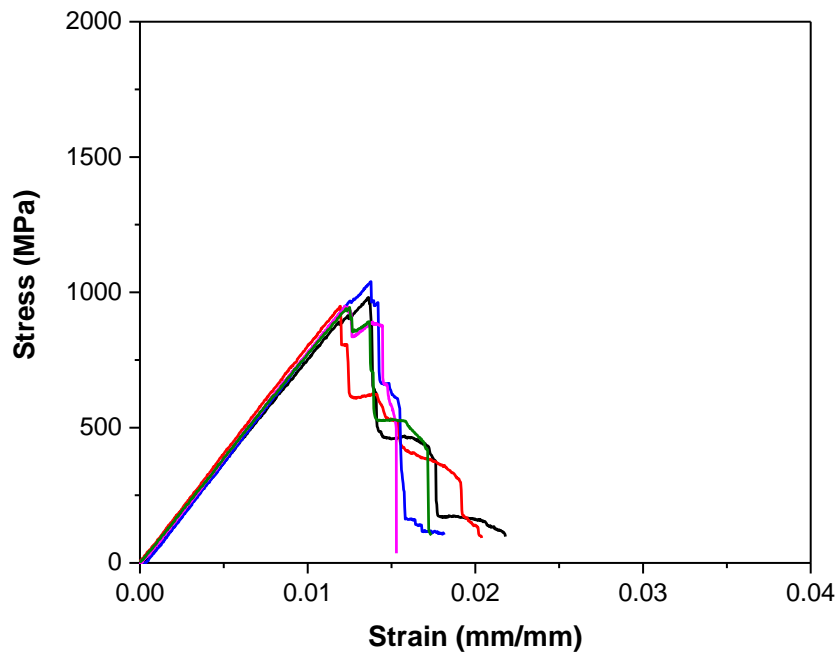


Figure 4.3.4. Stress-strain curves of m-PA66-50 composite specimens under flexural loading

Figure 4.3.3 and Figure 4.3.4 show the load-displacement curves of the m-PA66-17 and m-PA66-50 composite specimens under flexural loading. As in the case of m-AR interleaved composite specimens, the failure occurred with breaking of carbon plies one by one after the maximum force was reached. This behavior is one of the main characteristics of micro-scaled nonwoven interleaved specimens in which the failure mode becomes less catastrophic than the reference specimens. Incorporating 17 gsm of m-PA-66 veil into the interlaminar region increased the thickness of the specimen to 1.62 mm and reduced the carbon fiber volume fraction from 0.55 to 0.47. As a result, the flexural strength and flexural modulus decreased to 1119.6 MPa and 82.9 GPa, which were 12.62% and 20.8% lower than those of the reference specimens. The flexural modulus and strength of m-PA66-50 composite were determined as 75.93 ± 3.12 GPa and 1049.3 ± 10.9 MPa respectively. Increasing the areal density of the interleaf material from 17 gsm to 50 gsm caused higher reduction in flexural strength and modulus by 24.1 and 27.5% respectively, as compared to reference specimens due to

the increased thickness, lower carbon fiber volume fraction and lower stiffness of interleaf material surrounding the carbon fibers.

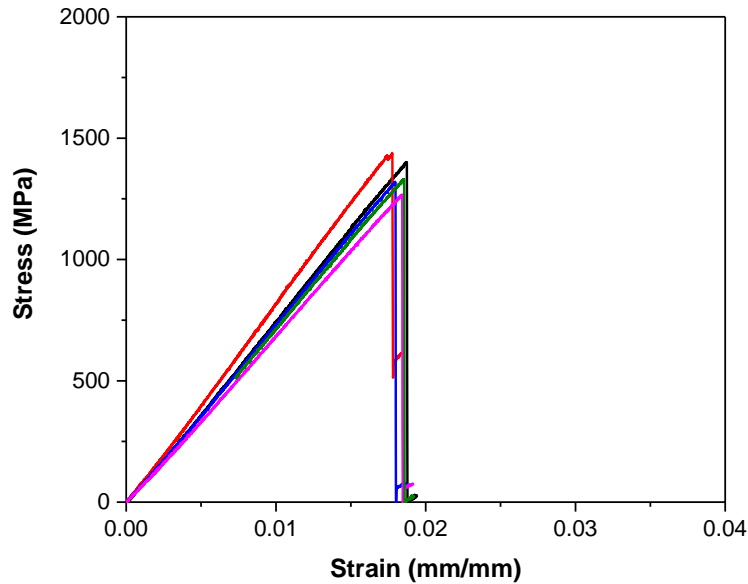


Figure 4.3.5. Stress-strain curves of nPVA composite specimens under flexural loading

Figure 4.3.5 shows the stress-strain curves of nPVA composite specimens under flexural loading. The flexural modulus was improved by 11% with PVA nanofiber interlayers. The flexural strength of PVA-modified composite specimens was 16% higher than those of reference specimens. The reason behind the bending performance will be explained in detail later. Figure 4.3.6 and Figure 4.3.7 show stress-strain curves of nPA66-AWD-0.525 and nPA66-AWD-1.05 composite specimens under flexural loading. It was observed that the incorporation of PA 66 nanofibers into the interlaminar region also resulted in significant improvement on the flexural modulus and strength of the composites. It was found that those values were increased by 15.64 and 12.80% for the composites that contains PA 66 nanofibers with a nanofiber AWD of 1.05 g/m². As compared to micro-scaled nonwoven interleaving, the nanofiber interleaving method improved flexural properties of composites for both nPVA and n-PA66 interleaf materials. At low strain values, the nanofibers increased flexural modulus and strength. As compared to reference specimens, higher maximum load values were recorded at higher strain values. This may be associated with the improved load-transfer capacity between the carbon fibers due to the presence of nanofibers in the interlaminar region.

Moreover, modified matrix properties may increase in-plane bending performance. These findings are consistent with those reported in the literature by Herwan et al. [75] and Palazzetti [89]. It was also noteworthy that flexural properties of the composites increased with the increase of areal weight density of nanofibers.

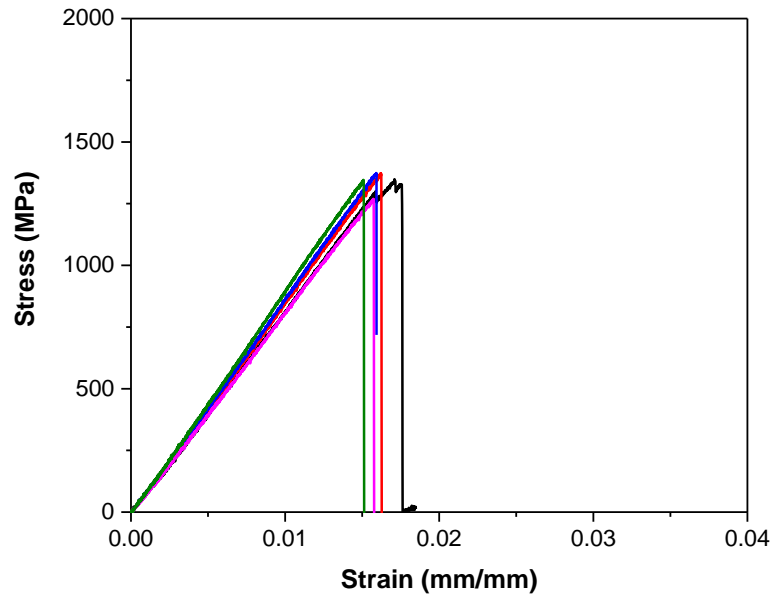


Figure 4.3.6. Stress-strain curves of nPA66-AWD-0.525 composite specimens under flexural loading

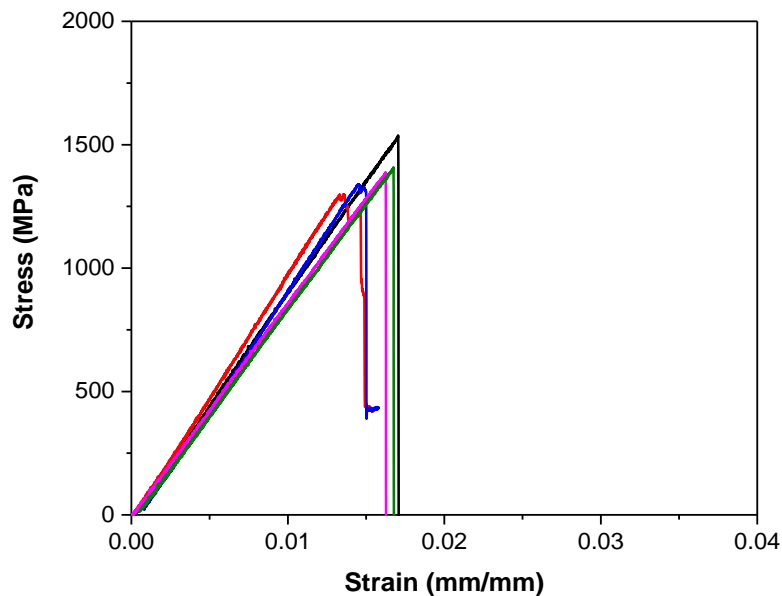


Figure 4.3.7. Stress-strain curves of nPA66-AWD-1.05 composite specimens under flexural loading

The flexural test results indicated that the micro-scaled interleaf materials, m-AR and m-PA66, reduced the flexural strength and modulus values of resulting composites. This is due to the fact that lower carbon fiber volume content causes lower flexural strength and modulus for the m-AR and m-PA66 interleaved composite specimens. On the other hand, the nano-scaled interleaf materials led to significant increase in flexural performance of CF/EP composites. This may be associated with the improved load-transfer capacity between the carbon fibers due to the presence of nanofibers. Moreover, modified matrix properties may increase in-plane bending performance. Another reason for the higher flexural performance of nano-interleaved specimens may be related to good interfacial bonding (Figure 4.3.8) between nanofibers and matrix. The bending load was distributed among the matrix and nanofibers acted like an energy absorbing material in the interlaminar region.

The interlaminar shear strength (ILSS), one of the most important parameters in many structural applications, determines the ability of a composite to resist delamination damage. Therefore, the enhancement of ILSS is very important for the long-term safety of fiber reinforced polymer composites. The results of ILSS tests provide valuable insight for the response of composite specimens under Mode-I loading.

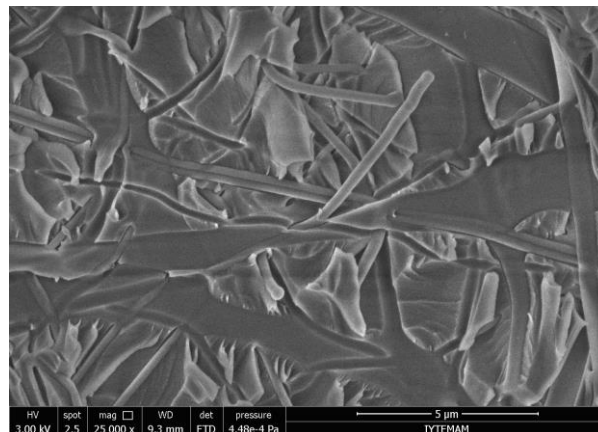


Figure 4.3.8. PVA nanofibers within the epoxy matrix

The ILSS test results of the reference and interleaved composite test specimens were shown in Figure 4.3.9. The value in parenthesis shows the standard deviation of ILSS tests for each group. The ILSS of the reference specimens were determined as 53.3 ± 0.4 MPa. The ILSS of m-AR and m-PA66-17 composite specimens were

determined as 60.76 and 63.01 MPa respectively. This corresponds to about 14% and 18% increase in ILSS values for m-AR and m-PA66-50 composites, respectively. The increase in AWD also led to higher ILSS values (about 21%), *i.e.*, the ILSS of the m-PA66-50 composite specimens was determined as 64.32 MPa. It was obvious that the incorporation of m-AR and m-PA66 nonwovens increased the ILSS of the composites.

On the other hand, the ILSS of nPVA composites was found to be lower than the reference specimens about 4%. However, the addition of nPA66 nanofibers in the interlaminar region increased of ILSS values about 4 and 10% for n-PA66-AWD-0.525 and n-PA66-AWD-1.05, respectively. The reason for increase in ILSS values was the good chemical interaction between the interleaf fibers and epoxy which improves the wetting efficiency. The interleaf fibers provide local resin-rich surfaces which possibly arrest the crack initiation at the interface of the composites. Also, the interleaf materials prevent the stress concentrations and crack initiation within the interlaminar region. As compared to micro-scaled interleaf materials, the PA66 nanofibers led to a more uniform distribution of stresses in the interlaminar region resulted in a lower standard deviation of ILSS data.

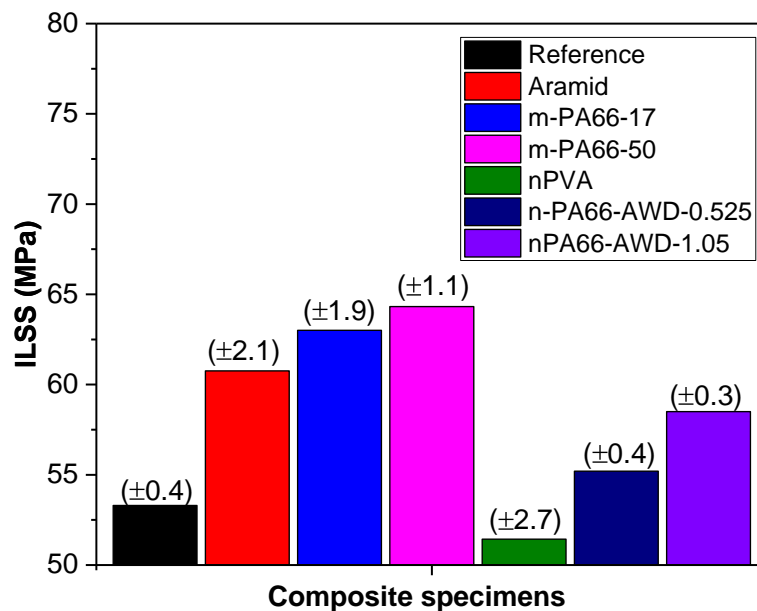


Figure 4.3.9. ILSS values of composite test specimens

The test results showed that the ILSS of existing CF/EP composites could be improved with the incorporation of aramid and PA66 nonwovens composed of micro and nanofibers. Another important observation was that the use of nano-scaled PA66 nonwovens in the interlaminar region led to higher increase in the ILSS values considering the AWD values. For instance, the use of m-PA66 with 50 gsm increased ILSS about 21% whereas the addition of nPA66 with 1.05 gsm increased ILSS about 10%. Therefore it can be said that the nanofiber interleaving technique was more effective in terms of higher ILSS values.

4.4. Effects of interleaf materials on the compressive properties of CF/EP composites

Compressive properties, especially compressive strength, are one of the critical factors that significantly affect the design of fiber-reinforced composites in engineering structures. Generally, compressive strength is lower than tensile strength in a fiber-reinforced composite. Therefore, compressive strength determines the utility of the composite as the weakest link in the engineering structure. It is vital to improve compressive strength without sacrificing other mechanical properties in terms of safer use of composite structures in engineering applications.

Figure 4.4.1 shows the compressive modulus of reference and micro-scaled nonwoven interleaved composite specimens. The compressive modulus of reference composites was determined as 102.1 ± 8.5 GPa. The compressive modulus of m-AR interleaved composite specimens decreased from 102.1 GPa to 84.81 GPa as compared to reference specimens. This corresponds to 17% decrease in compressive modulus values. It was also observed that the compressive modulus decreased with the inclusion of m-PA66 nonwovens in the interlaminar region of composites. Although increasing AWD reduced compressive modulus as in the case of tensile and flexural properties, a moderate reduction about 13% was observed in both values after the addition of the m-PA66 nonwoven veils. Unlike the tensile properties which are highly fiber-dominated, the compressive properties of a fiber reinforced composite depend on many factors such

as matrix modulus and strength, fiber/matrix interfacial bond strength. Therefore, it can be said that the incorporation of m-PA66 nonwoven veils retained the interfacial bond strength of the composites and caused no significant deterioration in compressive properties as compared to the tensile properties. The compressive modulus of nanofiber interleaved composite specimens was also shown in Figure 4.4.1. The addition of nano-scaled nonwovens reduced compressive modulus from 102 to 97.10 GPa for nPVA, 102 to 96.97 GPa for n-PA66-AWD-0.525 and 102 GPa to 95.9 GPa for n-PA66-AWD-0.525 interleaved specimens. The reduction in compressive modulus for nano interleaf materials was much lower than the micro-scaled nonwoven interleaved specimens. This is due to the lower amount nanofiber addition in the interlaminar region as compared to micro nonwovens.

Figure 4.4.2 shows the compressive strength of reference and nonwoven interleaved composite specimens. The compressive strength of reference composites was determined as 764.7 ± 35 MPa. It was found that the compressive strength of the CF/EP composites was decreased with the addition of both m-AR and m-PA66 micro nonwovens. The decrease in compressive strength was about 10 and 14% for m-AR and m-PA66-50 composites, respectively. The decrease in compressive strength values increased with the AWD value for m-PA66-50 composites. The reason was that the addition of significant amount of less-stiff microfibers compared to carbon fibers in the interlaminar region of composites.

On the other hand, in the case of nanofiber interleaved specimens, different behavior was observed. The compressive strength of n-PVA and n-PA66 composites was higher than those of the reference specimens. With the incorporation of PVA and PA66 nanofibers, the compressive strength increased about 4% and 15% respectively. As it is well-known, the longitudinal compressive strength is mainly depends on the matrix material because it provides lateral stiffness and fiber stability to the composite. Due to the presence of nanofibers in the matrix, matrix material could withstand higher compressive stresses in the longitudinal direction which led to significant increase in compressive strength values for nano-interleaved specimens. The PA66 nanofibers were more effective than PVA nanofibers in terms of the enhancement of compressive strength of composites. This is due the their network structure at fiber/matrix interphase,

a better mechanical attachment together with chemical bonding is expected to occur. This may be associated with the improved compressive strength values.

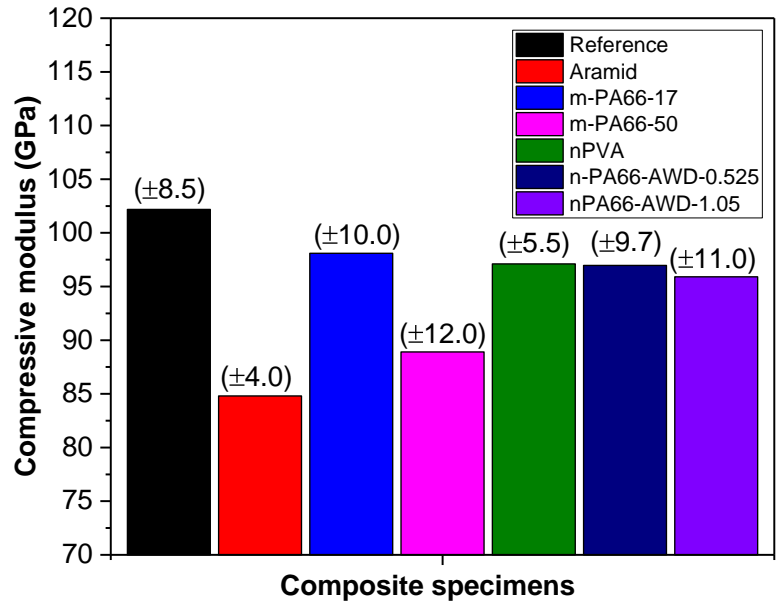


Figure 4.4.1. Compressive modulus of composite test specimens

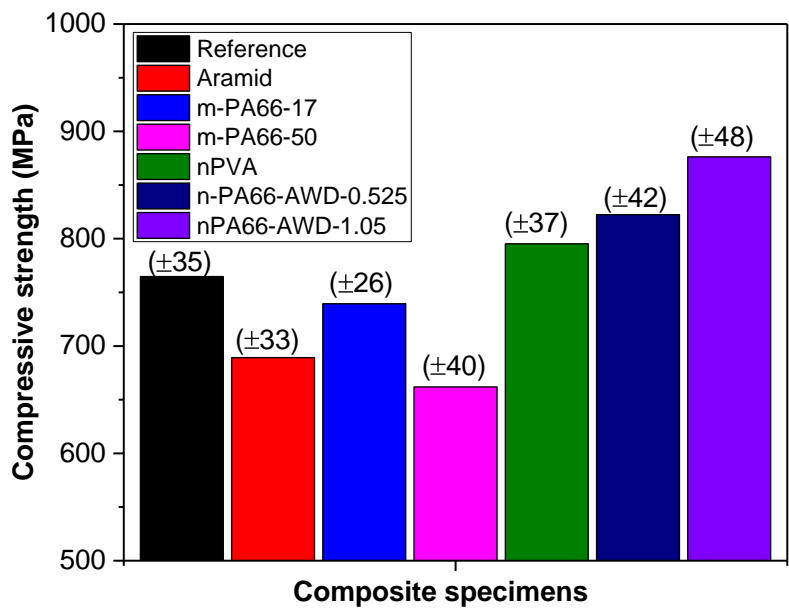


Figure 4.4.2. Compressive strength of composite test specimens

4.5. Effects of interleaf materials on the impact strength of CF/EP composites

The Charpy impact energy of the reference specimens was determined as $81.45 \pm 11.8 \text{ kJ/m}^2$. The SEM images of reference composite specimens were shown in Figure 4.5.1. As can be seen in Figure 4.5.1, reference specimens had a glassy and smooth fractured surface and showed no sign of deformation. These are the main characteristics of poor interfacial bonding strength and impact energy. The Charpy impact energy of the m-AR specimens was determined as $91.89 \pm 9.9 \text{ kJ/m}^2$. The impact energy increased about 13% with the addition of m-AR nonwovens within the reference composites. The deformation of epoxy matrix and torn and pull-out aramid microfibers during the impact loading can be seen in Figure 4.5.2.

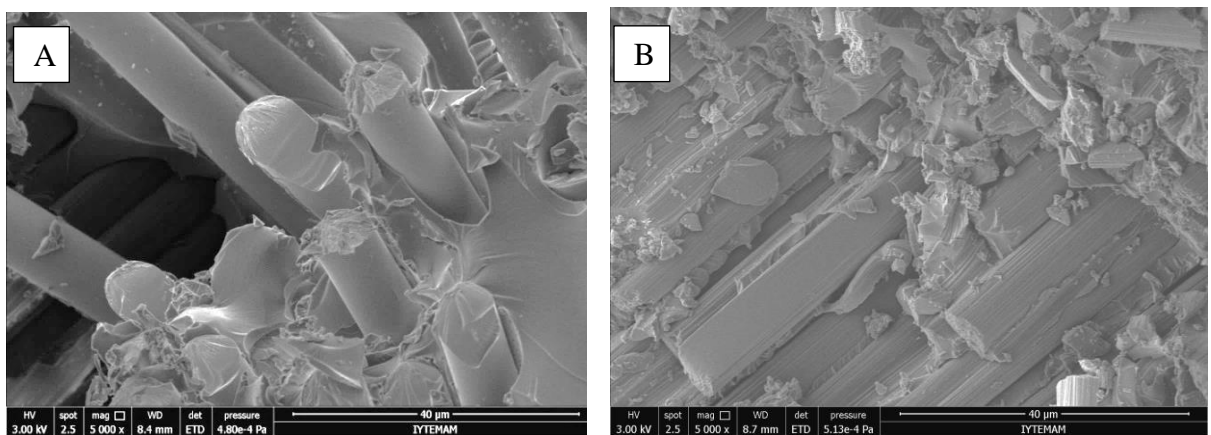


Figure 4.5.1. Fractured surface SEM images of reference Charpy-impact specimens

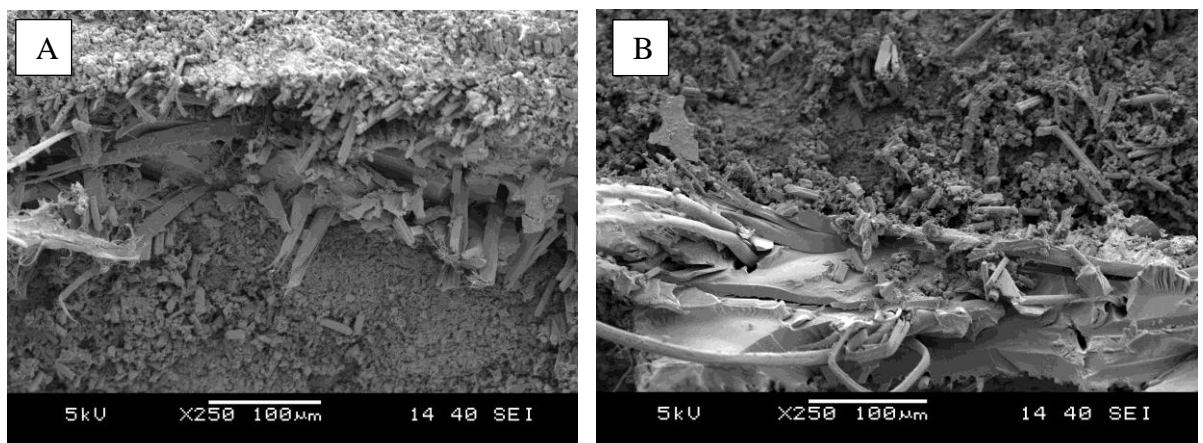


Figure 4.5.2. Fractured surface SEM images of m-AR Charpy-impact specimens

The Charpy impact energy increased about 15% ($93.67 \pm 18 \text{ kJ/m}^2$) by introducing m-PA66-17 nonwovens on the interface area of composite laminates. Although the addition of denser m-PA66 with 50 gsm veils led to higher impact energies, the thickness of the m-PA66-50 composite specimens was higher than reference specimens therefore the impact strength of the composites almost remained unchanged at $82.93 \pm 7.7 \text{ kJ/m}^2$ compared to reference specimens. Figure 4.5.3 shows the SEM images of the m-PA66 composite test specimens. As can be seen in Figure 4.5.3 (a), in the m-PA66 interleaved composite specimens, the epoxy matrix experienced higher deformation and absorbed more impact energy as compared to reference specimens. At the moment of impact, the whole area of PA66 interleaves involved in resisting to the applied load and improved the load-bearing capacity of the composites. The fracture around the mPA66 fibers in Figure 4.5.3 indicates that these fibers participated in the energy absorption and distributed the impact load to the surrounding matrix. The imprints of broken and torn PA66 fibers can be seen in Figure 4.5.3(b).

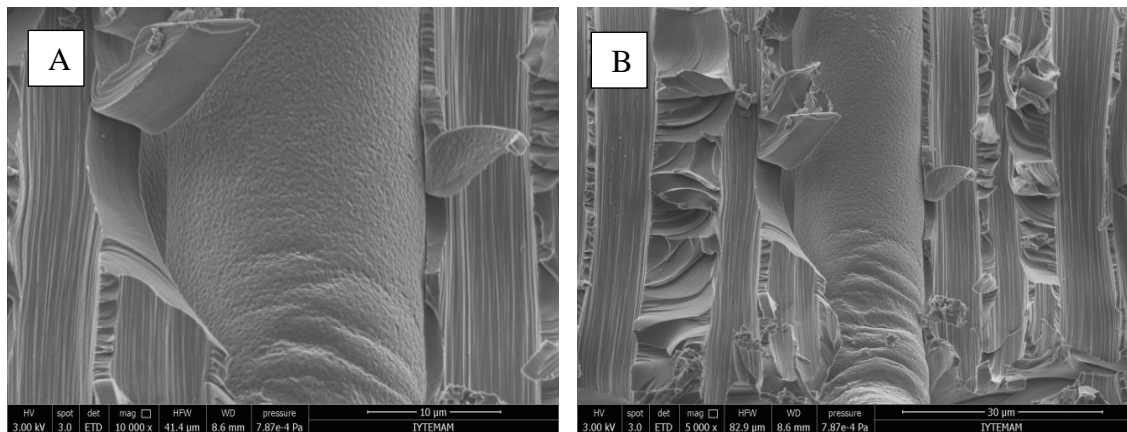


Figure 4.5.3. Fractured surface SEM images of m-PA66 Charpy-impact specimens

For the n-PVA composite specimens, the Charpy impact strength was calculated as $90.41 \pm 5.6 \text{ kJ/m}^2$. This increase in impact energy was about 10% as compared to reference specimens. The Charpy-impact energy values of the nPA66-AWD-0.525 and nPA66-AWD-1.05 composite specimens were determined as $87.19 \pm 15.0 \text{ kJ/m}^2$ and $96.13 \pm 6.9 \text{ kJ/m}^2$ respectively. This corresponds to about 7 and 18% improvement in fracture energy for 0.525 and 1.05 AWD; respectively as compared to those for composites without nanofibers. The improved impact energy can be explained by analyzing the SEM images of the fracture surfaces of PVA and PA66 nanofiber

interleaved specimens. Figure 4.5.4 (a-d) shows the fractured surface SEM images of nPVA and nPA66 Charpy-impact test specimens. As compared to reference specimens, nanofiber interleaved specimens exhibited more complex and irregular fractured surface which indicates higher plastic deformation in the epoxy matrix and impact energy absorption. Also, this improvement is due to the presence of nanofibers in the interlaminar region and their participation in resisting to the crack propagation at the moment of impact, improving load-bearing capacity of the specimens and altering the failure modes during fracture. The nanofibers acted as an energy absorber material in the composite. Moreover, as the in case of n-PA66 composites, when AWD is increased, a relatively higher amount of energy is absorbed which resulted in higher impact resistance. Figure 4.5.5 shows the n-PA66 Charpy-impact specimens before and after impact loading.

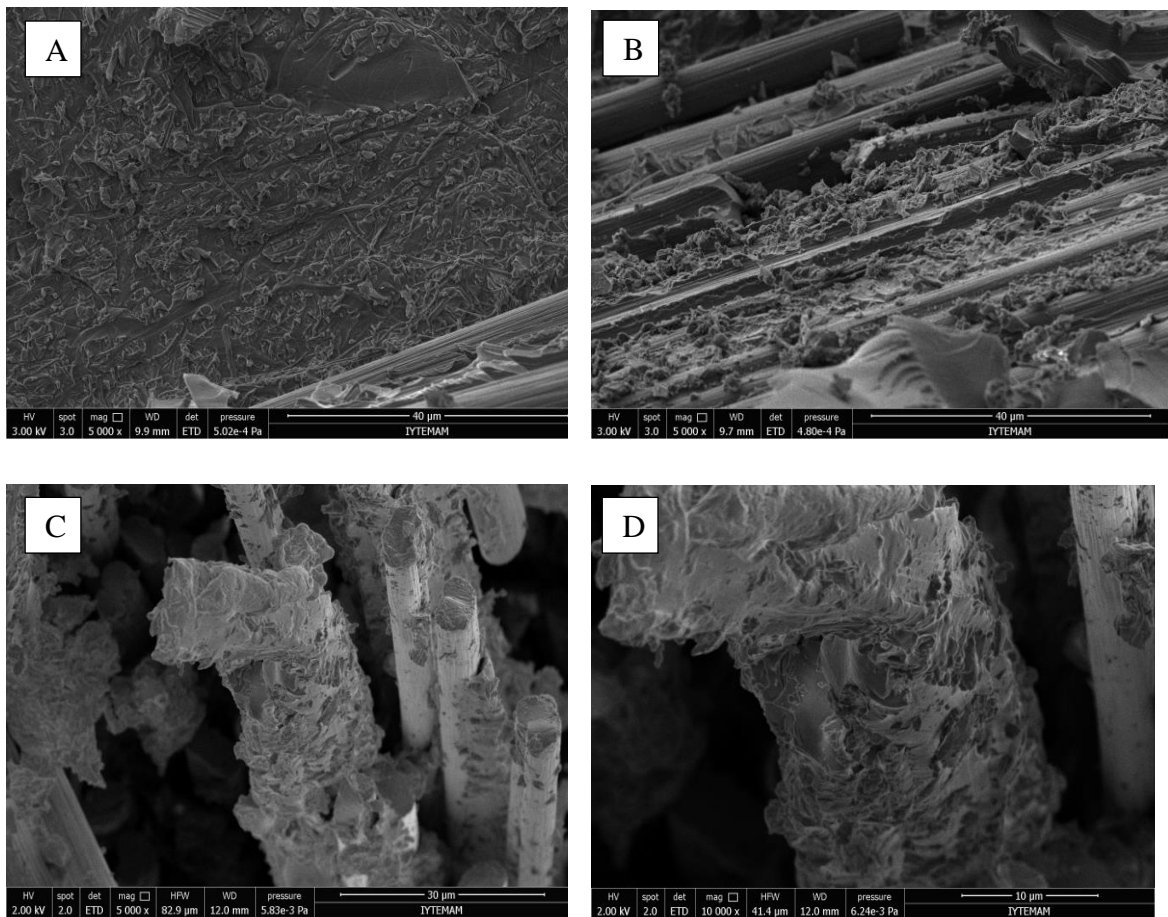


Figure 4.5.4. Fractured surface SEM images of (a-b) nPVA and (c-d) n-PA66 Charpy-impact specimens.

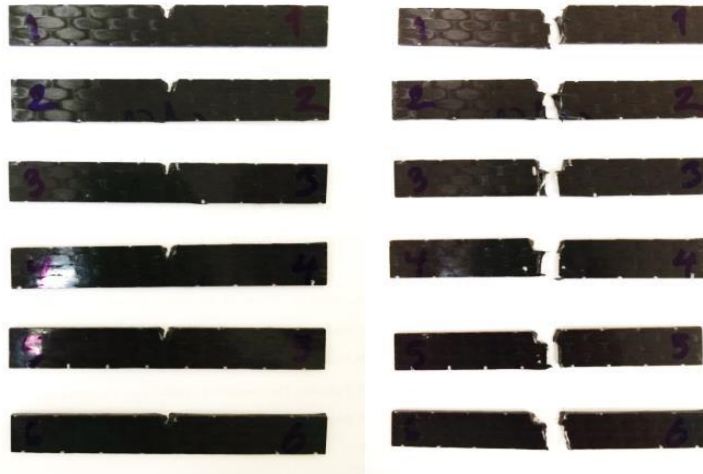


Figure 4.5.5.n-PA66 composite test specimens before and after impact loading.

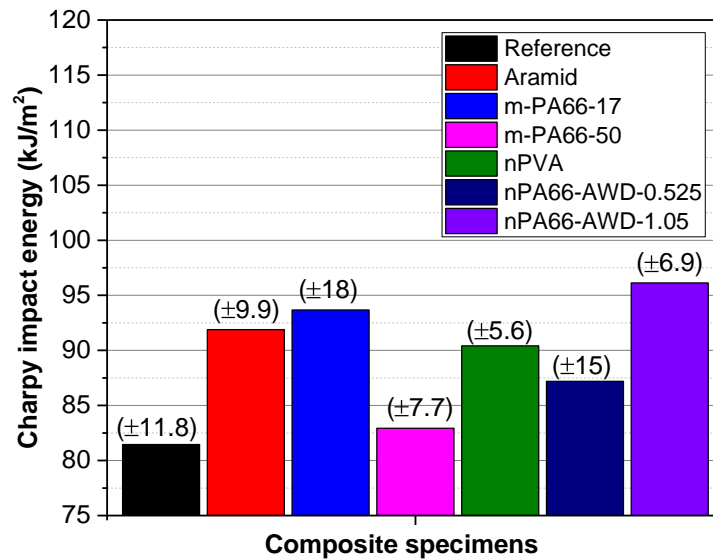


Figure 4.5.6.Charpy impact energy of composite test specimens

Figure 4.5.6 shows the Charpy impact strength of the composite specimens. The Charpy impact tests results showed that the impact energy of existing CF/EP composites could be improved using micro and nano fiber interleaving technique significantly. As compared to the reference specimens, the increase in Charpy impact energy was 5%, 15%, 10% and 18% for m-AR, m-PA66, nPVA, n-PA66 nonwovens, respectively. The plastic deformation of epoxy matrix and the participation of these nonwovens in the absorption of impact loading were the main reasons for improved impact energy. Considering the AWD values of the interleaf materials, the nanofiber interleaving technique was more effective than microfiber interleaving for higher impact resistance.

4.6. Effects of interleaf materials on the Mode-I fracture toughness of CF/EP composites

Figure 4.6.1 shows load-displacement curves of the reference composite specimens under Mode-I loading. The average load (F_{max}) was determined as 14.4 ± 1.0 N. The load-displacement curves of the specimens were jagged-shaped which is one the main characteristics of unidirectional composites. The sharp load drops were observed in the load-displacement curves of the reference specimens. This is an indication of highly unstable crack growth along the interlaminar region in the unidirectional CF/EP composites. The average displacement was calculated as 62.7 ± 8.4 mm. The G_{Ic} values were calculated using Eq. (1) and shown in Figure 4.6.2.

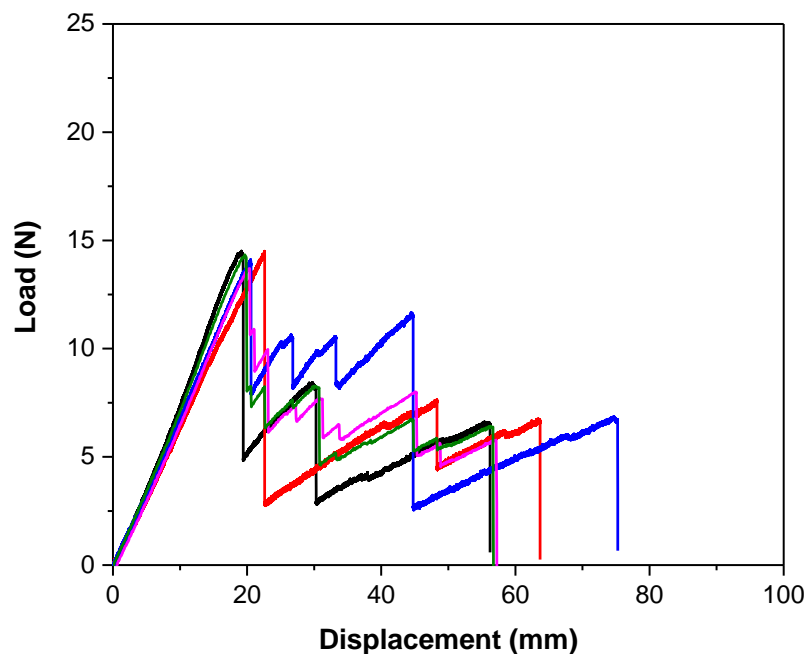


Figure 4.6.1. Load-displacement curves of reference composite specimens under Mode-I loading.

The initiation and propagation values for the reference specimens were determined as 0.20 and 0.24 kJ/m^2 ; respectively. The maximum G_{Ic} value of the reference composites was determined as 0.31 kJ/m^2 . The G_{Ic} values showed an increasing tendency with the delamination length due to carbon fiber bridging effect.

These values were consisted with the reported Mode-I fracture toughness values for unidirectional CF/EP composites (between 0.20-0.30 kJ/m²).

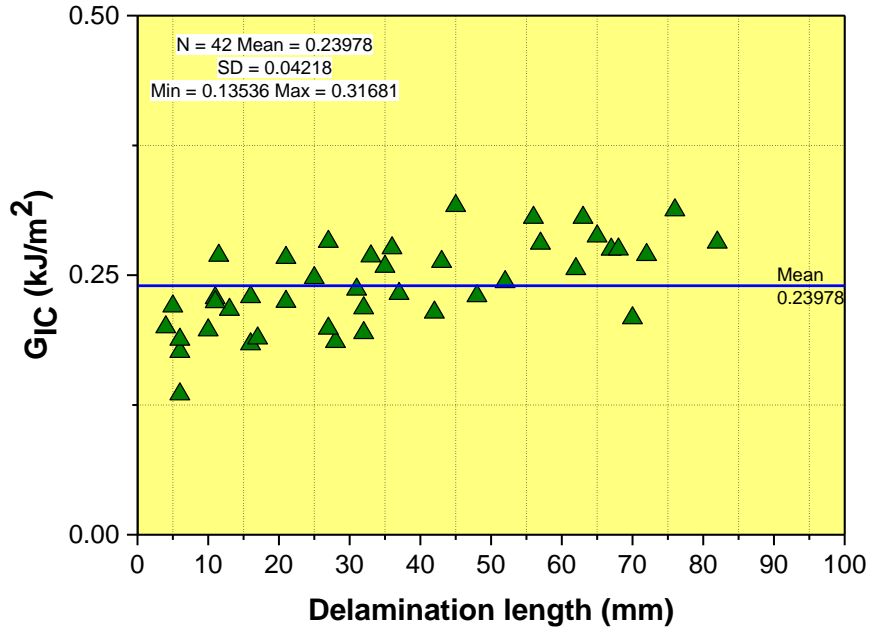


Figure 4.6.2. G_{IC} vs. delamination length of reference composite specimens.

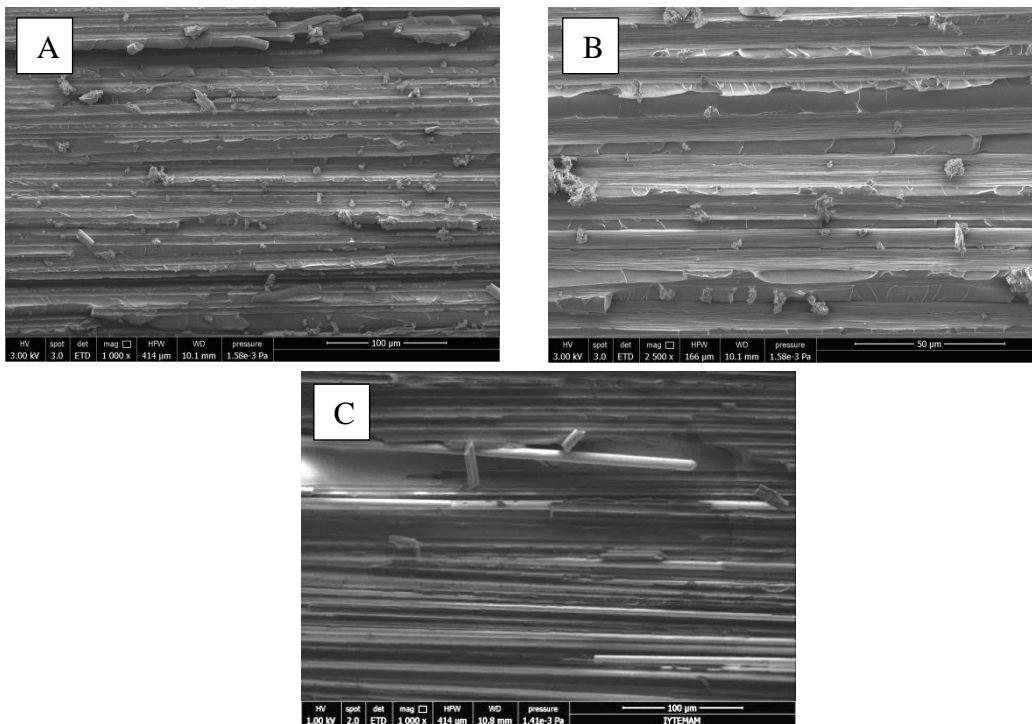


Figure 4.6.3. SEM fracture surface images of the reference specimens

The SEM fracture surface images of the reference specimens with different magnification levels were shown in Figure 4.6.3. The micrographs were taken from the middle of the specimens (away from the initial crack region) for interpreting fracture mechanisms in the reference composite specimens. As seen in Figure 4.6.3 (a-b), the reference specimens exhibited smooth and featureless (indicating brittle failure) failure which is one of the main characteristics of the unidirectional CF/EP composites under Mode-I loading. Debonding of the carbon fibers from the polymer matrix (pulled-out fibers) can be seen in Figure 4.6.3 (c). Mode-I fracture toughness in these composites is controlled by processes such as cohesive fracture of the matrix (fracture process) and fiber bridging as stated by Greenhalgh et al. [2, 3].

In the unidirectional CF/EP composites, the main toughening mechanism is fiber bridging in the wake of the propagating crack tip. This mechanism increases the interlaminar resistance to delamination growth especially after the crack propagates about 10-20 mm away from the crack tip (Figure 4.6.2). However, in this study, a very limited amount of fiber bridging was observed due to the nature of carbon fabric. It was stated in the literature that toughness values for materials that do not exhibit fiber bridging would be more accurate. Also, fiber bridging may lead to misjudging the effects of nanofiber interleaving on the fracture toughness of composites.

Figure 4.6.4 shows load-displacement curves of the m-AR composite specimens under Mode-I loading. The average load values were determined as 17.4 ± 1.01 N for the m-AR composite specimens. As compared to reference specimens, the maximum force values were found to be increased about 21% with the addition of aramid veils in the interlaminar region. Also, the displacement values were higher than the reference specimens. The average displacement of the m-AR composites was calculated as 120.55 ± 11.2 mm. It was observed that both force and displacement values were increased with the addition of aramid nonwoven as compared to reference specimens. Another important observation was that the crack traveled much more slowly in the m-AR composite specimens as compared to reference specimens. This can be associated with small load-drops observed in load-displacement curves which indicate more stable crack propagation during the tests. This behavior was also observed visually in the experiments.

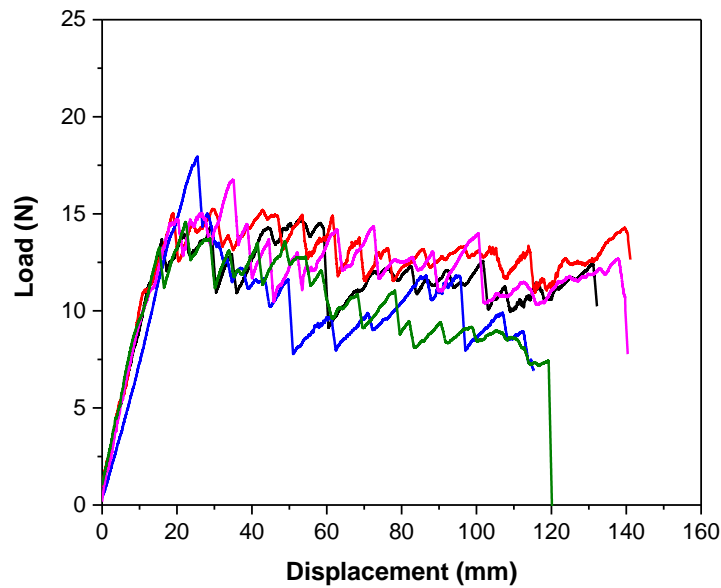


Figure 4.6.4. Load-displacement curves of m-AR composite specimens under Mode-I loading.

Figure 4.6.5 shows the G_{IC} data vs. delamination length graph of the m-AR composites. The initiation and propagation Mode-I fracture toughness values were determined as 0.201 and 0.348 kJ/m^2 ; respectively. It can be said that aramid nonwovens did not have a significant effect on the initiation Mode-I fracture toughness. The initiation Mode-I fracture toughness remained unchanged with addition of aramid veils. The maximum force and corresponding displacement values were not significantly changed until the first crack became visible. However, as the crack propagates, the effects of aramid fiber bridging became more noticeable. The G_{IC} values started to increase with the increase of delamination length when the crack propagated about 10 mm from the crack tip. As compared to reference specimens, the propagation Mode-I fracture toughness increased from 0.240 to 0.348 kJ/m^2 . This corresponds to almost 45% increase in Mode-I fracture toughness values. The maximum G_{IC} value of the m-AR composites was calculated as 0.577 kJ/m^2 . This value was 87% higher than the reference composites. These results clearly show that the Mode-I fracture toughness properties could be improved by interleaving the aramid nonwovens within the interlaminar region of composites. Figure 4.6.6 shows SEM images of fractured m-AR composite specimens under Mode-I loading.

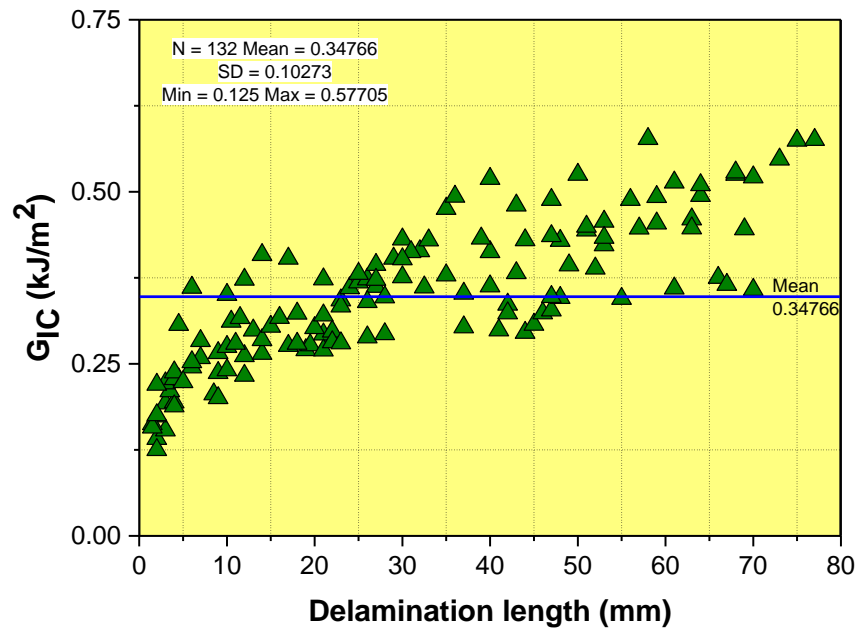


Figure 4.6.5. G_{IC} vs. delamination length of m-AR composite specimens.

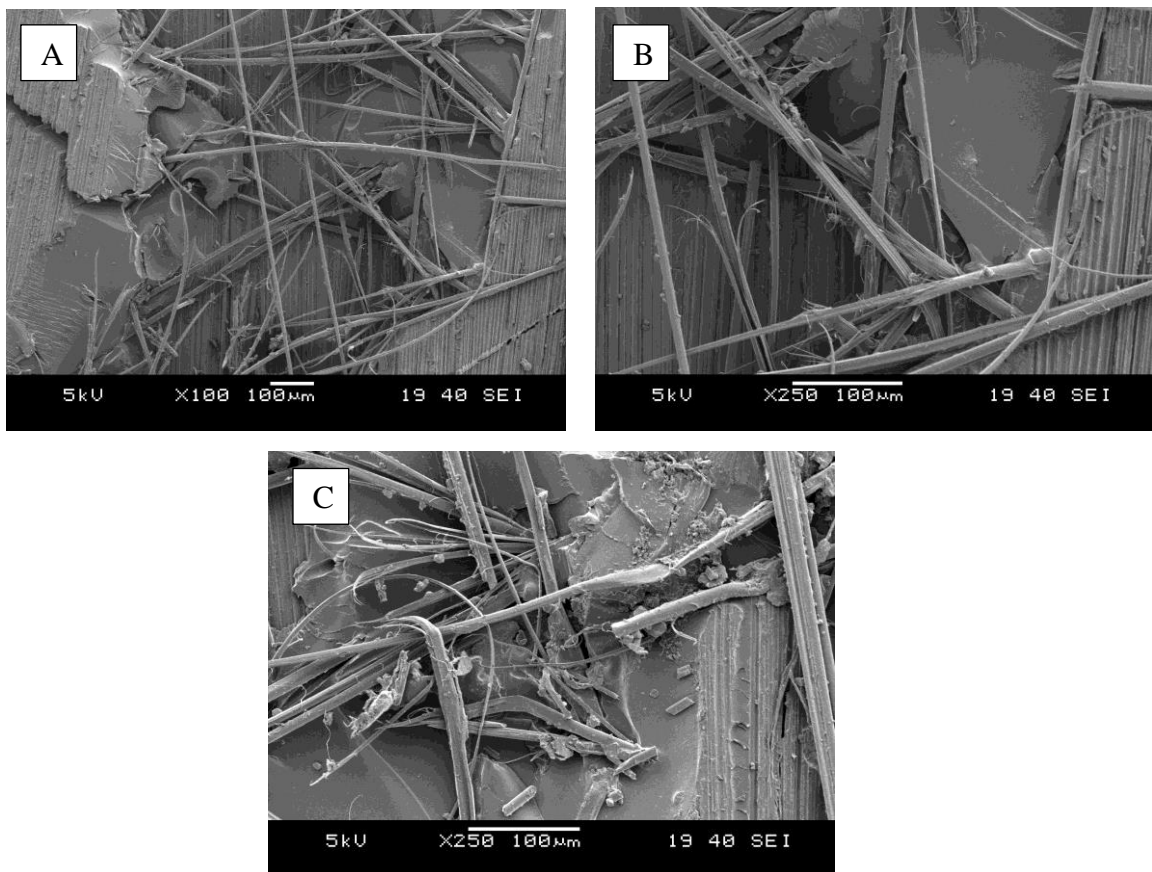


Figure 4.6.6. SEM images of fractured m-AR composite specimens under Mode-I loading.

Figure 4.6.7 and Figure 4.6.8 show the load-displacement curves of the m-PA66-17 and m-PA66-50 composite specimens under Mode-I loading. The load-displacement response of the m-PA66-17 composites was similar to those of the reference composite specimens. The zig-zagged shape response in load-displacement curves were obtained for the m-PA66-17 composites. However, the addition of m-PA66-50 nonwovens altered the load-displacement response of the composite specimens from zig-zagged to bow-shaped which generally observed in the woven composites (stable crack propagation). Another important observation during the Mode-I tests was that the load values of m-PA66-50 composites decreased significantly in some specimens after the crack propagated about 40-50 mm measured from the crack tip. The reason for this decrease was that the crack encountered relatively weak CF/EP interface and jumped into this weak interface. Then it continued to propagate in this relatively weak interface. Comparing with the m-PA66-17 composites, much higher amount of energy was absorbed in the crack plane and the energy was released in the weak carbon fiber/epoxy interface of the composite (Figure 4.6.9).

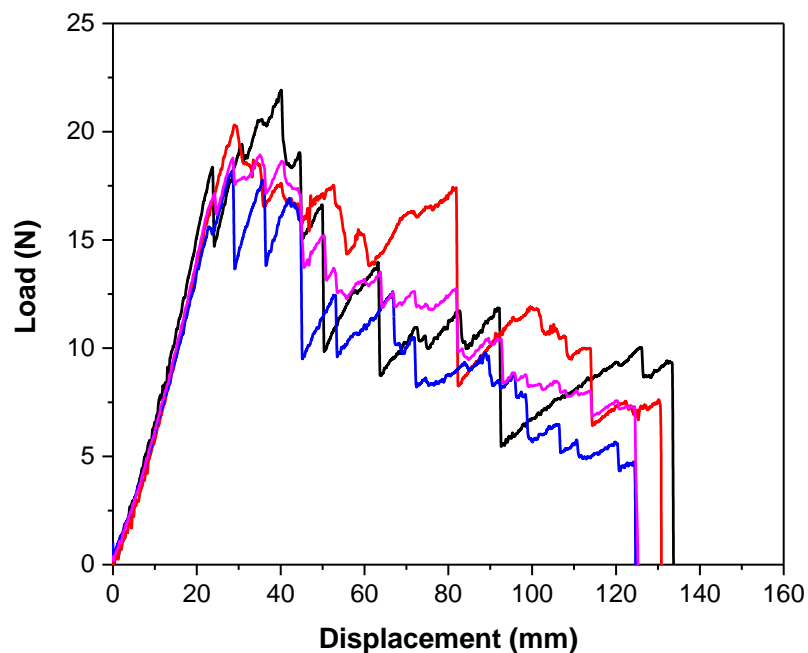


Figure 4.6.7. Load-displacement curves of m-PA66-17 composite specimens under Mode-I loading.

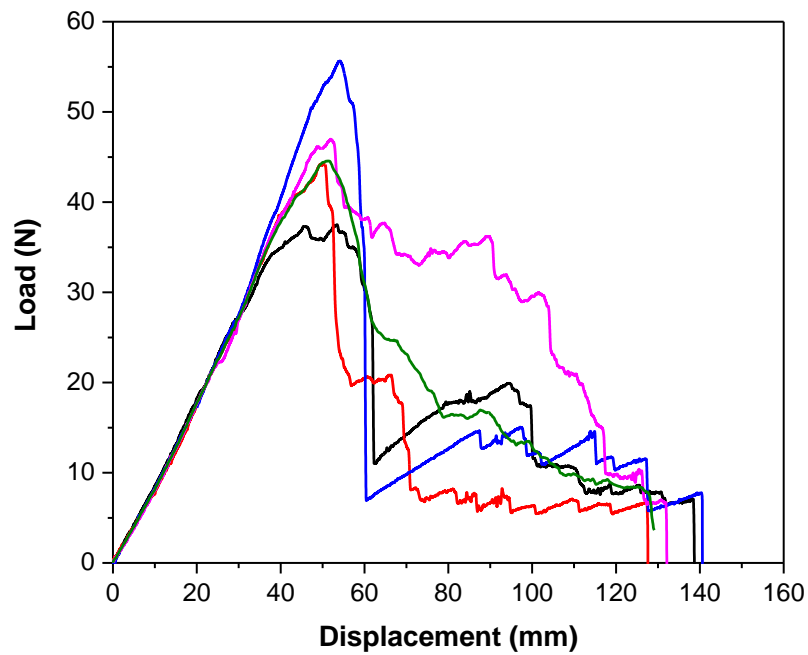


Figure 4.6.8. Load-displacement curves of m-PA66-50 composite specimens under Mode-I loading.

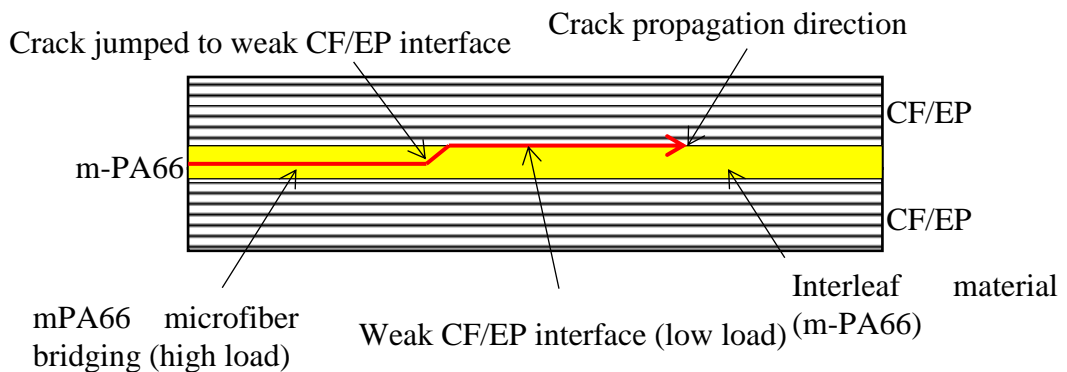


Figure 4.6.9. Schematic representation of the crack propagation in m-PA66 composite specimens

The average load (F_{max}) for m-PA66-17 composites was calculated as 23.6 ± 2.4 N. This corresponds to a 64% increase in the crack opening force values as compared to reference specimens. Also, the average displacement value was 128.4 ± 4.6 mm. The displacement values increased about 104.7% with the incorporation of m-PA66-17 interleaf material in the interlaminar region of the composites. For m-PA66-50

composite specimens, the average load (F_{\max}) was calculated as 48.2 ± 6.85 N. The average load value increased almost 2.5 times as compared to reference specimens. Also, the displacement values increased from 62.7 ± 8.4 to 135.5 ± 5.7 mm (about 116%).

Figure 4.6.10 shows the G_{IC} data vs. delamination length graphs of the m-PA66-17 and m-PA66-50 composite specimens. G_{IC} of the m-PA66-17 composite specimens was in the range between 0.340 and 1.102 kJ/m². Increasing AWD from 17 to 50 gsm led to much higher Mode-I fracture toughness values so it reached to its maximum value between 1.173 and 2.780 kJ/m². This corresponds to about 248 and 778% improvement of the maximum G_{IC} values Mode-I fracture toughness for m-PA66-17 and m-PA66-50 composite specimens, respectively, as compared to those for reference specimens. This can be associated with the excessive PA66 fiber bridging mechanism within the interlaminar region which will be discussed in more detail below. For the m-PA66-17 composites, the initiation and propagation Mode-I fracture toughness values were determined as 0.342 ± 0.017 and 0.643 ± 0.14 kJ/m²; respectively. This corresponds to about 71 and 168% improvement of those initiation and propagation Mode-I fracture toughness values, respectively, as compared to those for reference specimens. For the m-PA66-50 composites, the initiation and propagation fracture toughness values were found to be 0.831 ± 0.023 and 1.940 ± 0.38 kJ/m² which corresponds to as high as 316 and 708% improvement as compared to the reference specimens.

Figure 4.6.11 (a-b) shows the excessive m-PA66 fiber bridging observed during the DCB tests. Due to the good adherence between epoxy and m-PA66 fibers, m-PA66 nonwovens absorbed high amount of strain energy by bridging the crack opening and tearing which contribute to the improvement of delamination resistance. Figure 4.6.11 (c-d) shows the fractured surfaces of m-PA66 interleaved composite specimens. As compared to reference specimens, m-PA66 composite specimens exhibit a different type of failure surface. A high amount of torn m-PA66 fibers and minimal matrix fracture was observed in the m-PA66 interleaved composite specimens. Also, the pulled-out m-PA66 fibers from the matrix and the imprints of m-PA66 fibers on the other side of the delamination plane can be seen in Figure 4.6.11(c-d). The SEM images and the observation during the DCB tests revealed that the main toughening mechanism was the m-PA66 fiber bridging which led to much higher interlaminar fracture toughness and

more stable crack propagation in the m-PA66 nonwoven interleaved composite specimens. Figure 4.6.12 shows the photograph of DCB surfaces of a m-PA66 composites after Mode-I testing. The PA66 fiber imprints (white region) can be seen on both side of the DCB surfaces.

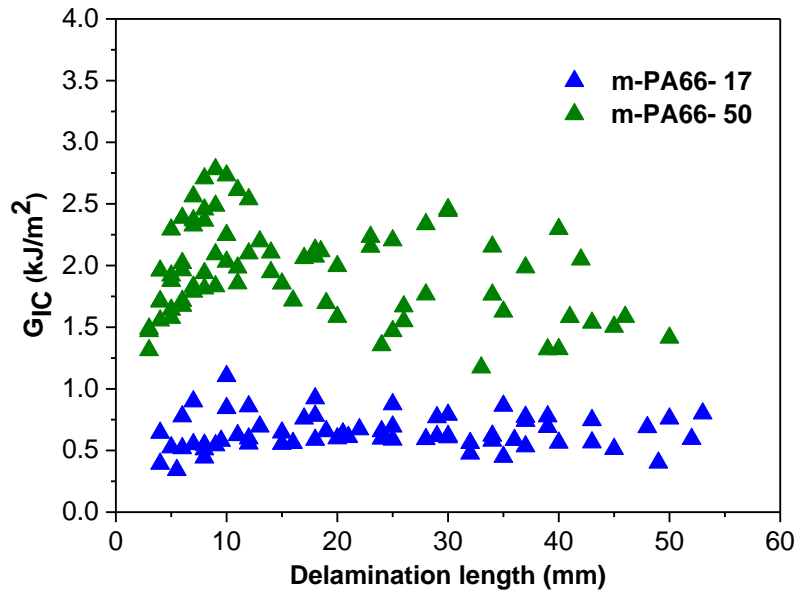


Figure 4.6.10. G_{IC} vs. delamination length of m-PA66 composite specimens.

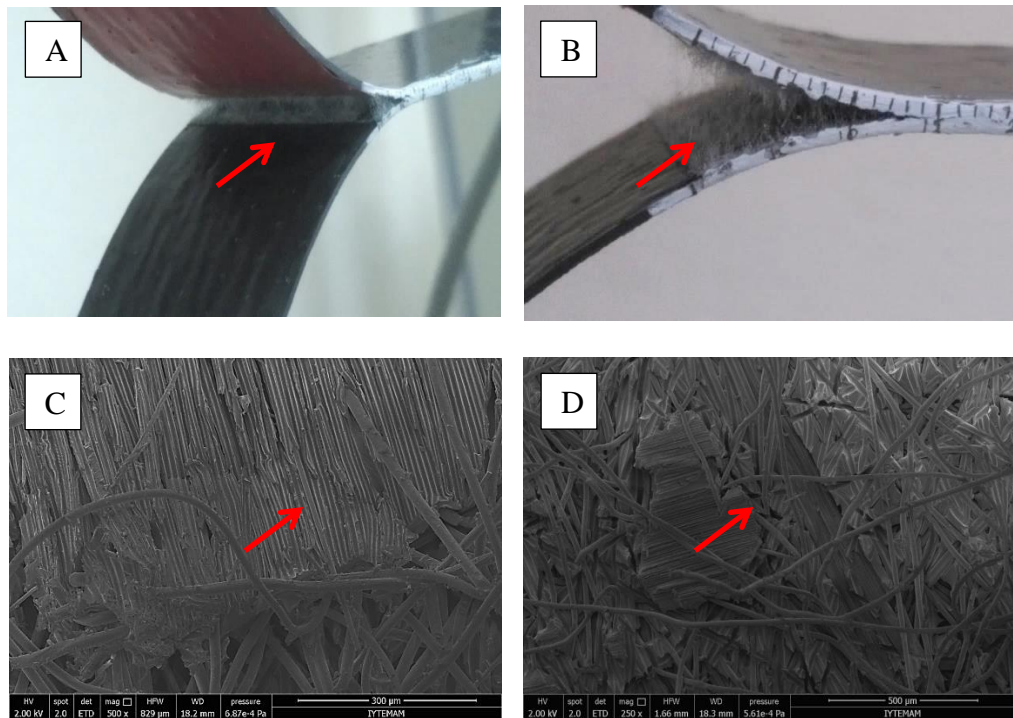


Figure 4.6.11. (a-b) Photographs of m-PA66 composite specimens under Mode-I loading and (c-d) SEM images of fractured surfaces of m-PA66 composite specimens.

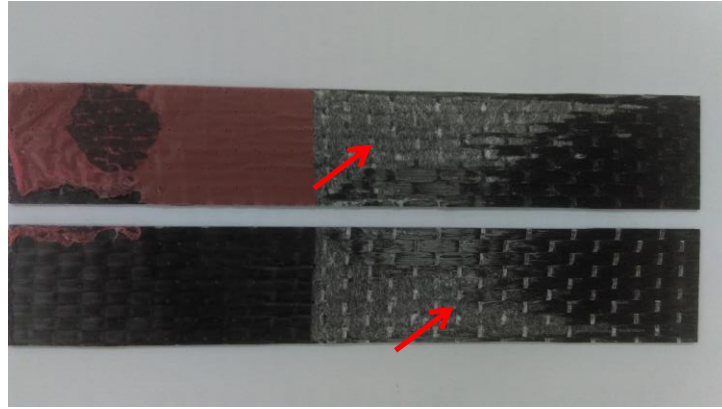


Figure 4.6.12. Photograph of the DCB surfaces of fractured m-PA66 composite.

Figure 4.6.13 show load-displacement curves of the nPVA composite specimens under Mode-I loading. The average load (F_{max}) was determined as 12.3 ± 0.9 N. It was observed that PVA nanofibers caused a reduction about 14.6% in average load values as compared to reference specimens. On the other hand, more gradual load drops were observed unlike the reference specimens. It can be said that the crack propagated in a stable manner due to the PVA nanofibers. The average displacement was calculated as 80.1 ± 3.9 mm. This value was 27% higher than the average displacement of the reference specimens. The G_{Ic} values were calculated using the Equation (1) and shown reference specimens. Although, the displacement values increased, it was noticed that the force values to open the crack decreased. For the nPVA composites, the initiation and propagation Mode-I fracture toughness values were determined as 0.168 ± 0.022 and 0.201 ± 0.02 kJ/m²; respectively. The results showed that the initiation and propagation Mode-I fracture toughness decreased about 17% with the incorporation of nPVA nanofibers in the interlaminar region. The maximum Mode-I fracture toughness value was calculated as 0.244 kJ/m². The decrease in Mode-I fracture toughness can be associated with the reduced the amount of epoxy ahead of the crack-tip. The PVA nanofibers were not able to resist crack propagation via fiber bridging. As can be seen in Figure 4.6.14, the G_{Ic} values did not show an increasing tendency with the delamination length. Figure 4.6.15 shows the SEM images of nPVA composites. The nPVA composites exhibited more complex and rough surfaces as compared to reference specimens Figure 4.6.14(a). The PVA nanofibers within the epoxy matrix can be seen in Figure 4.6.14(b). Additionally large amount of PVA nanofibers were remained in the

epoxy matrix instead of participating fiber bridging which would lead to significant improvement in Mode-I fracture toughness.

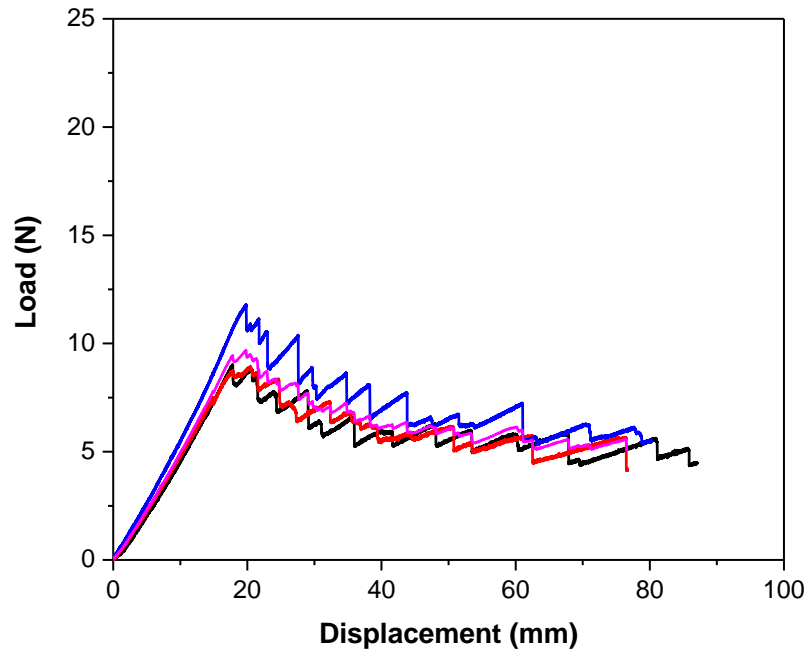


Figure 4.6.13. Load-displacement curves of nPVA composite specimens under Mode-I loading.

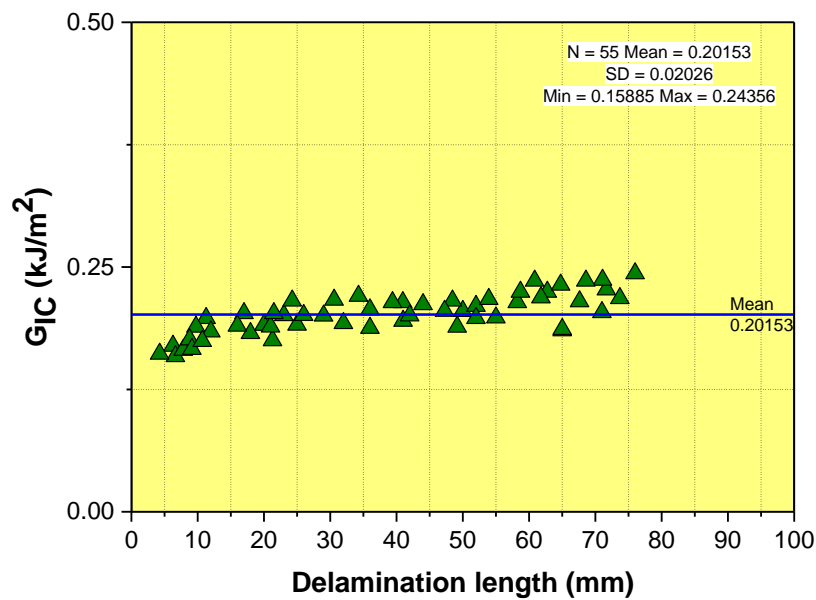


Figure 4.6.14. G_{IC} vs. delamination length of nPVA composite specimens.

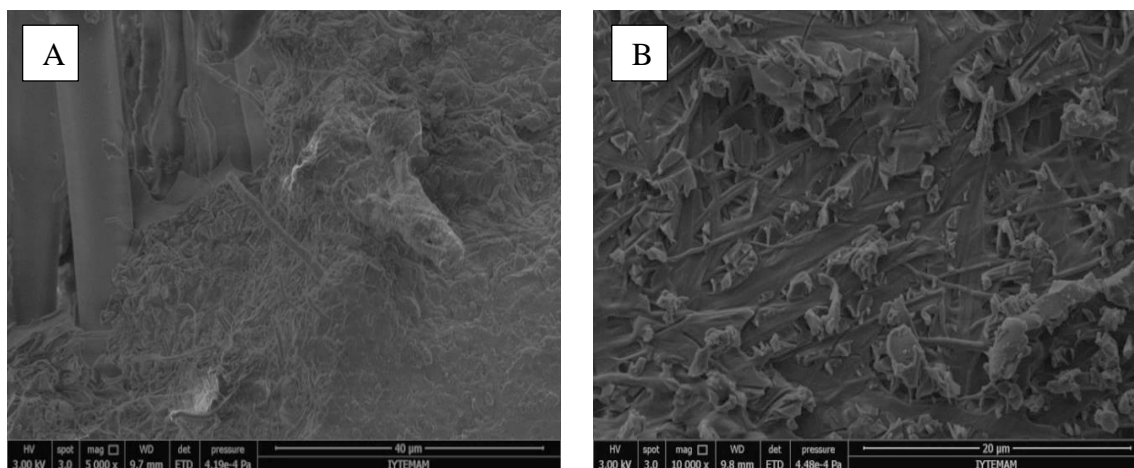


Figure 4.6.15. SEM images of fractured surfaces of nPVA composite specimens.

Figure 4.6.16 and Figure 4.6.18 show load-displacement curves of the nPA66-AWD-0.525 and nPA66-AWD-1.05 composite specimens under Mode-I loading, respectively. The average maximum load (F_{max}) values were determined as 16.42 ± 0.21 N and 21.0 ± 1.09 N and for the nPA66-AWD-0.525 and nPA66-AWD-1.05 composite specimens, respectively. As compared to reference specimens, the average maximum load values were increased from 14.5 N to 16.4 N for the nPA66-AWD-0.525 and from 14.4 N to 21.0 N. This corresponds to 13 and 45 % increase in the load values for the nPA66-AWD-0.525 and nPA66-AWD-1.05 respectively. Also, it was noteworthy that the maximum load values were found to be increased with the increase of nanofiber AWD values. The displacement values of the nPA66 specimens were higher than the reference specimens. The increase in both force and displacement values is an indication of higher delamination resistance as compared to reference specimens. The load-displacement curves of the specimens were jag-shaped as in the case of reference specimens. However, nPA66 specimens experienced many small-load drops during the crack propagation. The reason for that was the crack in the nPA66 modified specimens traveled much more slowly in the interlaminar region as compared to the reference specimens. Therefore, it can be said that the addition of PA66 nanofibers in the interlaminar region led to more stable crack propagation than the reference specimens.

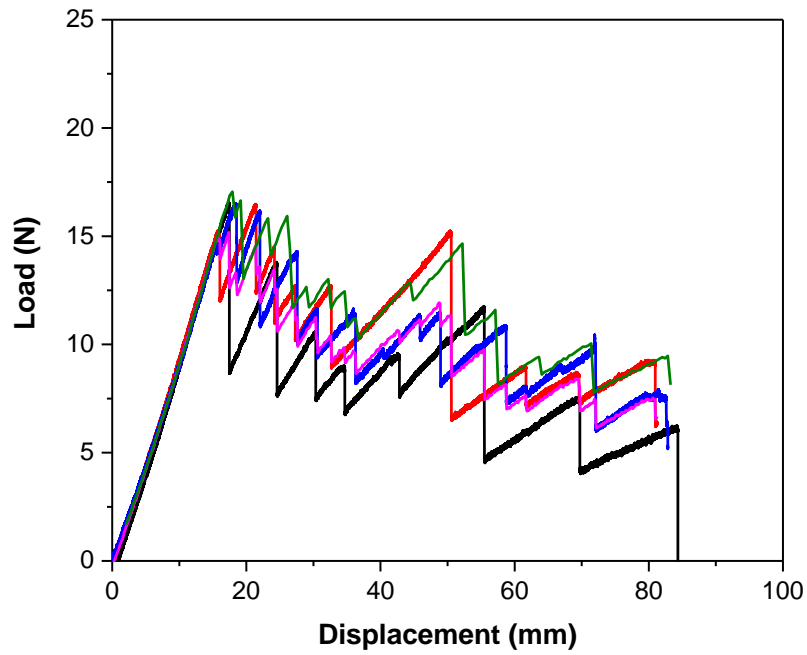


Figure 4.6.16. Load-displacement curves of nPA66-AWD-0.525 composite specimens under Mode-I loading.

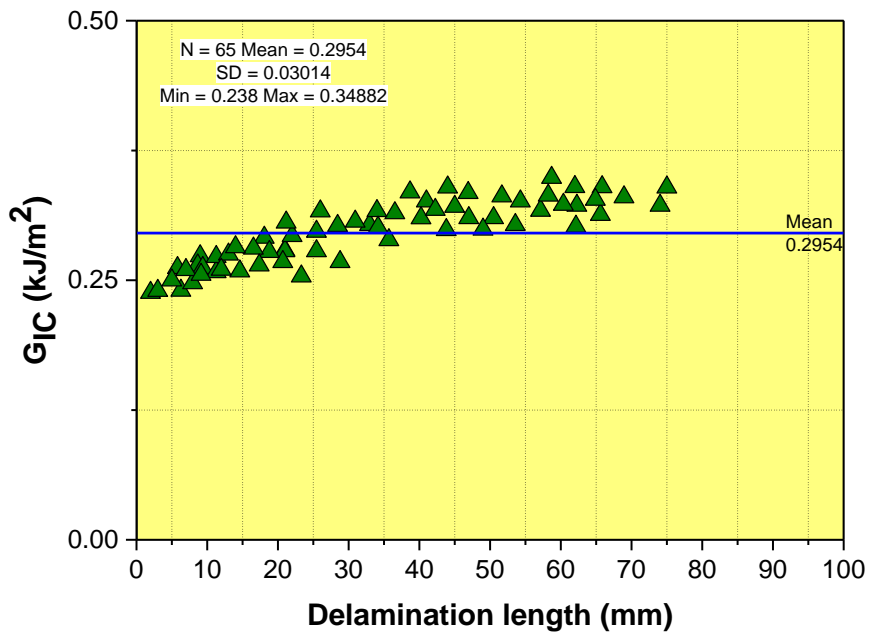


Figure 4.6.17. G_{IC} vs. delamination length of nPA66-AWD-0.525 composite specimens.

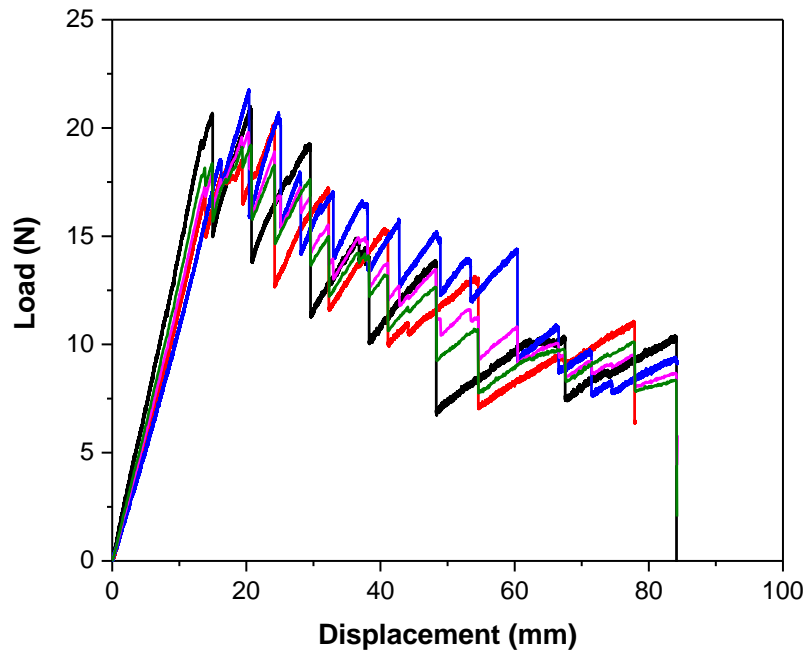


Figure 4.6.18. Load-displacement curves of nPA66-AWD-1.05 composite specimens under Mode-I loading.

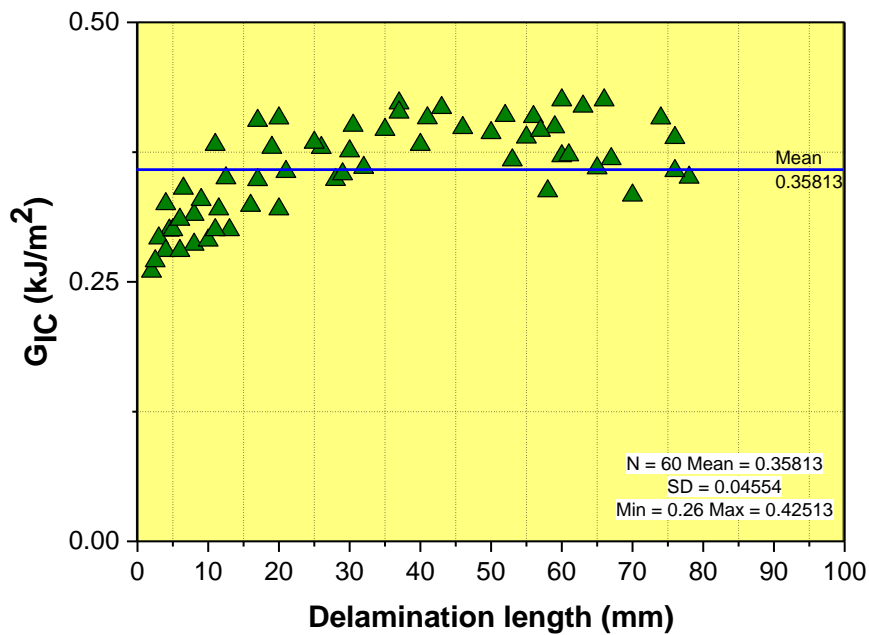


Figure 4.6.19. G_{IC} vs. delamination length of nPA66-AWD-1.05 composite specimens.

Figure 4.6.17 and Figure 4.6.19 show G_{IC} data vs. delamination length graphs of the nPA66-AWD-0.525 and nPA66-AWD-1.05 composite specimens, respectively. For

the composites with 0.525 g/m² PA 6/6 nanofiber coating, the initiation and propagation Mode-I fracture toughness values were determined as 0.255 and 0.296 kJ/m²; respectively. This corresponds to about 28 and 24% improvement of those values, respectively, as compared to those for reference specimens. For the composites containing nanofibers with AWD of 1.05 g/m², the initiation and propagation values were found to be 0.298 and 0.358 kJ/m² which corresponds to 50 and 51% improvement in Mode-I fracture toughness. The maximum G_{IC} values for the nPA66-AWD-0.525 and nPA66-AWD-1.05 composite specimens were determined as 0.348 and 0.425 kJ/m² respectively. The increase in the maximum G_{IC} values was 13 and 37% for the nPA66-AWD-0.525 and nPA66-AWD-1.05 composite specimens, respectively. These results clearly show that due to the presence of nanofibers within the composites, the Mode-I fracture toughness properties are improved significantly. This can be associated with the enhanced bridging mechanism promoted by PA66 nanofibers within the interlaminar region.

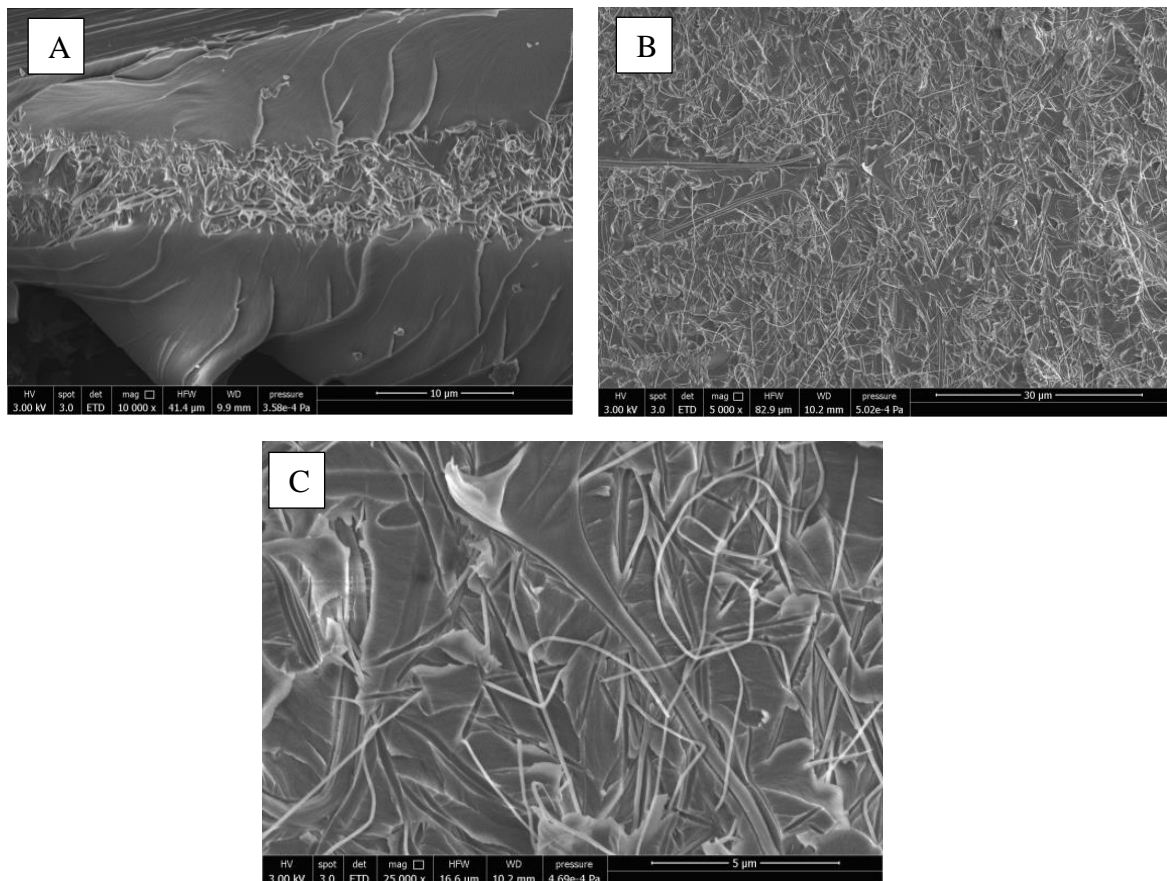


Figure 4.6.20. SEM images of Mode-I fractured surfaces of nPA66 interleaved composite specimens.

Figure 4.6.20 shows SEM images of Mode-I fractured surfaces of nPA66 interleaved composite specimens. Compared to reference specimens, the nPA66 fracture surfaces exhibits a combination of smooth and deformed regions (deformation of the matrix material and PA 66 nanofibers) as seen in Figure 4.6.20(a).

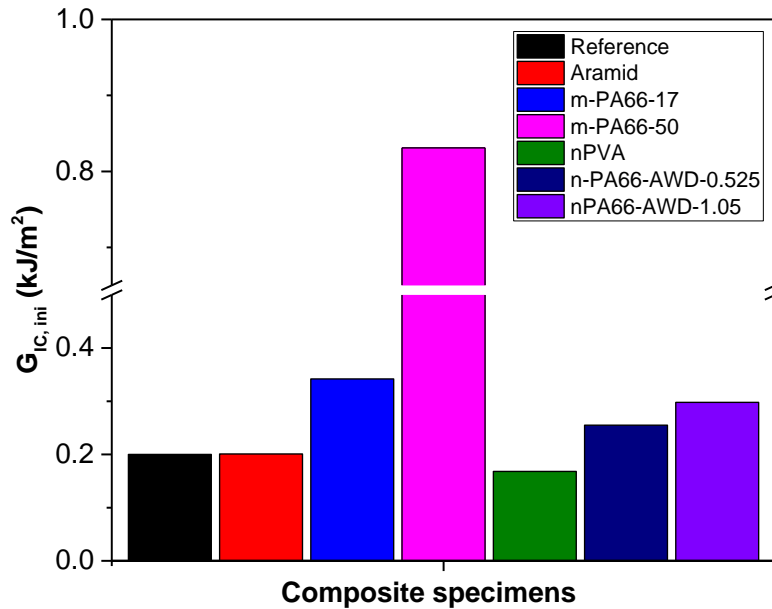


Figure 4.6.21. Initiation Mode-I fracture toughness (G_{IC}) of composite test specimens

Figure 4.6.20(b) shows the deformed PA 66 nanofibers within the matrix. PA 66 nanofiber imprints within the matrix can be also seen in this figure. Deformed PA66 nanofiber can be seen in Figure 4.6.20(c). During the tests, thousands of thousands PA66 nanofibers resisted to crack propagation which resulted in improved Mode I fracture toughness. The SEM images support the hypothesis of more stable crack propagation in the nPA66 interleaved composites. The main toughening mechanisms were crack deflection and fiber bridging in the interlaminar region observed in the nPA66 interleaved specimens. The fiber bridging kept the carbon plies together and led to a significant improvement in the crack opening forces. Plastic deformation of the PA66 nanofibers also improved the energy absorbing capacity of the composites. When the crack encounters with an obstacle such as PA66 nanofibers in this case, significant amount of energy is necessary to deform PA66 nanofibers. The improved matrix property due to good chemical interaction between the PA66 nanofibers and epoxy

matrix was the other reason for the improved delamination resistance. Figure 4.6.21 and Figure 4.6.22 summarizes the initiation and propagation Mode-I fracture toughness of reference and interleaved composite specimens.

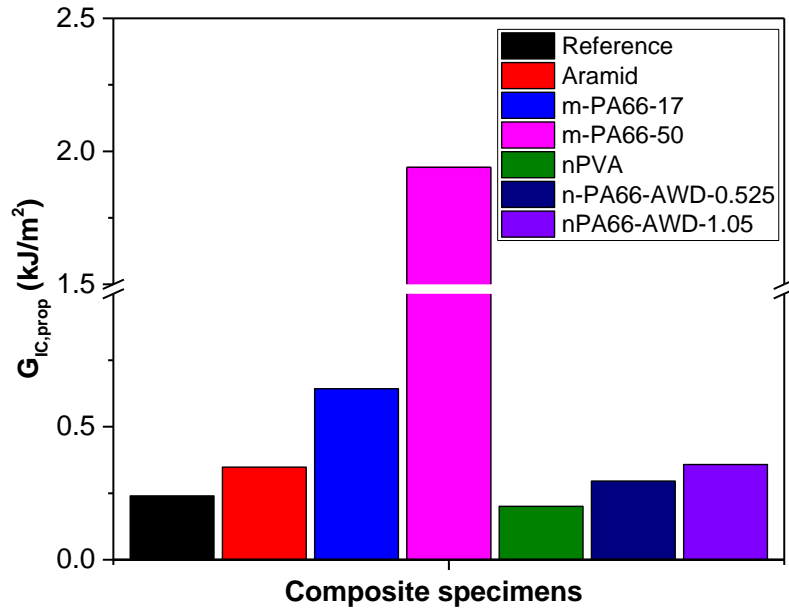


Figure 4.6.22. Propagation Mode-I fracture toughness (G_{IC}) of composite test specimens

4.7. Effects of interleaf materials on thermomechanical behavior of CF/EP composites

The glass transition temperature (T_g) of composite specimens were presented in Table 4.2. The T_g of reference composites was determined as 95.55°C. The T_g of the micro and nano modified composite specimens was determined as in the range of 95-96°C. Therefore, it can be concluded that the micro and nano interleaf materials retained the glass transition of the composites and caused no significant change in the T_g values. Figure 4.7.1 shows storage and loss modulus of the reference and interleaved composite specimens. The storage modulus is the elastic response of the material and the loss modulus measures the energy dissipated as heat. The results showed that the storage modulus decreased with the incorporation of micro-scaled nonwovens in the

interlaminar region of composites. The decrease in storage modulus was about 21, 26 and 31% for m-AR, m-PA66-17 and m-PA66-50 composite specimens respectively. This is due to fact that the interleaf material gives more flexibility resulting in the low stiffness and low storage modulus. These results were consistent with the results of three-point bending test results. The micro-scaled interleaf materials reduced the flexural modulus and strength values as shown in Section 4.3.

Table 4.2. Glass transition temperature (T_g) of composite specimens

Code	Glass transition temperature (T_g , °C)
Reference	95.55
m-AR	96.10
m-PA17	96.37
m-PA50	96.25
nPVA	95.20
nPA66-AWD-0.525	96.16
nPA66-AWD-1.05	95.93

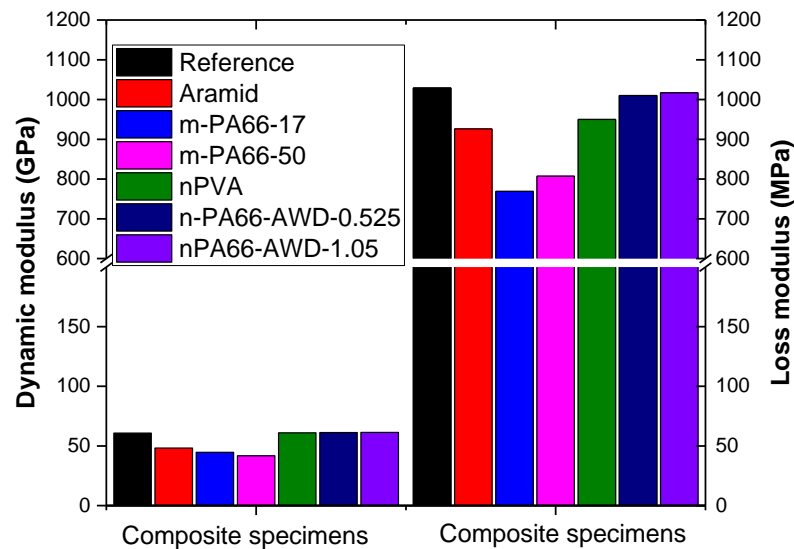


Figure 4.7.1. Storage and loss modulus of composite test specimens

Loss modulus represents the response of viscoelastic behavior of a material. It represents composite's ability to disperse mechanical energy via intermolecular motions. It was observed that the loss modulus of the composites decreased with the incorporation of micro-scaled nonwovens in the interlaminar region of composites. The decrease in loss modulus was about 10, 25 and 22% for m-AR, m-PA66-17 and m-PA66-50 composite specimens respectively. The addition of microfibers into interlaminar region of composite increases the flexibility and decreases the viscosity. Therefore, less energy is necessary to overcome the frictional forces between molecular chains as to decrease mechanical loss.

On the other hand, as compared to micro-scaled nonwoven interleaved composites, the nanofibers had a positive effect on the storage and loss modulus of the composites. In other words, the ability to store energy and impact absorption of composites increased with the incorporation of nanofibers in the interlaminar region of composite. The increase in the storage modulus can be associated with the efficient stress transfer at the interface between nanofibers and epoxy matrix. These results were also consistent with the results of three-point bending test results obtained for nanofiber interleaved specimens.

Figure 4.7.2 shows $\tan\delta$ (peak) values of the reference and interleaved composite specimens. $\tan\delta$ (peak) represents the mechanical damping efficiency of a material. The $\tan\delta$ (peak) values were determined as 0.492, 0.6477, 0.5676 and 0.5474 for reference, m-AR, m-PA66-17 and m-PA55-50 composites, respectively whereas the $\tan\delta$ (peak) values were determined as 0.504, 0.5249, 0.5435 for nPVA, n-PA66-ADW-0.525 and n-PA66-ADW-1.05 composites, respectively. Therefore, it can be concluded that the mechanical damping efficiency increased with the addition of interleaf materials in the interlaminar region of composites. Moreover, the nanofiber interleaved specimens were more effective in terms of higher damping ability considering the AWD values.

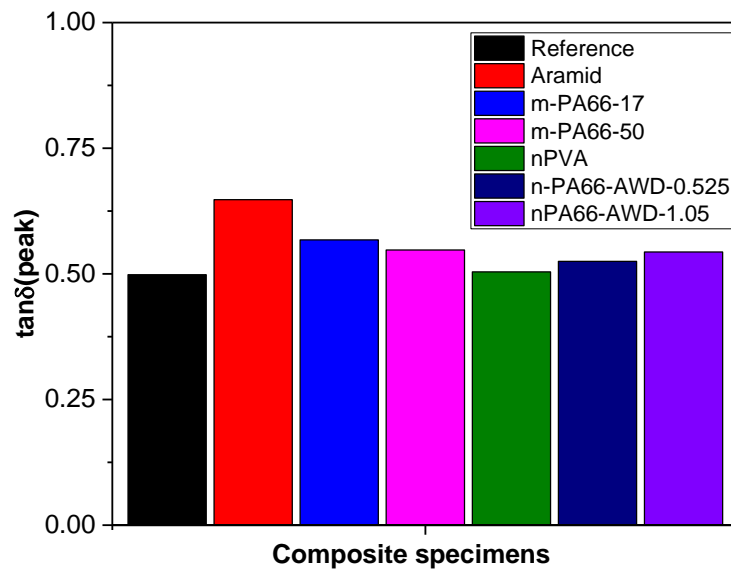


Figure 4.7.2. $\tan\delta$ (peak) values of composite test specimens

4.8. Comparison of interleaf materials on the mechanical performance of CF/EP composites

A comparison of m-AR and m-PA66 interleaving system and the other systems reported in the literature is shown in Table 4.3. It was obvious that the most effective interleaf material was m-PA66 in terms of Mode-I fracture toughness. The effectiveness of nonwoven interleaving system depends on the ability of fiber bridging of the nonwovens. If the microfibers remain inside in the epoxy matrix and not pull-out from the matrix, the improvement in Mode-I fracture toughness was not significant. For instance, although carbon fibers were much stronger than the others, these fibers showed no fiber bridging and remained inside the epoxy matrix therefore no significant improvement was obtained in Mode-I fracture toughness. Another important observation was that if the crack jumped to the relatively weak fiber/matrix interface instead of propagating in nonwoven/nonwoven interface (fiber bridging occurs), the improvement was very small as in the case of PET interleaving.

It was also seen that increasing AWD values led to higher Mode-I fracture toughness. This is due to the fact that higher amount of veil fibers provide a higher extend of fiber bridging that occurs behind the crack fronts and contributes to the interlaminar fracture toughness. However, the increase in the thickness of nonwovens increases the possibility of the crack-jump to the weak interface therefore the optimum thickness of nonwovens should be selected in engineering structure.

As compared to mechanical and material approaches used for delamination toughening, the Mode-I fracture toughness values achieved by using this m-PA66 interleaving system were found to be much higher than those methods such as Z-anchoring and epoxy toughening using micro/nano fillers. The incorporation of PA66 nonwoven veils also increased the ILSS and Charpy impact strength of the composites by 25 and 15%, respectively. Therefore, it can be concluded that PA66 interleaving system has the highest potential among the other micro-interleaving systems. Although this interleaving system reduced in-plane mechanical properties such as tensile and flexural strength, it can be used in structural applications subjected to out-of-plane loading in service for improved delamination resistance with minimal cost, and reduced health and safety issues. Additionally, instead of using in the whole composite structure, critical areas with high stress concentrations such as near holes, notches and sharp corners can be interleaved with aramid and PA66 nonwoven veils for better delamination resistance.

The results showed that the addition of aramid nonwovens increased some of the mechanical properties of existing CF/EP composites such as interlaminar shear and Charpy-impact strength. However the improvement in Mode-I fracture toughness values were moderate (about 45%) as compared to PA66 nonwovens. Even though aramid fibers are much stronger than PA66 fibers, most of these fibers are not pulled out from the matrix which causes moderate increase in Mode-I fracture toughness. Similar results were reported in the literature for the aramid and carbon nonwoven interleaved composites.

Table 4.3. Comparison of the effectiveness of various microfiber interleaving systems

Reference	Composite system	Interleaf material	Areal weight density (g/m ²)	Mode-I fracture toughness (% increase)
This study	CF/EP	AR	8.5	45
This study	CF/EP	PA66	17/50	168/708
[64]	CF/EP	CF	12	28
[90]	CF/EP	PEEK ¹	11	102
[90]	CF/EP	PPS ²	40	133
[63]	CF/BMI ³	AR ⁴	16	108
[91]	CF/ BE ⁵	PA	34	352
[59]	GF/VE	PA	17	90
[60]	GF/VE	PET	45	12
[61]	GF/PE	PA	17	170
[62]	GF/PE	PU	15	40
[92]	CF/EP	PE	20	83

¹PEEK: Polyether ether ketone, ²PPS: Polyphenylene sulfide, BMI: bismaleimide, ⁴AR: aramid, ⁵Benzoxazine.

Table 4.4 summarizes a comparison of the nanointerleaving results obtained within the present study and reported in the literature by other groups. As can be seen from Table 4.4, although PVA nanofibers led to an increase some of the in-plane mechanical properties, they do not have a positive effect on the Mode-I fracture toughness. On the other hand, PA 66 nanofiber interleaving is a promising technique for improving Mode-I fracture toughness of carbon fiber/epoxy composites without sacrificing the in-plane mechanical properties of those composites. Although Moroni et al. [93] reported a decrease in Mode-I fracture toughness values due to the presence of PA 66 nanofibers, other researchers revealed that it was possible to improve Mode-I fracture toughness values by selecting an optimum electrospinning parameters such as time or nanofiber areal weight. As results of the work by Daelemans et al. [82] and Beckermann et al. [94], it was shown that PA 66 nanofiber interleaving is an effective way for improving Mode-I fracture toughness when the nanofiber areal weight was between 0.5 and 9.0 g/m². Beckermann et al. [94] also revealed that there is a direct relationship between the AWD and Mode-I fracture toughness. Similar results were also

obtained in this study for n-PA66 interleaf material. The increase in AWD values increased the Mode-I fracture toughness. Beckermann et al. [94] also showed that the effectiveness of the PA 66 nanofibers reached to a maximum of Mode-I fracture toughness when the AWD was 4.5 g/m^2 . In the previous studies focused on the PA 66 nanofiber interleaving, the average nanofiber diameter obtained was within the range of 150-200 nm. In the present work, the average diameter of the nanofibers produced was 87 nm and nanofiber AWD values were lower than those reported in the literature. As stated by Palazetti [95], thinner nanofibers led to more significant improvement in Mode-I fracture toughness. Based on these findings, it can be concluded that the present results are relevant with the findings reported in the literature. It can be also concluded that although it is possible to obtain AWD values greater than 2 g/m^2 , a relatively long nanofiber coating durations may not be feasible and not applicable in industrial scale. The electrospinning parameters need to be optimized for feasible production and critical improvements in mechanical behaviour of the composites. Furthermore, recent studies also focused on the improvements of the mechanical performance of electrospun nanofibers. Xiang and Frey [96] revealed that the strength of the electrospun PA66 nanofibers can be increased significantly by incorporating 1 wt % carbon nanotubes (CNTs) into the fiber structure. The authors showed that Young's modulus, tensile strength, and toughness of the PA non-woven fiber mats increased 51, 87, and 136%, respectively, after incorporating 1 wt % CNTs into the PA66 nanofibers. Moreover, techniques such as thermal or solvent bonding may be tried to improve mechanical properties of the PA66 nanofibers. Therefore, among the other techniques, the nanofiber interleaving has significant potential for improving delamination resistance of composites. The transition of the nanofiber-interleaving technique into commercial products has already started, and now the first commercial supplies of thermoplastic nanoveils are on the market.

It was also shown in Table 4.4 that the presence of PA 66 nanofibers are also effective for improving in-plane mechanical properties such as flexural strength, flexural modulus and compressive strength of carbon fiber/epoxy composites. As compared to micro-scaled nonwovens, it is possible to increase delamination resistance without sacrificing in-plane mechanical properties of existing CF/EP composites using nano-scaled nonwovens in the interlaminar region. Generally, higher toughness comes

with the lower strength because there is an inverse relationship between toughness and strength. The ability to improve fracture toughness without compromising in-plane mechanical properties makes the thermoplastic nanofiber interleaving technique unique compared to the other techniques in the literature. Moreover, it was shown that the in-plane mechanical properties of composites could be improved using very low amount of nanofibers in the same time.

One of the key factors in nanofiber interleaving technique is the selection of polymer type for electrospinning. If the purpose of electrospun interleaving is to improve Mode-I fracture toughness together with an in-plane mechanical property such as compressive strength, PA66 nanofibers would be a good choice. However, as can be seen in Table 4.4, the PA 66 nanofibers were found not to be very effective for improving flexural strength and modulus of carbon fiber/epoxy composites as compared those obtained with the PAN interleaving as reported by Herwan et al. [75] and Molnar et al [97]. This can be explained by the fact that the higher elastic modulus of PAN nanofibers (7.6 GPa, [75]) than PA 66 nanofibers (0.9-1.2 GPa, [75]). On the other hand, PA66 nanofibers were more effective than PAN nanofibers in terms of absorption of impact energy. Therefore, it is very important to select the correct polymer type with optimum areal weight density to obtain desired mechanical performance. The areal weight density, in other words, nanofiber layer thickness directly affects the mechanical performance of the composites.

Although higher nanofiber thickness means higher amount of nanofibers that will be participated in fiber bridging mechanism in crack propagation, it will definitely reduce the primary reinforcement volume fraction. Consequently, the in-plane mechanical properties will be influenced adversely. Moreover, the increase in electrospinning duration may cause undesired nanofiber morphology such as beads and droplets in the resulting laminate due to possible changes in temperature and humidity during electrospinning process. Also, the increase in electrospinning duration is not feasible in terms of commercialization of thermoplastic nanofiber interleaving technique. Therefore, the next step can be applying possible techniques to obtain these nanofibers with optimum mechanical properties. It was also observed that the uniformity of nanofiber coating was very important to obtain sufficient improvement in

mechanical performance of composites. Also, non-uniform distribution of nanofibers in the interlaminar region may cause inconsistent results (higher standard deviations) and false judgements about their effects on the mechanical behaviour of fiber reinforced composites.

Table 4.4. Comparison of the effectiveness of various nanofiber interleaving systems (*NR: not reported)

Reference	Average nanofiber diameter (nm)	Areal weight density(g/m ²)	Nanofiber material	Property	Improvement or reduction (%)
This study	329±58	0.71	PVA	Tensile strength	+7
				Flexural strength	+16
				Compressive strength	+5
				ILSS	-4
				Charpy impact strength	+11
				Mode-I fracture toughness	-17
This study	87±22	0.525 /1.05	PA 66	Tensile strength	-9.8
				Flexural modulus	+15.6
				Flexural strength	+12.8
				Compressive strength	+15
				ILSS	+9.6
				Charpy impact strength	+18
				Mode-I fracture toughness	+50
[75]	150	NR*	PAN**	Flexural strength	+55
				Flexural modulus	+20
[76]	300	NR*	P(St-co-GMA)	Tensile strength	+14
[82]	158±19	3.0	PA 6/6	Mode-I fracture toughness	+40
[93]	150 ± 20	NR	PA 6/6	Mode-I fracture toughness	-17
[94]	150-300	4.5	PA 6/6	Mode-I fracture toughness	+156
[98]	170±30	NR	PA 6/6	Mode-I fracture toughness	+50
[97]	195±46	1.0	PAN	Flexural strength	+54
				Flexural modulus	+21
				ILSS	+11
				Charpy impact strength	+13

CHAPTER 5

FINITE ELEMENT MODELING OF CF/EP COMPOSITES INTERLEAVED BY ELECTROSPUN PA 66 NANOFIBERS

5.1. Delamination analysis using ANSYS

There are two techniques in ANSYS to simulate the behavior of crack that will propagate along a known path [99]:

- Cohesive zone model (CZM)
- Virtual crack closure technique (VCCT)

These techniques are commonly used for the modeling of delamination in composite structures, since the crack is assumed to propagate at the interface between layers. Both techniques use special elements (interface or contact) along a predefined interface to model the delamination of cracks.

In this study, cohesive zone modeling was used to simulate behavior of reference and PA66 nanomodified composite specimens under Mode-I loading.

5.2. Cohesive zone modeling

The cohesive zone approach can be explained using a detail view of the crack tip shown in Figure 5.1. The crack has a process zone acting as a transition region between traction free and the intact region of the bulk material. This region, also called outer region, has a different non-linear profile whereas the traction free part is named as inner region. The process zone was shown by set of springs to denote the existence of cohesive forces which result in a unique traction profile at the crack edge. The cohesive

tractions between the crack surfaces correspond to the resistance to crack propagation. Under external loading, the atomic structure of a material changes and is reflected as variations in the cohesive traction. Up to a certain amount of separation between the adjacent surfaces, the cohesive traction shows an increasing trend. After a critical separation is reached, the cohesive traction starts to decrease towards zero. When the interfacial tractions diminish, the cohesive surfaces begin to separate with each other. The stress state between the cohesive surfaces obeys according to certain material softening law, which is called the cohesive law, or the traction-separation law [100].

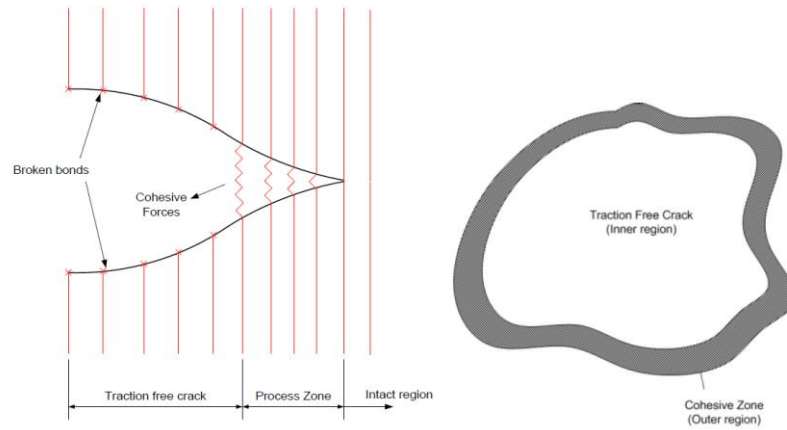


Figure 5.2.1. Bonding and debonding in the process zone [101].

The traction-separation relation for a mode-I crack is generally characterized using a scalar surface potential Φ by setting [101];

$$T_n = \frac{\partial \phi}{\partial \Delta_n} \quad (1)$$

where T_n denotes continuum normal traction and Δ_n is the normal separation between two surfaces of cohesive zone. The surface potential Φ actually represents the energy needed to separate the interface, i.e. separation between two surfaces of cohesive zone. If a proper potential function Φ is available, the constitutive equation between the cohesive traction and the relative separation can be derived. A large variety of proper function has been described in literature such as (a) polynomial, (b) piece-wise linear, (c) exponential and (d) rigid-linear.

There are basically two approaches to develop a cohesive law: (i) experimental measurements or (ii) phenomenological way with predefined functional assumption and estimated parameters. Since there is no effective experimental method available to directly determine the traction–separation relation, in this study, the latter approach was used. The proper law of the traction–separation relation for the cohesive zone was selected and the cohesive parameters were treated as modeling constants. The cohesive parameters were determined by fitting the CZM simulation results to the set of experimental data [100].

There are two types of elements capable of using a CZM material model in ANSYS [102].

(i) **Interface elements:** They can occupy a finite thickness between the two surfaces that they join or they can have zero thickness. In any cases, the contact between the two surfaces is known before the analysis and the surfaces are thus joined by the interface elements.

(ii) **Contact elements:** have zero thickness and can detect contact, separation, penetration, and slip between a contact surface and a target surface. The CZM model can be used only with bonded contact.

In this study, for the interface, TARGE169 elements were employed with its associated contact surface element (CONTA171). PLANE182 elements were used for 2-D modeling of composite specimens. PLANE182 is defined by four nodes having two degrees of freedom at each node: translations in the nodal x and y directions. CONTA171 has two degrees of freedom at each node: translations in the nodal x and y directions.

In order to reduce the computational cost of 3D simulation computational time, all numerical simulations were carried out under plane-strain assumptions. In plane-strain, the applied forces act in the x-y plane and do not vary in the z-direction. The strains are independent of the out-of-plane coordinate. The loads are uniformly distributed with respect to the large dimension as in the case of Mode-I fracture toughness test.

5.3. FEM model

In order to verify numerical model used in this study, a DCB problem was taken from the literature and the obtained results were compared with the published results. The dimensions of the DCB specimen were 100 mm (length) \times 20 mm (width). The specimen was composed of four unidirectional plies with a total thickness of 3 mm. The initial crack (a) was inserted 30 mm away from the loaded edge. Table 5.1 shows material properties of the composite specimen.

Table 5.1. Material properties of composites used for verification

	Value
E_1 (GPa)	135.3
E_2 (GPa)	9.0
G_{12} (GPa)	5.2
ν_{12} (-)	0.26

Figure 5.3.1(a) shows the mesh structure of the composite specimen. In total, 2280 elements and 2406 nodes were used to create FEM model of the composite specimen. Boundary and loading conditions were as follows; the right end of the beam is fixed and a constant displacement of 10 mm is applied on left edges of the beam as shown in Figure 5.3.1(b). Figure 5.3.2 shows von-Mises stress distribution in the specimen obtained from the numerical analysis. As expected, the stress values reach the maximum value at the crack tip. Table 5.2 shows the comparison of the obtained FEM results with the literature. It can be seen that very close agreement were found.

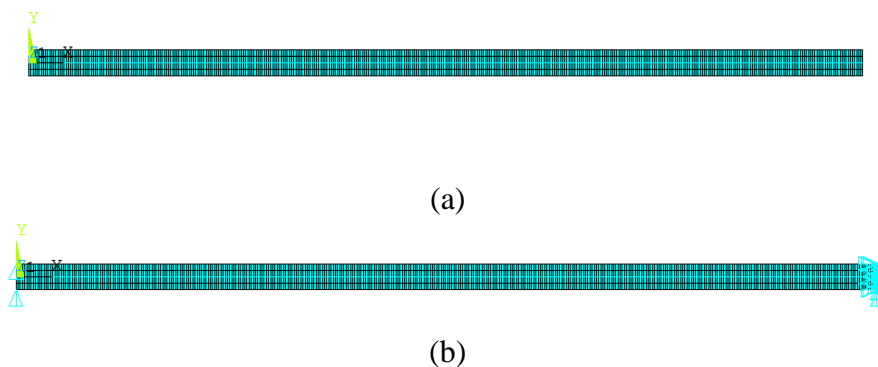


Figure 5.3.1. (a) Mesh structure and (b) boundary and loading conditions

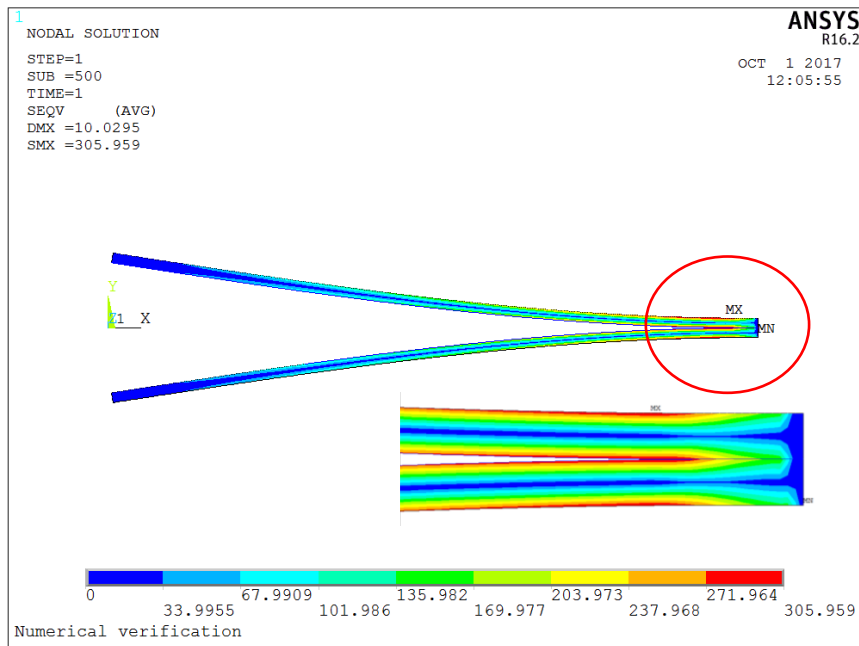


Figure 5.3.2. von-Mises stress distribution in DCB composite specimen

The FE model was extended to simulate the behavior of reference specimens under mode-I loading. To simulate the experiments, the dimensions of the model were changed as 137.5x25x1.2 mm. The numerical data were compared with the pre-cracked test results. Therefore, the length of initial crack was considered as 53 mm. The material properties were taken from Chapter 4 and entered directly to the FEM model. The mesh structure, loading and boundary conditions were kept the same as in the verification case. The cohesive zone parameters were changed to fit the CZM simulation results to the set of experimental data.

Table 5.2. Comparison of experimental and numerical results

	Max Force F_Y (N)	End Reaction force F_Y (N)	Von-Mises Stress (MPa)
Reference [102]	60.09	24.00	305.23
This study	58.59	24.07	305.96

5.4. Comparison of experimental and numerical results

Figure 5.4.1 shows comparison between experimental results and cohesive zone model response in the case of reference specimens. The FE model predictions were in reasonable agreement with the experimental test data although the predicted maximum force values were little lower than those of the experiments. The predicted maximum force was 12.5 N whereas the average maximum load of the reference specimens was 14.4 N. The numerical error was about 13% which could be reduced by tuning the cohesive zone parameters. However, the correct prediction of Mode-I fracture toughness is more important than the accuracy of maximum load prediction. Therefore the cohesive zone parameters were adjusted to obtain highest accuracy in fracture toughness values. The cohesive zone parameters were as follows; the maximum contact stress (σ_{\max}), critical fracture energy density (G_{cn}) and artificial damping coefficient (η) were 25, 0.25 and 0.0001; respectively.

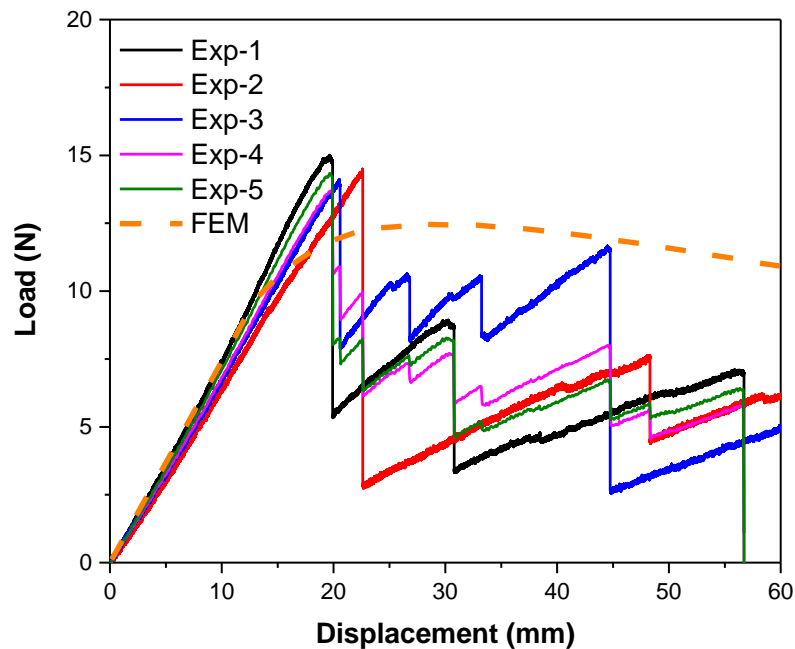
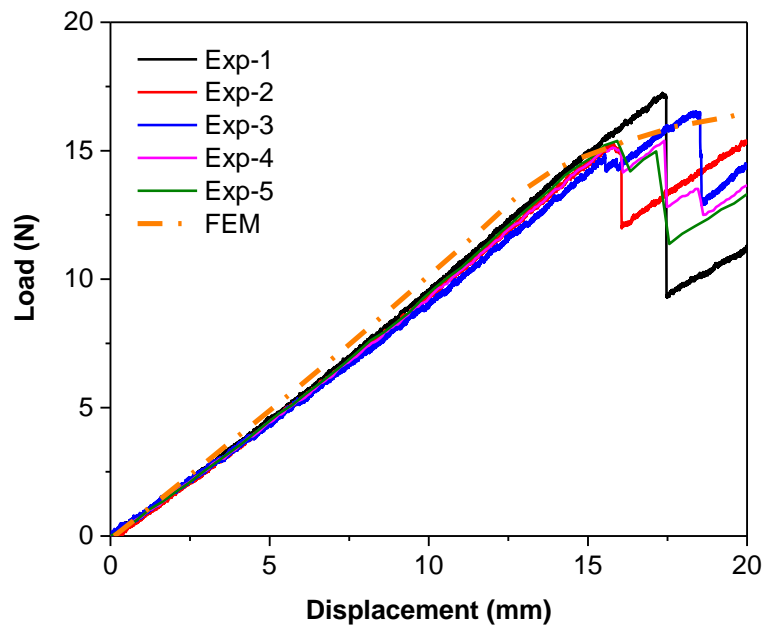
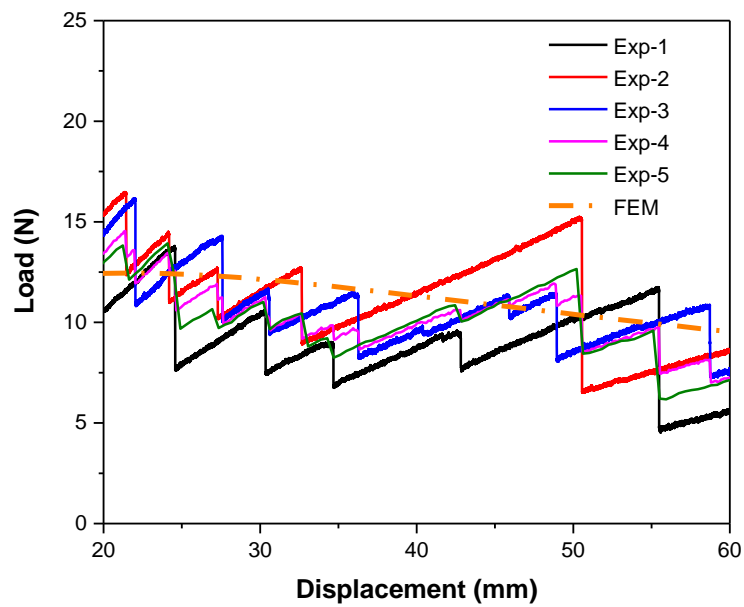


Figure 5.4.1. Comparison between experimental and cohesive zone model in the case of reference specimens

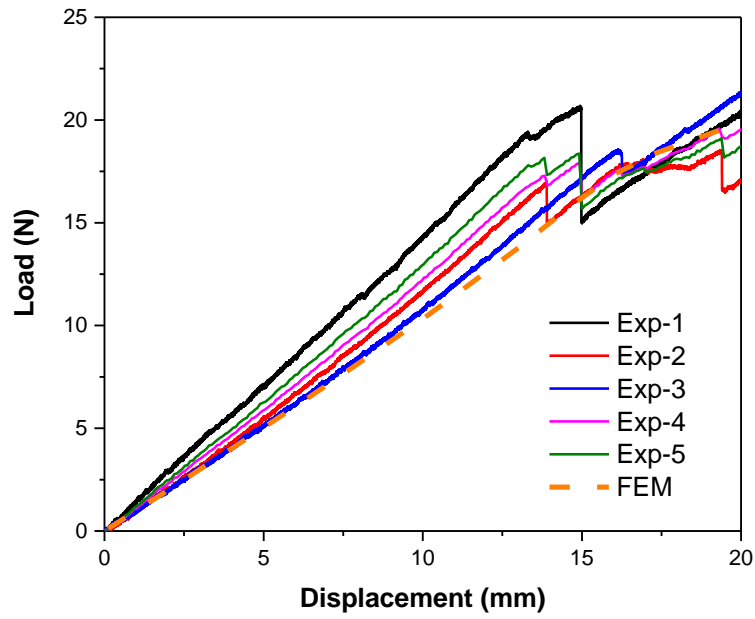


(a)

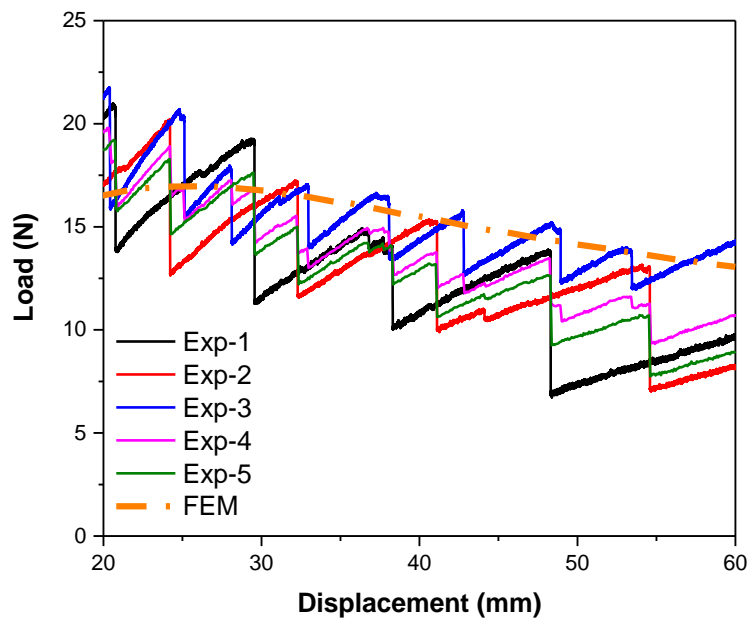


(b)

Figure 5.4.2. Comparison between experimental and cohesive zone model in the case of n-PA66-AWD-0.525 specimens (a) initial and (b) propagation stage



(a)



(b)

Figure 5.4.3. Comparison between experimental and cohesive zone model in the case of n-PA66-AWD-1.05 specimens (a) initial and (b) propagation stage

Figure 5.4.2 and Figure 5.4.3 show the numerical results of n-PA66-AWD-0.525 and n-PA66-AWD-1.05 composite specimens. The initial and propagation stages of the PA66 nanomodified specimens were predicted with two different bilinear cohesive zone models. Table 5.3 shows the cohesive zone parameter values for each specimen. The results of two different cohesive zone models were superposed to calculate the Mode-I fracture toughness of the composite specimens. The area under the curves was used to determine the Mode-I fracture toughness values of the specimens. Table 5.4 presents the numerical Mode-I fracture toughness values with comparison of experimental data. It can be said that the numerical predictions were good agreement with the experimental results. The numerical error in the analyses was in the range between 3-7%.

Table 5.3. Cohesive zone parameters used for numerical modeling of nanomodified composite specimens

<i>n-PA66-AWD-0.525 composite specimens</i>			
	σ_{\max}	G_{cn}	η
Initial stage	40	0.50	0.0001
Propagation stage	25	0.25	0.0001
<i>n-PA66-AWD-1.05 composite specimens</i>			
	σ_{\max}	G_{cn}	η
Initial stage	85	0.65	0.0001
Propagation stage	40	0.50	0.0001

Table 5.4. Comparison of numerical and experimental Mode-I fracture toughness values for reference and PA66 nanomodified specimens

Specimens	Numerical Mode-I fracture toughness (kJ/m²)	Experimental Mode-I fracture toughness (kJ/m²)	% Numerical error
Reference	0.258	0.240	7.5
<i>n-PA66-AWD-0.525</i>	0.306	0.295	3.73
<i>n-PA66-AWD-1.05</i>	0.380	0.358	6.14

CHAPTER 6

CONCLUDING REMARKS AND FUTURE WORK

6.1. Conclusions

Over the past decades, fiber reinforced composites have been used in many engineering applications ranging from trivial, industrial products such as boxes and covers produced in enormous numbers each day, to pipelines and crucial, load bearing parts of large structures. Performance of these materials is tailored to the requirements of the costumers by selecting the reinforcement and matrix materials, changing the fiber architecture or modifying the fiber-matrix interface.

Recently, there has been a growing demand for higher performance composites than those currently in the market. Therefore, researchers are seeking to find out the ways to improve mechanical performance of existing fiber reinforced composites. Nanocomposites in which nanomaterials (nanofibers, nanoparticles etc.) are used for the reinforcement purpose offer new solutions to enhance the mechanical properties of these fiber reinforced composites.

In the case of laminated composites, delamination, the separation of adjacent layers due to weakening of interface layer, is the most common failure mode when they subjected to impact or fatigue loading. It is caused by high interlaminar stresses in conjunction with the typically very low through-thickness strength. A number methods to improve delamination resistance (fracture toughness) have been developed and evaluated over the years such as matrix toughening with nanomaterials, laminate stitching, interleaving, optimization of ply sequence, critical ply termination etc.

Thermoplastic nanofibers produced by electrospinning technique are considered as the promising interleaf materials to reinforce the interlaminar region of laminated composites. The idea comes from the fact that structural failure occurs in critical areas where the matrix is not reinforced and high stress concentrations are highly localized.

The incorporation of an entangled nanofiber layer improves interlaminar fracture toughness like the “hooks and loops” in Velcro. Electrospun nanofibers are obtained in the form of nonwoven mats that uniformly distributed in the polymer matrix. Very low amount of nanofibers in the interlaminar region cause no significant change in the thickness and primary reinforcement fiber volume fraction of the resulting laminate.

This study aims to compare the effects of micro and nano-scaled nonwoven interleaf materials on the mechanical behavior of CF/EP composites. Different types of interleaf materials such as aramid and PA 66 nonwovens composed of microfibers and PVA and PA66 nonwoven mats produced by electrospinning were used to improve mechanical performance of CF/EP composites.

Different types of micro-scaled nonwovens such as carbon, aramid, polyester, PA66 are available in the market. Aramid is less studied material among the others. PA66 nonwovens were selected to be compared with the PA66 nanofiber interleaving. PVA nanofibers were chosen as one of the nano interleaf materials because PVA is a cheap, water-soluble, odorless and non-toxic polymer. There were no published studies in the literature about the effects of PVA nanofibers on the mechanical properties of CF/EP composites. PA66 nanofibers were selected due to the following reasons; they are relatively cheap, dissolves easily in a wide range of solvents and have better mechanical properties compared to other polymers. Their melting point is higher than the curing temperature of most of the matrices which makes the polymer morphologically stable in the resulting laminate. The effects of areal weight density of these nonwovens on the mechanical properties of these composites were investigated. Thermomechanical behavior of CF/EP composites with/without interleaf materials was determined via Dynamic Mechanical Analysis (DMA). SEM analysis was used to investigate the morphology of nonwovens, fracture surfaces of the composite specimens and deduce the toughening mechanisms. Finite element analyses were carried out to predict the CF/EP composites interleaved by electrospun PA66 nanofibers.

The results showed that aramid nonwovens were moderately effective in improving the Mode-I fracture toughness. The increase in average Mode-I fracture toughness was about 45% as compared to reference composite specimens. The addition of these nonwovens led to an increase about 14 and 13% in the interlaminar shear and

Charpy impact strength values, respectively. However, in-plane mechanical properties were adversely affected by addition of these nonwovens. Tensile, flexural and compressive strength values decreased 13, 7 and 10%; respectively. Additionally, the damping ability of the composites increased with the incorporation of aramid nonwovens. On the other hand, commercial PA66 nonwovens were much more effective than the aramid nonwovens in terms of Mode-I delamination resistance. The Mode-I fracture toughness increased almost seven times as compared to reference specimens. Most of the aramid microfibers remained inside the polymer matrix and did not participate in fiber bridging whereas large amount of PA66 microfibers kept the carbon plies together and led to significant increase in Mode-I fracture toughness. As in the case of aramid nonwoven interleaved composites, PA 66 nonwovens caused a significant reduction in in-plane mechanical properties. With the addition of PA66 nonwovens with an ADW value of 50 gsm, tensile, flexural and compressive strength values decreased 41, 28 and 14%; respectively. The reasons for decrease in micro-scaled interleaving were reduced fiber volume fraction, increased thickness and void formation during the composite manufacturing. Higher amount of microfibers in the interlaminar region caused higher reduction in in-plane mechanical properties of CF/EP composites.

On the contrary, in the case of nano-scaled interleaving, more promising results were obtained regarding the in-plane mechanical properties of composites. The results showed that the use of electrospun nanofibers could increase some of in-plane mechanical properties of composites. The incorporation of PVA nanofibers increased tensile, flexural and compressive strength by 7, 16, 11% respectively. Charpy impact strength was also increased by 11%. PVA nanofibers reduced Mode-I fracture toughness about 17%. The reason for this decrease can be attributed to low mechanical strength of these nanofibers and their lack of ability to keep carbon plies during the tests. Additionally, they prevented fiber bridging occurred between carbon plies which resulted in lower fracture toughness. It was observed that PA 66 nanofibers were more effective in terms of mechanical performance of CF/EP composites as compared to PVA nanofibers. Although these nanofibers reduced tensile strength of the composites, they led to significant increase in in-plane mechanical properties of the composites. The flexural and compressive strength increased about 13 and 15% respectively. Also, the

interlaminar shear and Charpy impact strength increased by 10 and 18% respectively. Interlaminar fracture toughness was improved about 50% with the addition of PA66 nanofibers. Another important observation was that the positive effect of the nanofibers increases with increasing areal weight density of the nanofibers.

Numerical studies showed that it was possible to simulate nanofiber interleaved specimens with cohesive zone modeling approach. The bilinear CZM model was used to simulate reference specimens under Mode-I loading. However, nanomodified specimens behaved differently due to nanofiber bridging occurred in Mode-I fracture toughness tests. Therefore two different bilinear CZM models were used to simulate the nanomodified composite specimens so that the material parameters were adjusted to predict the maximum force at the initial stage and propagation fracture toughness of the composites. The numerical results showed good agreement with the experimental results.

6.2. Future work

The use of thermoplastic electrospun nanofibers as a secondary reinforcement offers great potential to improve the delamination and impact resistance without compromising in-plane mechanical properties of CF/EP composites. Moreover, these nanofibers may lead to an increase in tensile, flexural and compressive strength depending on the polymer type and nanofiber mat thickness. A solid knowledge has been gained on this topic and the transition of the nanofiber-interleaving technique into commercial products has already started. Now, the first commercial supplies of thermoplastic nanofiber nonwoven mats are on the market. However, some problems related to this technique such as costs, low production rate, low repeatability are needed to be solved. Also, there is still some distance from of a full understanding of this technique to provide wider range of application.

From a research point of view, there are certain gaps to be filled in terms of clear understanding the behavior of nanomodified composites;

- The effects of nanofiber interleaving technique on aramid fiber reinforced composites are still unknown.
- The effects of temperature and humidity aging on nanointerleaved composites can be investigated.
- The behavior of nanomodified composites under static Mode-I and Mode-II loading is one of the most-widely studied topics in this field. However, fatigue behavior of nanomodified GFRP composites still remains as an open question in the literature. Fatigue crack growth in these composites under Mode-II loading has still several gaps due to the difficulty of addressing crack propagation mechanisms in sliding mode.
- The impact and post-impact behavior of nanomodified composites depends on many parameters such as thickness, lay-up sequence, number of interlayers, velocity of the impactor etc. To reveal the effects of these variables, the impact response of nanocomposites is needed to be studied and understood. In this context, tensile after impact (TAI) and compression after impact (CAI) behavior of nanomodified composites could also be investigated.
- The studies on the vibration characteristics of nanomodified composites are still in the primitive stage and further research needs to be done. If nanofibers are shown to be effective to reduce or tune the free vibration response of a structure, it will certainly make a significant positive impact on their application in industry.
- Persistent efforts to improve manufacturing techniques and reduce the electrospinning time by using different types of hybrid nanofibers in the interlaminar region should be made to integrate this technique into existing production lines. Further studies are also needed to understand the cost benefit analysis of using electrospun nanofibers as a secondary reinforcement material.
- Another direction would be to assess the performance of nanointerlayer toughening combined with the other traditional improvement techniques such as z-pinning and stitching. This could reduce their negative effects

on the in-plane mechanical properties of fiber reinforced composites with the highest improvement in fracture toughness.

- The addition of healing substances into electrospun nanofibers ensures their homogenous distribution throughout the matrix material. This will contribute to a feasible and economic fabrication of self-healing composites.

6.3. List of publications

SCI-Expanded publications

1. Beylergil, B., Tanoglu, M. and Aktaş, E. “Enhancement of interlaminar fracture toughness of carbon fiber/epoxy composites using polyamide 6/6 electrospun nanofibers”, Journal of Applied Polymer Science, Volume 134, Issue 35, September 15, 2017, 45244.

2. Beylergil, B., Tanoglu, M. and Aktaş, E. “Modification of carbon fiber epoxy composites by polyvinyl alcohol (PVA) based electrospun nanofibers”, Advanced Composites Letters, 2016, 26(3), 69-76.

National and international conference proceedings

1. Beylergil, B. and Tanoğlu, M. “Improving Mode-I fracture toughness of woven carbon fiber/epoxy composites using polyamide- 6,6 (PA 66) nonwoven fabrics”, V. Uluslararası Polimerik Kompozitler Sempozyumu ve Çalıştayları, 2-4 Kasım 2017, İzmir, Turkey.

2. Beylergil, B. and Tanoğlu, M. “Karbon elyaf / epoksi kompozitlerin mekanik performansının poliamid-6,6 (PA 66) nanofiberler kullanılarak iyileştirilmesi”, Teknik sunum, Türk Kompozit 2017, İstanbul, Turkey.

3. Beylergil, B. and Tanoğlu, M. “Karbon fiber/epoksi kompozitlerin kırılma tokluğunun poliamid 66 nanofiberler kullanılarak iyileştirilmesi”, 2. Uluslararası Lif ve Polimer Araştırmaları Sempozyumu, 2017, Bursa, Turkey.

4. Beylergil, B. and Tanođlu, M. “Improving delamination resistance of carbon fiber/epoxy composites using PA 66/GNPs hybrid nanofibers”, NART 2017, Prague, Czech Republic.
5. Beylergil, B. and Tanođlu, M. “Toughness improvement of carbon fiber/epoxy composites by polyamide-6,6 (PA 66) nonwoven fabrics”. PPM 2017, Kuşadası, İzmir, Turkey.
6. Beylergil, B. and Tanođlu, M. “Preparation and characterization of electrospun polyvinyl alcohol PVA halloysite nanotubes HNTs hybrid nanofibers”, PPM 2015, Çeşme, İzmir, Turkey.
7. Beylergil, B. and Tanođlu, M. “Toughening of unidirectional carbon fiber epoxy composites by polyvinyl alcohol nanofiber interlayers”, NART 2015, Prague, Czech Republic.
8. Beylergil, B. and Tanođlu, M. “Improving mechanical performance of unidirectional carbon fiber epoxy composites by polyvinyl alcohol electrospun nanofibers”, PPM 2015, Çeşme, İzmir, Turkey.
9. Beylergil, B. and Tanođlu, M. “Poliamid 66 nanofiberler kullanılarak karbon fiber vinil ester kompozitlerin kırılma toklugunun arttirilmesi”, ASELSAN 2. Malzeme Teknolojileri Çalıstayı, 2016, Ankara, Turkey.
10. Beylergil, B. and Tanođlu, M. “Karbon elyaf epoksi kompozitlerin poliamid 6 6 nanofiberler kullanılarak kırılma toklugunun arttirilmesi”, 8.Savunma Teknolojileri Kongresi SAVTEK 2016, Ankara, Turkey.
11. Beylergil, B. and Tanođlu, M. “Karbon elyaf epoksi kompozitlerin mekanik performansinin polivinilalkol PVA nanofiberler kullanılarak iyileştirilmesi”, Türk Kompozit 2015, Istanbul, Turkey.

REFERENCES

- [1] Beylergil B., Cunedioğlu Y. and Aktas A. Enhancement of single-lap composite joints strength at different temperatures, *Journal of Adhesion Science and Technology*, 26: 10-11, 1453-1465, 2012.
- [2] Greenhalgh E. S. Rogers C. and Robinson P. Fractographic observations on delamination growth and the subsequent migration through the laminate, *Composite Science and Technology*, 69, 2345–2351, 2009.
- [3] Greenhalgh E. S. In *Woodhead Publishing Series in Composites Science and Engineering*; CRC Press: Boca Raton, FL, 2009; pp 164–165.
- [4] Beylergil, B., Tanoglu, M. and Aktaş, E. Enhancement of interlaminar fracture toughness of carbon fiber/epoxy composites using polyamide 6/6 electrospun nanofibers, *Journal of Applied Polymer Science*, 134(35), 45244, 2017.
- [5] Kuwata M. Mechanisms of Interlaminar Fracture Toughness using Non-Woven Veils as Interleaf Materials. Queen Mary, University of London, School of Engineering and Materials Science, Department of Materials, 2010.
- [6] Dzenis Y.A. and Reneker D.H. Delamination resistant composites prepared by small diameter fiber reinforcement at ply interfaces, US Patent No: US 6265333, 2001.
- [7] Xantu-Layr Fiber Product Catalog. website: <https://www.revolutionfibres.com/wp-content/uploads/2014/03/Xantu-Layr-Product-Catalogue-v3.1.pdf>, Access date: 10.02.2017.
- [8] Dragan A. and Carlone P. Soft computing in the design and manufacturing of composite materials, *Woodhead Publishing Series*, 2015.
- [9] Prasad N. Development and characterization of metal matrix composite using red mud an industrial waste for wear resistant applications, PhD thesis, Department of Mechanical Engineering National Institute of Technology Rourkela, 2006.

- [10] History of composites, website: <http://compositeslab.com/composites-101/history-of-composites>, Access date: 10.02.2017.
- [11] American Chemical Society, Leo Hendrick Baekeland and the Invention of Bakelite National Historic Chemical Landmark, website: <https://www.acs.org/content/acs/en/education/whatischemistry/landmarks/bakelite.html>, Access date: 10.02.2017.
- [12] Pyramid builders and building the pyramids of ancient Egypt, website: <http://factsanddetails.com/world/cat56/sub365/item1932.html>, Access date: 10.02.2017.
- [13] History of Composite Materials, Mal-bar Cooperation, website: <http://www.mar-bal.com/language/en/applications/history-of-composites>, Access date: 10.02.2017.
- [14] The constructor: Methods to Improve Ductility of RCC Beams with fiber reinforced polymer bars website: <https://theconstructor.org/structural-engg/improve-ductility-rcc-beams-frp-bars-methods/15862>, Access date: 10.02.2017.
- [15] Dr. PM Mohite., AE-681 Composite Materials lecture notes website: http://home.iitk.ac.in/~mohite/Composite_introduction.pdf, Access date: 10.02.2017.
- [16] Wang R-U., Zheng S-R. and Zheng Y-P. Polymer matrix composites and technology, Woodhead Publishing Series in Materials, 2011.
- [17] Gan Y.X. Effect of Interface Structure on Mechanical Properties of Advanced Composite Materials. International Journal of Molecular Sciences. 10(12), 5115-5134, 2009.
- [18] Drach A., Drach B., Tsukrov I., Bayraktar H. and Goering J. Realistic FEA modeling of 3D woven composites on mesoscale, The 19th international conference on composite materials, 2013.
- [19] Campbell F. C. Structural composites, Introduction to composite materials website: http://www.asminternational.org/documents/10192/1849770/05287G_Sample_Chapter.pdf, Access date: 10.02.2017.

[20] Carbon fiber Australia, Website: <http://www.carbonfiber.com.au/prod70.htm>, Access date: 10.02.2017.

[21] Hergueta F.C. Multiscale analysis of the mechanical behaviour of needle-punched nonwoven fabrics, PhD thesis, Universidad Politecnica de Madrid, 2016.

[22] Quartus Engineering Composite 101 Lecture notes, website: <http://www.quartus.com/resources/white-papers/composites-101/> Access date: 10.02.2017.

[23] Agarwal B.D., Broutman L.J., Chandrashekhara K. Analysis and performance of fiber composites, Wiley&Sons, 2015.

[24] Hashmi S. Comprehensive Materials Processing, ISBN: 978-0-08-096533-8, Elsevier Ltd., 2014.

[25] Li S., Zhang Y., Han J., Zhou Y. Fabrication and characterization of SiC whisker reinforced reaction bonded SiC composite, Ceramics International, 39, 449–455, 2013.

[26] Prof. Satish V. Kailas, Material Science lecture notes website: http://nptel.ac.in/courses/112108150/pdf/Web_Pages/WEBP_M12.pdf, Access date: 10.02.2017.

[27] Miroslava Klárová, Composite materials lecture notes, website: http://katedry.fmmi.vsb.cz/Opory_FMMI_ENG/2_rocnik/TRaCM/Composite%20materials.pdf, Access date: 10.02.2017.

[28] Princeton university lecture notes- Chapter 3: Polymer matrix composites, website: <https://www.princeton.edu/~ota/disk2/1988/8801/880106.PDF>, Access date: 10.02.2017.

[29] Ullmann's Polymers and Plastics: Products and Processes, Publisher: Wiley-VCH ISBN 10: 3527338233, 2016.

[30] Hull D., Clyne T. W. An Introduction to Composite Materials (Cambridge Solid State Science Series) 2nd Edition, Cambridge Solid State Science Series, 1996.

[31] Kessler M.R. Polymer Matrix Composites: A Perspective for a Special Issue of Polymer Reviews, Polymer Reviews, 229-233, 2012.

[32] Comparison of Carbon Fiber, Kevlar (Aramid) and E Glass used in Composites for Boatbuilding website: <http://www.christinedemerchant.com/carbon-kevlar-glass-comparison.html>, Access date: 10.02.2017.

[33] Vicari A., Will Carbon Fiber Find Widespread Use in the Automotive Industry?, website: <http://www.machinedesign.com/contributing-technical-experts/will-carbon-fiber-find-widespread-use-automotive-industry>, Access date: 10.02.2017.

[34] SAE international, Cutting costs of carbon composites, website: <http://articles.sae.org/11618/>, Access date: 10.02.2017.

[35] Heider D., Newton C, Gillespie J.W. VARTM variability and substantiation website: https://depts.washington.edu/amtas/events/jams_06/Heider.pdf, Access date: 10.02.2017.

[36] Vacuum Assisted Resin Transfer Molding Process (VARTM): What it is, what it is Not, what it can, and what it cannot do. website: <https://www.rtmcomposites.com/process/vacuum-assisted-resin-transfer-molding-vartm>, Access date: 10.02.2017.

[37] Miyazaki T., Hosoe S., Fujii Y. Structure of molding tools, injection molding device, and molding method US Patent No: 20100193983.

[38] Aero Consultant AG. Airtech Auxiliary Materials website: <http://www.aero-consultants.ch/en/Airtech-Hilfsmaterialien/Vacuum-Bagging-and-Composite-Tooling.htm> Access date: 10.02.2017.

[39] Dr. P. M. Mohite, Composite Materials and Structures lecture notes, The National Programme on Technology Enhanced Learning (NPTEL) website:

<http://nptel.ac.in/courses/101104010/downloads/Lecture20.pdf>, Access date: 10.02.2017.

[40] Yan L., Chouw N. and Yuan X. Improving the mechanical properties of natural fibre fabric reinforced epoxy composites by alkali treatment, *Journal of Reinforced Plastics and Composites*, 31: 425, 2012.

[41] Naebe M., Abolhasani M.M., Khayyam H., Amini A. and Fox B. Crack Damage in Polymers and Composites: A Review, *Polymer Reviews*, 56:1, 31-69, 2016.

[42] Rashid B. Ceramics for advanced applications: Fracture toughness and toughening mechanisms- website: http://teacher.buet.ac.bd/bazlurrashid/467_feb2013/lec_08.pdf Access date: 10.02.2017.

[43] Yun Z., Xiaoquan C. and Baig Y. Effect of stitching on plane and open-hole strength of CFRP laminates, *Chinese Journal of Aeronautics*, 25: 473-484, 2012.

[44] Wouters M. Effects of fibre bundle size and stitch pattern on the static properties of unidirectional carbon-fibre non-crimp fabric composites, Master Thesis, Luleå University of Technology, Sweden, 2012.

[45] Abounaim M.D. Process development for the manufacturing of flat knitted innovative 3D spacer fabrics for high performance composite applications, PhD Thesis, Technischen Universität Dresden, 2010.

[46] Ghafari-Namini N. and Ghasemnejad H. Effect of natural stitched composites on the crashworthiness of box structures, *Materials and Design* 39,484–494, 2012.

[47] Sharma, S.K. and Sankar, B. V. Effect of stitching on impact and interlaminar properties of graphite/epoxy laminates, *Journal of Thermoplastic Composite Materials*, 10: 241 - 253, 1997.

[48] Kang T. J. and Lee S. H. Effect of stitching on the mechanical and impact Properties of woven Laminate Composite, *Journal of Composite Material*, 28(16): 1574–1587, 1994.

- [49] Yudhanto A., Watanabe N., Iwahori Y. and Hoshi H. Compression properties and damage mechanisms of stitched carbon/epoxy composites, *Composites Science and Technology*, 86: 52–60, 2013.
- [50] Mouritz A. P. Review of z-pinned composite laminates, *Composites Part A: Applied Science and Manufacturing*, 38(12): 2383-2397, 2007.
- [51] Freitas G.A., Magee C. Dardzinski P. and Fusco T. Fiber insertion process for improved damage tolerance in aircraft laminates, *Journal of Advanced Materials*, 25(4):36-43 1994.
- [52] Zhang X, Hounslow L, Grassi M. Improvement to low-velocity impact and compression-after-impact performance of z-fibre pinning. In: *Proceedings of the 13th international conference on composite materials*, San Diego; July 2003.
- [53] Childress J.J., Freitas G. Z-Direction pinning of composite laminates for increased survivability. In: *Proceedings of the AIAA aerospace design conference*, Irvine, California, February 1992. p. 92–109.
- [54] Stinger, L.G. Hiley, M.J. Through thickness reinforcement of composites: z-pinning, stitching and 3-D weaving, *Proceedings of the 14th international conference on composite materials*, San Diego, Paper No. 1312, 14-18 July 2003.
- [55] Steeves C, Fleck N. Z-pinned composite laminates. Knock down in compressive strength. *Fifth deformation and fracture of composites*, London: IMechE; (1999).
- [56] Yokozeki T, Iwahori Y, Ishibashi M, Yanagisawa T, Imai K, Arai M, Takahashi T, Enomoto K. Fracture toughness improvement of CFRP laminates by dispersion of cupstacked carbon nanotubes. *Composites Science and Technology* 2009; 69(14): 2268–2273.
- [57] Ragosta G, Abbate M, Musto P, Scarinzi G, Mascia L. Epoxy–silica particulate nanocomposites: chemical interactions, reinforcement and fracture toughness. *Polymer* 2005; 46(23): 10506–10516.

[58] Phong N. T., Gabr M. H., Okubo K., Chuong B. and Fujii T. Improvement in the mechanical performances of carbon fiber/epoxy composite with addition of nano-(Polyvinyl alcohol) fibers, *Composite Structures*, 99, 380-387, 2013.

[59] Saz-Orozco BD, Ray D, Stanley WF. Effect of thermoplastic veils on interlaminar fracture Toughness of a Glass Fiber/Vinyl Ester Composite. *Polymer Composites* 2015; doi: 10.1002/pc.23840.

[60] Fitzmaurice K., Ray D, McCarthy MA. PET interleaving veils for improved fracture toughness of glass fibre/low-styrene-emission unsaturated polyester resin composites. *Journal of Applied Polymer Science* 2015; 133(3): 42877.

[61] O'Donovan K, Ray D, McCarthy MA. Toughening Effects of Interleaved Nylon Veils on Glass Fabric/Low-Styrene-Emission Unsaturated Polyester Resin Composites. *Journal of Applied Polymer Science* 2014; 132(7): 41462.

[62] Miller SG, Roberts GD, Kohlman LW, Heimann PJ, Pereira JM, Ruggeri CR, 1, Martin RE, McCorkle LS. Impact behavior of composite fan blade leading edge subcomponent with thermoplastic polyurethane interleave. In: *Proceedings of 20th International Conference on Composite Materials*, Denmark; 19-24 Jul. 2015.

[63] Ni N, Wen Y, He D, Yi X, Zhang T, Xu Y. Ex-situ toughness and damping research of the co-cured bismaleimide matrix composite with aramid nonwoven fabrics. *Composites Part B* 2016. doi: 10.1016/j.compositesb.2016.01.042.

[64] Lee S-H, Noguchi H. Kim Y-B. Cheong S-K. Effect of Interleaved Non-Woven Carbon Tissue on Interlaminar Fracture Toughness of Laminated Composites: Part II – Mode I. *Journal of Composite Materials* 2002; 36(18): 2153–2168.

[65] Persano L., Camposeo A., Tekmen C. and Pisignano D. Industrial upscaling of electrospinning and applications of polymer nanofibers: a review, *Macromolecular Materials and Engineering*, 298: 504-520, 2013.

[66] Webpage: <http://www.people.vcu.edu/~glbowlin/electrospinning.htm>, Accessed on: 5/11/2015, Accessed on: 5/11/2015.

[67] Webpage: <http://www.people.vcu.edu/~glbowlin/images/electrospinning.jpg>, Accessed on: 5/11/2015.

[68] Li Z. and Wang C. One-Dimensional Nanostructures, Springer Briefs in Materials, DOI: 10.1007/978-3-642-36427-32.

[69] Eda G. and Shivkumar S. Bead-to-fiber transition in electrospun polystyrene. *Journal of Applied Polymer Science*, 106(1):475–487, 2007.

[70] Yuan X., Zhang Y., Dong C. and Sheng J. Morphology of ultrafine polysulfone fibers prepared by electrospinning. *Polymer International*, 53(11):1704–1710, 2004.

[71] Li G., Li P., Yu Y., Jia X., Zhang S., Yang X. and Ryu S. Novel carbon fiber/epoxy composite toughened by electrospun polysulfone nanofibers, *Materials Letters*, 62(3): 511-514, 2008.

[72] Zhang J., Lin T. and Wang X. Electrospun nanofibre toughened carbon/epoxy composites: Effect of polyetherketone cardo (PEK-C) nanofibre diameter and interlayer thickness, *Composites Science and Technology*, 70: 1660-1666, 2010.

[73] Zhang J., Yang T., Lin T. and Wang C-H. Phase morphology of nanofibre interlayers: Critical factor for toughening carbon/epoxy composites, *Composite Science and Technology*, 72: 256-262.

[74] Van der Heijden S., Daelemans L., De Schoenmaker B., De Baere I., Rahier H., Van Paepegem W., De Clerck K. Interlaminar toughening of resin transfer moulded glass fibre epoxy laminates by polycaprolactone electrospun nanofibres, *Composite Science and Technology*, 104: 66-73, 2014.

[75] Herwan J., Al-Bahkali E., Khalil K. A. and Souli M. Load bearing enhancement of pin joined composite laminates using electrospun polyacrylonitrile nanofiber mats, *Arabian Journal of Chemistry*, 9, 262, 2016.

[76] Bilge K., Venkataraman S., Menciloglu Y.Z. and Papila M. Global and local nanofibrous interlayer toughened composites for higher in-plane strength. *Composites Part A*, 58:73–76; 2014.

[77] Liu L., Zhang H. and Zhou Y. Quasi-static mechanical response and corresponding analytical model of laminates incorporating with nanoweb interlayers, *Composite Structures*, 111:436-445, 2014.

[78] Matulevicius, J., Kliucininkas L., Martuzevicius D., Krugly E., Tichonovas M. and Baltrusaitis, Design and Characterization of Electrospun Polyamide Nanofiber Media for Air Filtration Applications *Journal of Nanomaterials*, Article ID 859656, 2014.

[79] Sanatgar, R. H., Borhani S., Ravandi S. A. H. and Gharehaghaji A. A. The influence of solvent type and polymer concentration on the physical properties of solid state polymerized PA66 nanofiber yarn, *Journal of Applied Polymer Science*, 126, 1112, 2012.

[80] Saghafi H., Brugo T., Minak G. and Zucchelli A. The effect of PVDF nanofibers on mode-I fracture toughness of composite materials, *Composites Part B*, 72:213-216, 2015.

[81] Palazzetti R., Zucchelli A., Gualandi C., Focarete M. L., Donati L., Minak G. and Ramakrishna S. Influence of electrospun Nylon 6,6 nanofibrous mats on the interlaminar properties of Gr-epoxy composite laminates, *Composite Structures*, 94(2): 571-579.

[82] Daelemans L., Van der Heijden S., De Baere I., Rahier H., Van Paepegem W. and De Clerck K. Nanofibre bridging as a toughening mechanism in carbon/epoxy composite laminates interleaved with electrospun polyamide nanofibrous veils, *Composites Science and Technology*, 117, 244, 2015.

[83] Daelemans L., Van der Heijden S., De Baere I., Rahier H., Van Paepegem W. and De Clerck K. Using aligned nanofibres for identifying the toughening micromechanisms in nanofibre interleaved laminates, *Composites Science and Technology*, 124, 17-26, 2016.

[84] De Baere I., Van Paepegem W., Quaresimin M. and Degrieck J. On the tension–tension fatigue behaviour of a carbon reinforced thermoplastic part I: Limitations of the ASTM D3039/D3479 standard, *Polymer Testing*, 30, 625–632, 2011.

[85] De Baere I., Van Paepegem W., Hochard C. and Degrieck J. On the tension–tension fatigue behaviour of a carbon reinforced thermoplastic part II: Evaluation of a dumbbell-shaped specimen, *Polymer Testing*, 30, 663-672, 2011.

[86] Aktas M. and Karakuzu R. Determination of mechanical properties of glass-epoxy composites in high temperatures, *Polymer Composites* 30 (10), 1437-1441, 2009.

[87] ASTM D5528–13. Standard Test Method for Mode I Interlaminar Fracture Toughness of Unidirectional Fiber-Reinforced Polymer Matrix Composites.

[88] Simon S. and Strunk L. Fiber Volume of Resin Matrix Composites by Density Measurement. *International SAMPE Symposium Exhibition*. 32, 116-122, 1987.

[89] Palazzetti R. Flexural behavior of carbon and glass fiber composite laminates reinforced with Nylon 6,6 electrospun nanofibers. *Journal of Composite Materials*, 49(27), 3407-3413, 2015.

[90] Ramirez VA, Hogg PJ, Sampson WW. The influence of the nonwoven veil architectures on interlaminar fracture toughness of interleaved composites. *Composites Science and Technology* 2015; 110: 103–110.

[91] Nash NH, Young TM, Stanley WF. The reversibility of Mode-I and -II interlaminar fracture toughness after hydrothermal aging of Carbon/Benzoxazine composites with a thermoplastic toughening interlayer. *Composite Structures* 2016; 152: 558–567.

[92] Kuwata M, Hogg PJ. Interlaminar toughness of interleaved CFRP using non-woven veils: Part 1. Mode-I testing. *Composites Part A: Applied Science and Manufacturing* 2011; 42(10): 1551–1559.

- [93] Moroni F., Palazzetti R., Zucchelli A. and Pironi A. A numerical investigation on the interlaminar strength of nanomodified composite interfaces. *Composites Part B: Engineering*, 55: 635-641, 2013.
- [94] Beckermann G. W. and Pickering K.L. Mode I and Mode II interlaminar fracture toughness of composite laminates interleaved with electrospun nanofibre veils, *Composites Part A*, 72:11-21, 2015.
- [95] R. Palazzetti, *Electrospun nanofibrous interleaves in composite laminate materials*, PhD Thesis, Università di Bologna, 2013.
- [96] Xiang C. and Frey, M.W. Increasing Mechanical Properties of 2-D-Structured Electrospun Nylon 6 Non-Woven Fiber Mats. *Materials* 9, 270, 2016.
- [97] Molnar K., Kostakova E. and Meszaros L. The effect of needleless electrospun nanofibrous interleaves on mechanical properties of carbon fabrics/epoxy laminates *eXPRESS Polymer Letters*, 8(1), 62, 2014.
- [98] Alessi S., Filippo M. D., Dispenza C., Focarete M. L., Gualandi C., Palazzetti, R., Pitarresi G., Zucchelli, A. Effects of Nylon 6,6 nanofibrous mats on thermal properties and delamination behavior of high performance CFRP laminates, *Polymer Composites*, 36, 1303, 2015.
- [99] Virtual Crack Closure Technique (VCCT) in ANSYS https://caeai.com/sites/default/files/vcct_in_ansys_0.pdf, Access date: 10.02.2017.
- [100] Jiang H. Cohesive zone model for carbon nanotube adhesive simulation and fracture/fatigue crack growth, The Graduate Faculty of The University of Akron, 2010.
- [101] Gözlüklü B. Delamination analysis by using cohesive interface elements in laminated composites, Middle East Technical University, MSc Thesis, 2009.
- [102] Barbero E.J., *Finite Element Analysis of Composite Materials Using ANSYS*, Second Edition CRC Press, 2014.

VITA

Bertan BEYLERGİL
03/05/1982, Ankara

EDUCATION

Ph.D. (2013-2017): Mechanical engineering, Izmir Institute of Technology
M. Sc. (2008-2010): Mechanical engineering, Nigde University
B. Sc. (2001-2006): Mechanical engineering, Dokuz Eylul University

THESES

2007-2010: M. Sc. Thesis
Thesis title: Yapıştırılarak bağlantı sağlanan kompozit plakaların bağlantı performansının artırılması
Advisor: Assoc. Prof. Yusuf Cunedioğlu, Co-advisor: Prof. Alaattin Aktaş
2013-2017: Ph. D. Thesis
Thesis title: Toughening of carbon fiber based composites with electrospun fabric layers
Advisor: Prof. Metin Tanoğlu, Co-advisor: Assoc. Prof. Engin Aktaş

PEER-REVIEWED PUBLICATIONS (SCI and SCI Expanded)

Beylergil, B., Tanoglu, M. and Aktaş, E. “Enhancement of interlaminar fracture toughness of carbon fiber/epoxy composites using polyamide 6/6 electrospun nanofibers”, *Journal of Applied Polymer Science*, Volume 134, Issue 35, September 15, 2017, 45244.

Beylergil, B., Tanoglu, M. and Aktaş, E. “Modification of carbon fiber epoxy composites by polyvinyl alcohol (PVA) based electrospun nanofibers”, *Advanced Composites Letters*, 2016, 26(3), 69-76.

Cunedioğlu, Y. and **Beylergil, B.** “Free vibration analysis of damaged composite beams”, *Structural Engineering and Mechanics*, 2015, 55(1), 79-92.

Beylergil, B., Aktaş, A. and Pekbey, Y. “Shear strength of pultruded composite pins with external confinement”, *Advanced Composite Materials*, 2014, 23(4), 375-387.

Cunedioğlu, Y. and **Beylergil, B.** “Free vibration analysis of laminated composite beam under room and high temperatures”, *Structural Engineering and Mechanics*, 2014, 51(1), 111- 130.

Kaya, M. T., Aktaş A., **Beylergil B.** and Akyıldız H. K. (2014). “An experimental study on friction drilling of St12 steel”, *Transactions of the Canadian Society for Mechanical Engineering*, 2014, 38(3), 319-329.

Güngör, A., Bayrak, M. and **Beylergil, B.** (2013). “In view of sustainable future energetic exergetic and economic analysis of a natural gas cogeneration plant”, *International Journal of Exergy*, 2013, 12(1), 109.

Beylergil, B., Aktaş, A. and Cunedioğlu Y. “Buckling and compressive failure of stepped lap joints repaired with composite patches”, *Journal of Composite Materials*, 2012, 46(26), 3213-3230.

Beylergil, B., Cunedioğlu, Y. and Aktaş, A. “Enhancement of single lap composite joints Strength at different temperatures”, *Journal of Adhesion Science and Technology*, 2012, 26, 1453-1465.

Beylergil, B., Aktaş, A. and Pekbey, Y. “Enhancement of flexural performance of wood beams using textile fabrics”, *Science and Engineering of Composite Materials*, 2012, 1-8.

Beylergil, B., Cunedioğlu, Y. and Aktaş, A. “Experimental and numerical analysis of single lap composite joints with inter adherend fibers”, *Composites Part B: Engineering*, 2011, 42(7), 1885-1896.